Colloidal Crystals: Structure, Dynamics, and the Importance of Dimer Bonds

by Sharon Jane Gerbode

This thesis/dissertation document has been electronically approved by the following individuals:

Cohen,Itai (Chairperson)

Sethna,James Patarasp (Minor Member)

Franck,Carl Peter (Minor Member)

COLLOIDAL CRYSTALS: STRUCTURE, DYNAMICS, AND THE IMPORTANCE OF DIMER BONDS

A Dissertation

Presented to the Faculty of the Graduate School

of Cornell University

in Partial Fulfillment of the Requirements for the Degree of

Doctor of Philosophy

by

Sharon Jane Gerbode

August 2010

© 2010 Sharon Jane Gerbode

ALL RIGHTS RESERVED

COLLOIDAL CRYSTALS:

STRUCTURE, DYNAMICS, AND THE IMPORTANCE OF DIMER BONDS

Sharon Jane Gerbode, Ph.D.

Cornell University 2010

Colloidal crystals, periodic arrays of micron-sized solid particles in solution, offer a unique glimpse of the particle-scale structures and dynamics within a true thermodynamic ensemble. Experimental colloidal studies of melting and crystallization [55, 56, 13, 76, 2] as well as non-equilibrium states such as colloidal glasses [67, 68, 29, 49] have uncovered numerous mechanisms that are experimentally inaccessible in atomic systems due to both small timescales and small lengthscales. The great successes of colloidal physics have emerged as a result of technological advances enabling synthesis of large batches of monodisperse spherical particles. Yet, the crystal structures formed by such particles are limited to variations on layers of close-packed spheres. Consequently, one of the current frontiers in colloidal physics is the study of novel crystal structures formed by non-spherical particles.

My thesis work has focused on crystals formed by colloidal dimer particles consisting of two connected spherical lobes. Surprisingly, while the structure of two dimensional crystals formed by the dimers are quite similar to those observed for spheres, the motion of defects within the dimer crystals is significantly different. Geometric obstacles formed by interlocking dimers restrict the motion of defects and ultimately introduce a completely unexpected, previously unreported glassy defect dynamics within a colloidal crystal.

BIOGRAPHICAL SKETCH

Sharon Gerbode is the daughter of Gail Gerbode and Frank "Sarge" Gerbode. She has four siblings: Colin, Ian, Vanessa and Holly. In addition to her academic pursuits, Sharon is interested in education outreach, especially in relation to the "forgotten" students in juvenile detention centers or prisons. She also enjoys playing music, dancing, and driving on long roadtrips.

This thesis is dedicated to those students in prison who find inspiration and hope in the study of the natural world, and whose intellectual reach extends far beyond the boundaries of their daily lives.

ACKNOWLEDGEMENTS

The work described in this thesis would not have been possible without the support of my advisor Itai Cohen and his creative, collaborative group of students and post-doctorate associates, especially Mark Buckley, Leif Ristroph, Rajesh Ganapathy, John Savage, and Xiang Cheng. Outside of the Cohen group, John Gregoire, Ryan Shannon, and Matt Warkentin have provided a soundboard for my research ideas and problems ever since we started at Cornell together in the fall of 2004. My collaborators have also provided invaluable advice and suggestions, especially Stephanie Lee and Fernando Escobedo. I also wish to sincerely thank my committee members Carl Franck and Jim Sethna for their support and advice throughout my years at Cornell.

Beyond my academic life, many others have contributed crucial support and love without which I could never have reached this point. Rather than naming the many friends and relatives who have helped me grow and learn, I would like to thank my loving parents Gail and Sarge. Since day one, they have encouraged me to enjoy life and be curious and bold in everything I do. It wasn't until I was entering adulthood that I realized how unusual it was for a young child to jump into a discussion among adults to add her perspective. Itai once described this as 'gumption' - whether it is a blessing or a curse, I am certain that this gumption has helped me tremendously as a scientist.

TABLE OF CONTENTS

Biographical Sketch . . . iii
Dedication . . . iv
Acknowledgements . . . v
Table of Contents . . . vi
List of Figures . . . viii

1 Introduction **1**
1.1 Colloidal crystals . . . 1
1.2 Colloidal glasses . . . 4
1.3 Nonspherical colloidal particles: a new frontier . . . 5
1.4 Guide to the thesis . . . 7

2 2-D Crystals of Colloidal Dimer Particles **8**
2.1 Introduction . . . 8
2.2 Experimental System . . . 8
2.3 Structure of the dimer crystals . . . 11
2.4 Defects in the dimer crystals . . . 13
2.5 Conclusions . . . 16
2.6 Supplementary materials . . . 16
2.6.1 Monte Carlo simulations . . . 16

3 Vacancies in Degenerate Crystals of Colloidal Dimers **19**
3.1 Abstract . . . 19
3.2 Introduction and experimental setup . . . 19
3.3 Experimental results . . . 21
3.4 Vacancy motion . . . 26
3.4.1 Monte Carlo simulations . . . 27
3.5 Conclusions . . . 39

4 Restricted Dislocation Motion in Crystals of Colloidal Dimers **41**
4.1 Abstract . . . 41
4.2 Introduction . . . 41
4.3 Confining the particles to a quasi 2-D layer . . . 43
4.4 Dislocation nucleation and glide . . . 43
4.5 Unrestricted glide "zippers" . . . 46
4.6 Dislocation reactions . . . 48
4.7 Estimate of energetic cost for arbitrary dislocation separation . . . 49
4.8 Conclusions . . . 50
4.9 Supplementary materials . . . 51
4.9.1 Dislocation separation energy calculation . . . 51

5 Glassy Dislocation Dynamics in Crystals of Colloidal Dimers **55**
5.1 Abstract . . . 55
5.2 Introduction . . . 55
5.3 Local mechanical perturbation using optical tweezers . . . 57
5.4 Effect of grain size on response to perturbations . . . 59
5.5 Multi-defect mechanisms: long time relaxation experiments . . . 60
5.6 Glassy two-stage dislocation relaxation . . . 62
5.7 Cage-hopping dislocation motion . . . 63
5.8 Conclusions . . . 66
5.9 Supplementary materials . . . 66
5.9.1 Experimental techniques . . . 66
5.9.2 Molecular dynamics simulations . . . 67

6 Transition into the Glassy Dislocation State **72**
6.1 Abstract . . . 72
6.2 Introduction . . . 72
6.3 Experimental system . . . 73
6.4 Numerically generated mixed crystals . . . 75
6.5 Conclusions . . . 78

7 Dimer dreams for the future and a dose of reality **79**
7.1 Abstract . . . 79
7.2 Dimer dreams . . . 79
7.3 Reality . . . 81

8 Epitaxial Crystal Growth: Spherical Particles **86**
8.1 Introduction . . . 86
8.2 Experimental system . . . 86
8.3 Experimental results . . . 88
8.4 Simulating particle diffusion on an island . . . 92
8.5 Conclusions . . . 97

A Colloidal Dimer Synthesis **98**

B Ramp Cell Construction **99**

C The Depletion Effect **101**

D Substrate Fabrication **103**
D.1 Patterning holes into a PMMA layer . . . 103
D.2 Patterning holes directly into glass . . . 105

Bibliography **108**

LIST OF FIGURES

1.1 (a) In a defect-free plane of crystalline spheres, each sphere has 6 nearest neighbors. (b) In an edge dislocation, one 5-fold coordinated sphere (pink) is paired with one 7-fold coordinated sphere (blue). The 5-7 pair is located at the end of an extra row of spheres when viewed along either of two crystalline axes (green dotted lines). The third axis (orange dottted line) defines the direction for dislocation glide. 3

1.2 Schematic of the two-stage KTHNY theory for 2-D melting. (a) Bound pairs of dislocations can occur in the crystal phase. (b) In the hexatic phase, dislocation pairs separate, but the 5-7 disclination pairs remain bound together. (c) In the fluid phase, the disclinations unbind and all crystalline order is lost. In this frame, the defects are not colored. 4

2.1 Fluorescent silica particles. (a) FE-SEM image of monodispersed hematite colloids from which hollow particles are templated. Scale bar, 2.5 microns. (b) TEM bright-field micrograph of intact silica shells (thickness, 65 nm). Scale bar, 1.5 μm. (c) XRD pattern of hematite particles (bottom, black), hematite-silica core-shell particles (middle, light gray), and hollow silica shells (top, dark gray). The bottom two show peaks corresponding to crystalline hematite (JCPDS card no. 33-0664), while the top exhibits only an amorphous signature indicative of complete etching. (d) Collapsed particle (thickness, 28 nm), illustrating a typical morphology below the critical thickness, t_c. Scale bar, 400 nm. 9

2.2 Confocal microscope images of dense monolayers of dimer particles. (a) Schematic of wedge-shaped confinement cell used to constrain the nonspherical dimer colloids. Details of the confinement cell construction are provided in Appendix B. The hatched area indicates a region where the gap height is roughly 1.5 μm. (b) Confocal image of a dense monolayer of colloids taken across the equatorial plane (inset, schematic view). Scale bar, 5 μm. (c) Triangular ordering of the lobes is revealed when an image is captured at a focal plane that just grazes the particle lobes (inset, schematic). Scale bar, 5 μm. 10

2.3 Structural characterization. (a) Lobe radial distribution function, $g(r)$. b) Histogram of particle orientations taken from various crystallites. The first peak measured from each grain is shifted to $\theta = 30°$. (c) The orientation correlation function, $G_6(r)$ for an ideal structure (gray hatched line) and our experimental system (black line). The latter shows a non-zero but decreasing long-range value, indicating that while interparticle angles are ordered close to multiples of $\pi/3$, crystal defects may be present. 11
2.4 Kagomé construction of the Degenerate Crystal. (a) Schematic of the structure of the DCs observed in prior simulations [71]. Red dots represent the particle centers, white circles show the kagomé lattice sites, and dashed grey lines indicate the three crystalline axes (after [71]). (b) Kagomé construction applied to the experimental data with dimer colloids. The overlaid kagomé net is a guide for the eye. 13
2.5 Defects and Monte Carlo simulations. (a) Voronoi reconstruction for experimental data, showing $N = 2394$ particle lobes color-coded by their coordination number. Defect lobes with a coordination number other than six are highlighted with non-white colors. (b) Voronoi reconstruction from MC simulations at a compression rate of 0.17. A magnified region of the total sample area ($N = 7200$ lobes) is shown for clarity. (c) Lobe pair correlation function associated with the simulation set from b. Inset, magnified view of the first few peaks. (d) Comparison of the defect fraction in crystals made of dimer particles (black squares) versus spherical particles (gray asterisks) at various compression rates. Trend lines are added to guide the eye. 15

3.1 Confocal images of a Degenerate Crystal grain of dimer particles. A focal slice through the dimer centers looks disordered (a), but a slice through the tips resembles close-packed spheres (b). 20
3.2 Scanning Electron Microscope image of the fluorescent silica dimer shells. A stretched dimer is overlaid in white as a guide to the eye. 21
3.3 The pair correlation function $g(r)$ for experimental data (a) and for simulated data (b). 22
3.4 Microscope images overlaid with coordination number plots. The frames were imaged at time (a) $t = 0$ hours, (b) $t = 3$ hours, and (c) $t = 21$ hours. Between frames (a) and (b), the area fraction was slowly increased to near lobe close-packing. Coordination number key: light blue = 6, pink = 7, dark blue = 5, yellow = 8. 22

3.5 Schematic of dislocation glide in a triangular crystal of spherse. (a) An edge dislocation in a 2-D triangular crystal looks like one partial row and is made up of one 5-fold coordinated defect (pink) and one 7-fold coordinated defect (blue). (b) Slight shifting of the 7-defect particle moves the entire dislocation down by one row. 24
3.6 (a) Dimers aligned parallel to glide direction allow dislocation glide. (b) Interlocking particles block glide. 25
3.7 The particles in both experimental (a) and the simulated (b) DCs are randomly oriented. 26
3.8 The allowed vacancy move corresponds to a dimer swinging one of its lobes into a neighboring vacancy. This is the only vacancy move that is observed in the experiments. 28
3.9 The energy cost of a dimer move can be estimated by considering the overlap area that would be required to make the move. (a) No overlap in the initial configuration. The overlap required for dimer swinging (b) is half that for sliding (c). 28
3.10 (a) A divacancy is created by removing one entiredimer from an initially aligned DC. (b) Lattice sites that have been visited by a vacancy in 1000 dimer moves are represented in greyscale. 30
3.11 (a) One top-lobe vacancy and one bottom-lobe vacancy are shown in their initial positions. (b) The top-lobe vacancy moves to the left, while the bottom-lobe vacancy moves to the right. Sites visited by a vacancy in 100 dimer moves are represented in grayscale. 31
3.12 (a) Two top-lobe vacancies in a single row. (b) The accessible region for the left vacancy if the right vacancy is fixed is shown in gray. 31
3.13 One top-lobe vacancy and one bottom-lobe vacancy in a single row before (a) and after (b) 1000 dimer moves. 32
3.14 Ladder effect with two vacancies: a top-lobe vacancy on the left and a bottom-lobe vacancy on the right. (a) Initial configuration near the bottom-lobe vacancy. A second vacancy in the top-lobe position is out of the field of view to the left. (b) After the bottom-lobe vacancy moves, the nearby dimer (mauve) is reoriented. (c) Now the left top-lobe vacancy can move down from the ladder dimer (bright pink) to the reoriented dimer, entering the lower row. 33
3.15 The 'bi-switch' (a), 'tri-switch' (b), and 'quad-switch' (c) reorient particles without changing their collective footprint on the lattice. 34
3.16 (a) An initially aligned dimer lattice. (b) The same lattice after 10^5 Wojciechowski switches. 35

3.17 Most single vacancies in randomly oriented dimer lattices can visit all lattice sites. Here the sites visited within 10^3 dimer moves are shown in grayscale. The gray cluster percolates the system. 35
3.18 The MSD for vacancies in aligned dimer crystals (blue curve) and randomly oriented dimer DC crystals (red curve). The black curve represents an MSD of slope 1 on the log-log plot, representing what would be expected for a diffusive system. For waiting times up to 500 time steps, the motion of vacancies in DCs is subdiffusive. 36
3.19 (a) Initially the central vacancy is stuck and the top left one is mobile. (b) After 60 moves, it is still stuck. (c) After 1400 moves, it is still stuck, even though the mobile vacancy has visited some neighboring sites. (d) After 1800 moves, it is finally released. . . 37
3.20 A theoretical cage containing 11 lattice sites. None of the surrounding particles are oriented in such a way that they can swing in to release the vacancy. 38

4.1 Before-and-after micrographs illustrating observed dislocation nucleation and glide moves. Particle lobes have been marked with dots, nearest neighbor bonds are indicated by lines, and dislocations consisting of paired fivefold and sevenfold coordinated lobes have been highlighted. (a,b) One rotating dimer particle (highlighted with a thick black dumbbell) nucleates a pair of dislocations. (c,d) A dislocation glides down by three rows through a combination of one sliding move (upper dumbbell) followed by one swinging move (lower dumbbell). 44
4.2 A schematic of dislocation nucleation and glide in monolayers of spheres (a - c) and dimer particles (d - f). (a,b) Displacing two spheres (gray) creates a pair of dislocations, each containing one 5-fold and one 7-fold coordinated particle. (b,c) The pair glides apart when the sevenfold particles shift parallel to their Burgers vectors (outlined arrows). (d) In DCs, a dislocation pair is created by rotating one particle (gray). Glide proceeds through the motion of the lobes marked with arrows, either by swinging (blue particle) or sliding (green particle). (e) The separation of a dislocation pair shears the crystal, which leaves swinging and sliding particles intact. The red particles, however, would have to be severed by this deformation, indicating that dislocation motion is blocked by such particle orientations. (f) The sequence of green and blue particles is a zipper of length $Z = 4$. . 45

4.3 The distribution of zipper lengths in both experimental (empty squares) and simulated (solid triangles) DCs. Counting statistics determine the error bars, which for the simulations are smaller than the symbols. The average zipper length measured from experimental DC grains is $\bar{Z}_{exp} = 4.6 \pm 0.2$. Zippers in simulated crystals with 10^4 lattice sites are only slightly longer: $\bar{Z}_{sim} = 6.18 \pm 0.01$. The dotted line is the best fit exponential for $Z > 6$, having the form $\rho(Z) = 0.37e^{-Z/4.4}$. The inset shows the ensemble of glide-permitting particle orientations given nucleation via clockwise rotation of the gray particle. Particle configurations including a subset of these orientations enable glide via swinging (blue/dark gray) or sliding (green/light gray). . . . 47

4.4 An observed dislocation reaction allowing a dislocation to hop from one zipper to another. Only the relevant defects have been highlighted, and their Burgers vectors are indicated by outlined arrows. (a) A dislocation gliding down from the upper right is one lobe from the end of its zipper. (b) The dislocation has reacted and proceeds by gliding down another zipper extending horizontally to the left. A second dislocation, visible to the lower right of the reaction site, was emitted to conserve total Burgers vector. 49

4.5 Pathways for dislocation pair separation in crystals of spheres (a) and DCs (b,c). Pair nucleation occurs at the location marked with a star in each pathway. (a) Dislocation pair separation is achieved through nucleation and glide along a straight line parallel to the direction of the defects' burgers vectors $\pm\vec{b}$. This process results in a pair separation of Na. (b) In an otherwise defect-free DC, an identical dislocation pair $\pm\vec{b}$ separates by Z_0a, the average zipper length, before undergoing dislocation reactions and traveling along a sequence of tilted path segments of length Z_0a. This pathway also results in a separation of Na along the burgers vector direction. (c) The shortest pathway with segment length Z_0a yields a separation of Na along a direction rotated by $\pi/6$ from the axis of the burgers vectors $\pm\vec{b'}$. 52

5.1 Micrographs illustrating a local perturbation experiment. Five-fold and seven-fold coordinated defects created by the perturbation are marked with pink and blue dots, respectively. (a) A single spherical intruder particle in a small grain is dragged by 1 LC using optical tweezers. (b) Two dislocations marked by arrows glide to the grain edge and are absorbed by the grain boundary (solid closed curve). (c) The intruder particle remains stationary after the tweezers are turned off. The vacancy left behind has no topological charge and is stable. (d-f) In a large grain (only the central part is shown here) the dislocations marked by arrows are obstructed by the particles in red. When the tweezers are turned off, the blocked dislocations return along their glide paths, recombining and causing the intruder particle to recoil. . . 58
5.2 Recoil distance R as a function of glide distance Z to the nearest grain boundary. The error bars represent uncertainty in particle position. The distribution of unrestricted glide distances $\rho(Z)$ (dashed gray curve) is reprinted from [22]. 60
5.3 Average number of defects versus time for large (> 700 particles) degenerate crystals and crystals of spheres. Error bars represent the standard error of the mean. The solid line is the best fit exponential for the decay in the sphere data ($R^2 = 0.99$); the dashed line is the best fit sum of an exponential and a logarithmic decay for the dimer data ($R^2 = 0.99$). 61
5.4 Defect trajectories in simulated crystals under shear (large arrows). (a) Dislocations in a crystal of spheres glide along straight paths in response to the applied shear. (b) Dislocations in a degenerate crystal follow crooked trajectories as they hop between caged configurations. (c) MSD of individual dislocations in crystals of spheres and degenerate crystals. Error bars are smaller than the markers. The solid curve is the best fit for $MSD = \langle \Delta r^2 \rangle = u^2 t^2 + 2Dt$. 65
5.5 The grain boundary defects are highlighted around the small grain also shown in Fig. 5.1c above. Pink and blue dots represent lobes having a number of nearest neighbors equal to 5 or 7, respectively. The dotted circle marks the spherical intruder particle. 67
5.6 Dislocation mean squared displacement in crystals of spheres under uniform shear at three different shear rates $\dot{\gamma}$. Error bars represent the standard error of the mean. 69

6.1 (a) Optical microscope image of a mixed sphere and dimer crystal with $\phi_d = 0.4$. Dumbells are overlaid on top of the dimers for clarity. The bright white sphere is a PS intruder particle. (b) Distribution of dimer orientations within the grain. Error bars are derived from counting statistics. 74
6.2 Example of a numerically calculated mixed crystal with dimer concentration $\phi_d = 0.3$. (a) The lattice sites that are dimer bonded are colored in matching darker hues, while the sphere lattice sites are uniquely colored lighter hues. Inset: Zoomed in view illustrating the color-coding for dimers versus spheres. (b) The distribution of dimer orientations for this mixed crystal demonstrates that the three lattice directions are equally weighted. Error bars are derived from counting statistics. 76
6.3 The distribution of cage sizes for each dimer concentration. Marker key: black squares: $\phi_d = 1.0$, purple squares: 0.9, blue squares: 0.8, green squares: 0.7, yellow squares: 0.6, red squares: 0.5, purple circles: 0.4, blue circles: 0.3, green circles: 0.2, yellow circles: 0.1. The curves are fits as described in the text. The distribution is also shown in a semilog plot as the inset. 77
6.4 The peak cage size z_* as a function of dimer concentration ϕ_d. The line is the best fit power law, as described in the text. 78

7.1 Examples of typical nearly dimer-sized mutant particles commonly found in the monolayer region of the wedge-shaped ramp cells used for experiments. 82
7.2 The process of semi-automatic lobe identification. (a) A typical confocal image, demonstrating the variety of particle appearances. (b) The same image a brightness/contrast adjustment and an edge-finding algorithm defined in ImageJ. (c) The same image after inversion and a bandpass filter applied using ImageJ. (d) The same image after an additional bandpass filter applied using Matlab. (e) The same image shown in (d) with the located lobe positions overlaid as red plus symbols. (e) The lobe positions overlaid on the original image. Note that the vacancy does not get counted as a lobe. Also note the two misidentified dimers marked with circles. 83

8.1 Schematic of islands formed on the crystalline substrate. The permanently bonded monolayer is shown in gray, while the particles making up the epitaxially grown islands are colored blue. (a) On top of this 15 particle island, there are 3 additional particles shown in 3 different types of island sites (details in text): $p = 0$ (green), $p = 1$ (yellow), and $p = 2$ (orange). (b) The single particle in red on top of this 3 particle island is in a site with $p = 3$, since all 3 exit pathways descend off of the island. 88
8.2 Schematic of the energy landscape near a the edge of an island for atoms (a) and for our colloidal system (b). The edge of the island is marked with a red dotted line in each schematic. 89
8.3 Mean residence times spent in each site atop the 15 particle island shown in gray. Colorbars indicate mean residence time. The values of residence time represent averages over 100 independent experiments. The mean residence time is largest for the corner sites ($p = 2$), lower for the edge sites ($p = 1$), and lowest for the interior sites ($p = 0$). 91
8.4 (a) Schematic of the 1-D random walk model for a single pathway. (b) Schematic of the model for 3 pathways. 93
8.5 The distribution of residence times in the weak-interaction limit is shown for each of 4 kinds of lattice sites. 95
8.6 The distribution of residence times in the strong-interaction limit is shown for each of 4 kinds of lattice sites. 96
8.7 The mean residence time τ as a function of p, scaled by the mean residence time when $p = 0$. Experiments are shown as black squares. Error bars are on the order of the symbol size and show SEM. Simulations in the strong interaction limit (red circles) and weak interaction limit (green circles) are also shown. 96

B.1 Schematic of wedge-shaped confinement cell construction. The wedge angle is exaggerated for clarity. (a) One base-washed coverslip (blue) is bonded with UV glue to a larger microscope slide (beige) to provide structural support for the cell. (b) Small UV glue droplets (yellow) are placed in two rows on the coverslip and are cured to become spacers for the cell. (c) A second base-washed coverslip is placed on top of the first, and the two are squeezed together until the two coverslips bond together (bonded region shown in white). (d) UV glue (shown in yellow) is then used to seal three sides of the cell, leaving an access gap for inserting colloidal samples. Once the cell is filled with sample, this gap is also sealed using UV glue. 100

C.1 Illustration of the depletion effect. The purple and blue spheres represent large and small colloidal particles, respectively. The shaded green regions surrounding the purple particles represents the excluded volume that the small spheres cannot access. (a) When two large particles are sufficiently separated, these excluded regions do not overlap. (b) If the purple particles move close enough that the blue particles cannot fit in the region between then, the total excluded volume for the spheres is decreased and an effect attractive interaction is produced. 101

D.1 Illustration of the process for patterning holes into a PMMA layer on top of a borosilicate coverslip. Process details corresponding to each lettered frame are provided in the text. Color code is as follows: gray-coverslip; blue-PMMA. 104

D.2 Illustration of the process for patterning holes into a glass layer on top of a borosilicate coverslip. Process details corresponding to each lettered frame are provided in the text. Color code is as follows: gray-coverslip; orange-silica; black-Chromium; blue-PMMA. 105

CHAPTER 1

INTRODUCTION

Colloidal suspensions are thermal systems consisting of solid, traditionally spherical particles suspended in a liquid solvent. The micron-sized particles are small enough to undergo Brownian motion in the fluid solvent, but are large enough (and slow enough, with a diffusion constant of about $1\ \mu\text{m}^2/\text{s}$) that they may be easily visualized with an optical microscope. As such, colloids offer a truly unique opportunity to actually watch the time evolution of a thermodynamic system, particle by particle. This unprecedented window into the configurations and dynamics of thermal particles has revealed an intimate view of both equilibrium and nonequilibrium phases formed by large collections of colloidal particles under confinement at controlled concentrations. Results obtained from experiments on colloidal systems have been used to probe unanswered questions in analogous atomic or molecular systems whose constituents are made inaccessible by both size and speed. In addition to their usefulness as tools for addressing fundamental statistical mechanics problems, colloidal crystals are also industrially interesting as candidates for self-assembly of photonic band gap materials [66] and as model systems for studying nanoparticle crystals such as those proposed for solar cell or LED materials [42].

1.1 Colloidal crystals

While it is possible to induce attractions between colloidal particles using clever tricks like the depletion effect[1], the simplest kind of colloidal crystal is formed

[1] A detailed description of the depletion effect is provided in Appendix C.

by particles with only hard core repulsive interactions. The phase diagram for confined hard spheres has been extensively studied both in three dimensions (3-D) [51, 7, 74] and in two dimensions (2-D) [58] and is an entropically-driven phase transition wherein the configurational phase space for the spheres is maximized when the particles form a lattice.

Whereas temperature is typically thought of as the relevant variable for controlling melting or freezing of an atomic or molecular crystal, in colloidal systems of hard spheres, this role is played by particle concentration, or volume fraction. The volume fraction ϕ (or area fraction in 2-D systems) is defined as the total volume (area) occupied by the particles divided by the system volume (area). In 3-D suspensions of confined hard spheres, the fluid to crystal transition is a first order phase transition and occurs at $\phi_* \approx 0.49$ while close-packing occurs at $\phi_{cp} = 0.74$ [51].

Experimental investigations of 3-D colloidal crystals of hard spheres have studied the role of crystal defects such as dislocations in processes such as melting [2] and nanoindentation [57]. 3-D crystal of spheres are made up of stacked 2-D planes of close-packed spheres, where each sphere has 6 nearest neighbors (Fig. 1.1a). An edge dislocation, one of the most common kinds of defects found in such crystals, can be identified as a pair of spheres, one with 5 nearest neighbors, and one with 7 (Fig. 1.1b). This 5-7 pair occurs at the end of an 'extra' row of spheres, when viewed along either of two crystal axes (marked with dotted green lines in Fig. 1.1b). The third crystal axis (marked with a dotted orange line in Fig. 1.1b) defines the direction for dislocation glide, the fundamental mechanism for dislocation motion. Each of the two individual defects (the 5-fold coordinated sphere and the 7-fold coordinated sphere) is called a disclination.

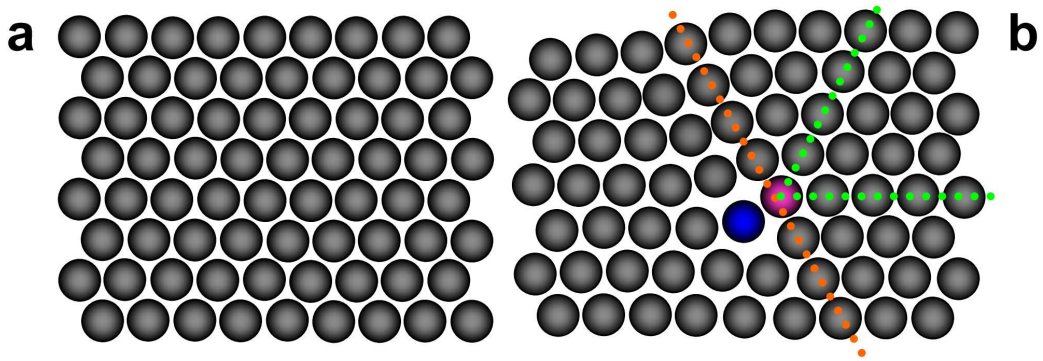

Figure 1.1: (a) In a defect-free plane of crystalline spheres, each sphere has 6 nearest neighbors. (b) In an edge dislocation, one 5-fold coordinated sphere (pink) is paired with one 7-fold coordinated sphere (blue). The 5-7 pair is located at the end of an extra row of spheres when viewed along either of two crystalline axes (green dotted lines). The third axis (orange dottted line) defines the direction for dislocation glide.

The melting of 2-D crystals of spheres has been theoretically addressed by Kosterlitz, Thouless, Halperin, Nelson, and Young [32, 43, 75]. In their 'KTHNY' theory, the melting of a 2-D crystal of spheres takes place in two stages, as depicted schematically in Fig. 1.2. In the first stage, dislocation pairs unbind (Fig. 1.2b), thereby destroying the translational order, but retaining an algebraically decaying long-ranged orientational order [43]. This orientationally ordered, translationally disordered state is called 'hexatic'. The transition from the hexatic state to the fluid state, which possesses neither translational nor orientational order (Fig. 1.2c), occurs when the individual disclinations making up the dislocations separate.

Studies of 2-D crystals of repulsive colloidal particles where individual dislocation and disclination formation and motion have been imaged on the particle scale have experimentally verified this KTHNY theory of two-stage melting for crystals of spheres [17]. This is just one example of how colloidal crystal exper-

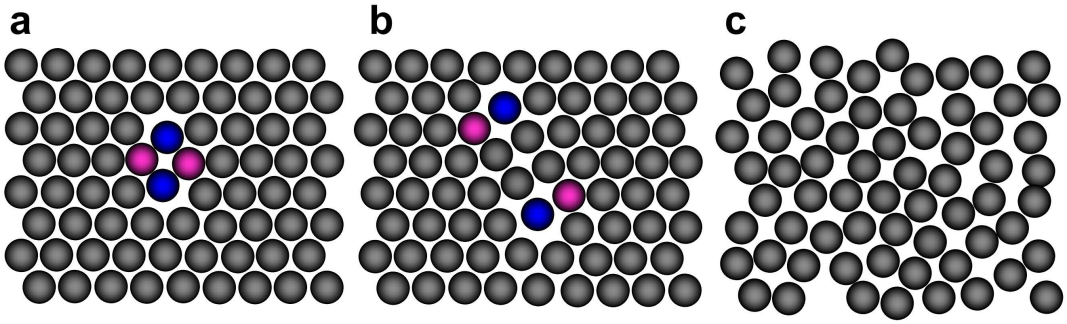

Figure 1.2: Schematic of the two-stage KTHNY theory for 2-D melting. (a) Bound pairs of dislocations can occur in the crystal phase. (b) In the hexatic phase, dislocation pairs separate, but the 5-7 disclination pairs remain bound together. (c) In the fluid phase, the disclinations unbind and all crystalline order is lost. In this frame, the defects are not colored.

iments can serve as model statistical mechanical systems for studying fundamental condensed matter questions.

1.2 Colloidal glasses

The focus of this thesis is on crystals of colloidal particles; however, it is useful to briefly review some of the results from experimental colloidal studies of the glass transition. Colloidal glasses are disordered 3-D suspensions of spheres formed by quenching into a high-ϕ state, eg. by centrifuging a low-ϕ sample initially in a fluid state. If the quench rate is fast enough, the system becomes trapped out of equilibrium in a local minimum of the energetic landscape. Relaxation of the system in this glassy state cannot be described by a single relaxation timescale, but rather follows either a stretched exponential or logarithmic decay form – both functional forms can account for the multiple timescales which arise due to the broad distribution of local well depths in the complex

energy landscape [31, 28].

In colloidal glasses, the breadth of timescales can be intuitively grasped by considering the motion of the Brownian particles within the glass, which can be directly visualized in 3-D in colloidal systems [67]. Colloidal experiments have demonstrated a caging effect where individual particles are confined in cages formed by their neighbors [68]. Particle transport through the glass is characterized by two stages of motion: an initial fast diffusion until the particle encounters its caging neighbors, followed by a much slower cage-hopping process. This second mechanism relies on collective, multi-particle rearrangements that shift the cage structure, allowing the particle to jump between caged configurations. Such studies have provided insight on the hypothesis first proposed by Adam and Gibbs that the size of the smallest 'cooperatively rearranging region' diverges as the glass transition is approached [1]. The size of the cooperative regions have been directly measured in colloidal glasses [67], where the size of the smallest region was indeed found to increase. Furthermore, colloidal studies of confined glasses are making contributions to the longstanding question of whether such confinement makes the system more or less 'glassy' – that is, more or less restricted [44].

1.3 Nonspherical colloidal particles: a new frontier

Clearly much groundwork has been laid out for understanding condensed matter phenomena in systems of spherical particles. However, the range of crystalline structures that are formed by spheres is rather limited. Particles possessing anisotropy in either particle shape or interaction potential are required

in order to explore statistical mechanical questions in more complex lattices. Furthermore, the study of nonspherical particles is motivated by industrial applications of colloidal assemblies, which have been cited as a means to create periodic materials for photonic, optoelectronic, solar cell, and sensing applications. The technique is attractive because it holds promise for the simple microfabrication of low-cost, large-scale devices. However, spherical particles fail to capture the selective functionalities and geometries required to encode the ordering of assemblies that are more elaborate than variations on close-packing. In contrast are the many naturally occurring sophisticated structures such as icosahedral virus capsids and herringbone pentacene thin films, which use protein sub-units or small molecules as their structural motifs. These natural architectures inspire a strategy to increase complexity in traditional colloids by introducing symmetry-breaking features in the particle shape or interparticle potential. Essential to this idea is the ability to impart specific assembly instructions to the colloidal building blocks so that materials with enhanced functional properties can be made.

Recent advances in particle synthesis techniques have enabled the production of many new, exotic anisotropic particles [30, 39, 25, 23, 8]. While a rod or ellipsoid could arguably be called the simplest anisotropic particle shape, colloidal dimers consisting of two connected spherical lobes can theoretically fit into the same close-packed crystals that are formed by free spheres, with each lobe occupying a spherical crystal lattice positions. This similarity implies that the study of colloidal dimers may illuminate how a small perturbation to the known spherical building block can alter the properties of the resulting crystal.

1.4 Guide to the thesis

This thesis describes my experimental studies of colloidal crystals, with a strong emphasis on my investigations of crystals of colloidal dimer particles. Chapter 2 describes the structure of the crystalline phase formed by the dimer particles when they are confined in a 2-D chamber and notes the abundance of long-lived defects in the crystals. Chapter 3 addresses the question (posed by Jim Sethna for my A Exam) of how vacancies move in the dimer crystals. The culmination of my efforts on the dimer system are described in chapters 4 through 6, which describe in detail the restrictions on dislocation motion in crystals of dimers, and the resulting glassy dislocation dynamics that are observed in such crystals under external perturbation. Chapter 8 describes my contributions to a study using spherical colloidal particles to model epitaxial thin film crystal growth. Finally, the Appendices (A through D) contain detailed descriptions of some of the less standard experimental techniques used in my studies.

CHAPTER 2

2-D CRYSTALS OF COLLOIDAL DIMER PARTICLES

2.1 Introduction

One of the frontiers in colloidal physics is the self-organization of anisotropic particles into complex macrostructures. While numerous examples of particles with asymmetry either in terms of interparticle interactions or shape have been demonstrated [30, 39, 25, 23], producing such particles in sufficiently large quantities with low polydispersity remains a challenge. In this chapter, our procedure for synthesizing colloidal dimer shell particles is described along with the observed crystalline structure that is formed by the particles.[1]

2.2 Experimental System

The dimer particles are prepared through a multi-step templating process that produces hollow, fluorescent silica shells amenable to direct visualization with a confocal microscope. To synthesize the core hematite particles (α-Fe_2O_3), a condensed ferric hydroxide gel is first aged under hydrothermal conditions (Fig. 1a) [63]. A rhodamine-functionalized silica shell is then grown onto the hematite surface using modified sol-gel chemistry [65]. This protocol produces 95% pure dimer particles with final dimensions of $2.82\ \mu$m $\times 1.36\ \mu$m, and polydispersity 4.7%. The shell thickness ranges between 20-150 nm and is tuned via the silica precursor concentration and feed times. Since hematite has a high index of

[1] Much of the information in this chapter is taken from our manuscript [34].

refraction that hinders confocal imaging due to scattering, and a weak magnetization that alters the assembly process, we sacrifice the core through selective etching using concentrated hydrochloric acid (Fig. 2.1b). Complete removal of the hematite is confirmed by XRD measurements (Fig. 2.1c).

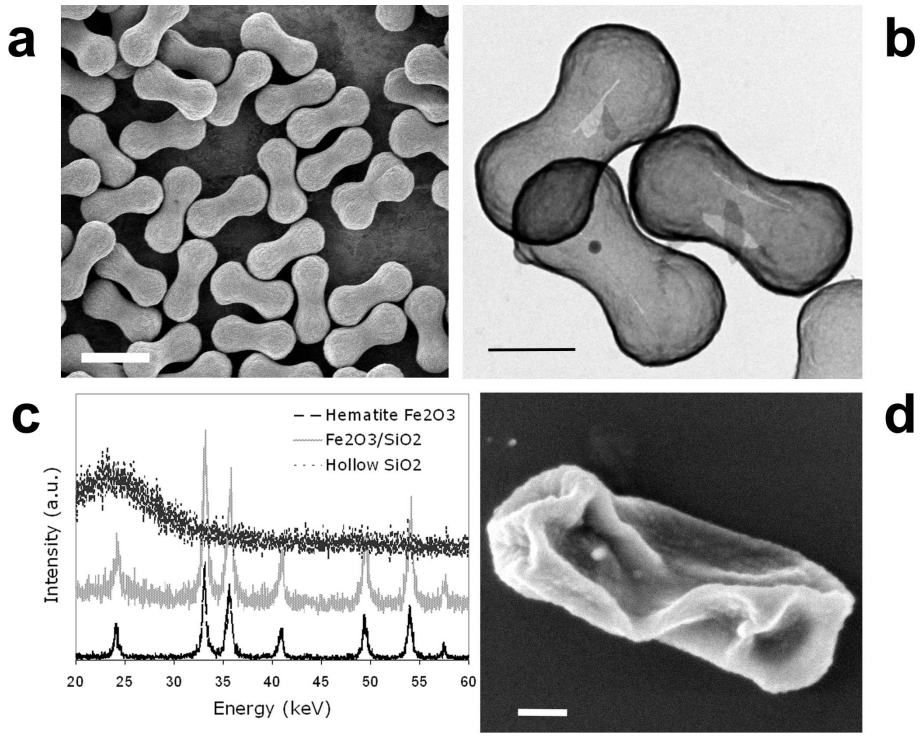

Figure 2.1: Fluorescent silica particles. (a) FE-SEM image of monodispersed hematite colloids from which hollow particles are templated. Scale bar, 2.5 microns. (b) TEM bright-field micrograph of intact silica shells (thickness, 65 nm). Scale bar, 1.5 μm. (c) XRD pattern of hematite particles (bottom, black), hematite-silica core-shell particles (middle, light gray), and hollow silica shells (top, dark gray). The bottom two show peaks corresponding to crystalline hematite (JCPDS card no. 33-0664), while the top exhibits only an amorphous signature indicative of complete etching. (d) Collapsed particle (thickness, 28 nm), illustrating a typical morphology below the critical thickness, t_c. Scale bar, 400 nm.

The dimer shells are structurally stable only when the shells are thicker than a critical shell thickness of about 40-50 nm. Below this thickness, hollow dimers

crumple without fracture and lose their intended shape (Fig. 2.1c). Increasing the silica precursor concentration leads to thicker shells, though coatings are limited to 60 nm depositions in a single step to prevent the undesirable nucleation of smaller, secondary silica particles. The particles are sterically-stabilized and suspended in an aqueous solution, yielding nearly hard core interactions.

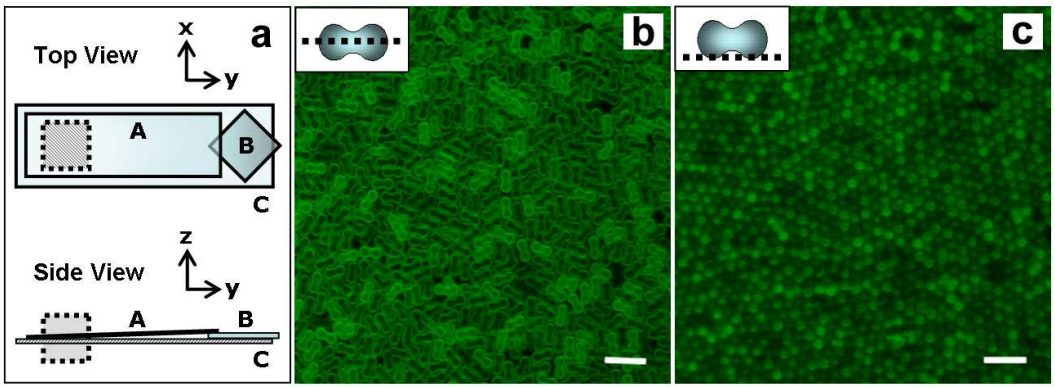

Figure 2.2: Confocal microscope images of dense monolayers of dimer particles. (a) Schematic of wedge-shaped confinement cell used to constrain the nonspherical dimer colloids. Details of the confinement cell construction are provided in Appendix B. The hatched area indicates a region where the gap height is roughly 1.5 μm. (b) Confocal image of a dense monolayer of colloids taken across the equatorial plane (inset, schematic view). Scale bar, 5 μm. (c) Triangular ordering of the lobes is revealed when an image is captured at a focal plane that just grazes the particle lobes (inset, schematic). Scale bar, 5 μm.

We investigate the ordering of a dense monolayer of dimer particles confined in a wedge-shaped cell depicted schematically in Fig. 2.2a. (A detailed description of the wedge cells is provided in Appendix B.) Particle area fraction is controlled by gently tilting the cell so that the dimers slowly sediment into the region of interest. Before imaging, the confinement cell is laid flat to allow for equilibration over the entire field of view.

2.3 Structure of the dimer crystals

The spontaneous organization of the colloids at high area fraction is shown in the confocal micrograph of Fig. 2.2b. Although the positions of the particle centers are aperiodic, an image captured at a focal plane that grazes only the particle tips reveals triangular ordering in the lobes (Fig. 2.2c). This symmetry is quantified by the form of the lobe pair correlation function, $g(r)$, taken over an area of 4800 μm^2 (Fig. 2.3a).

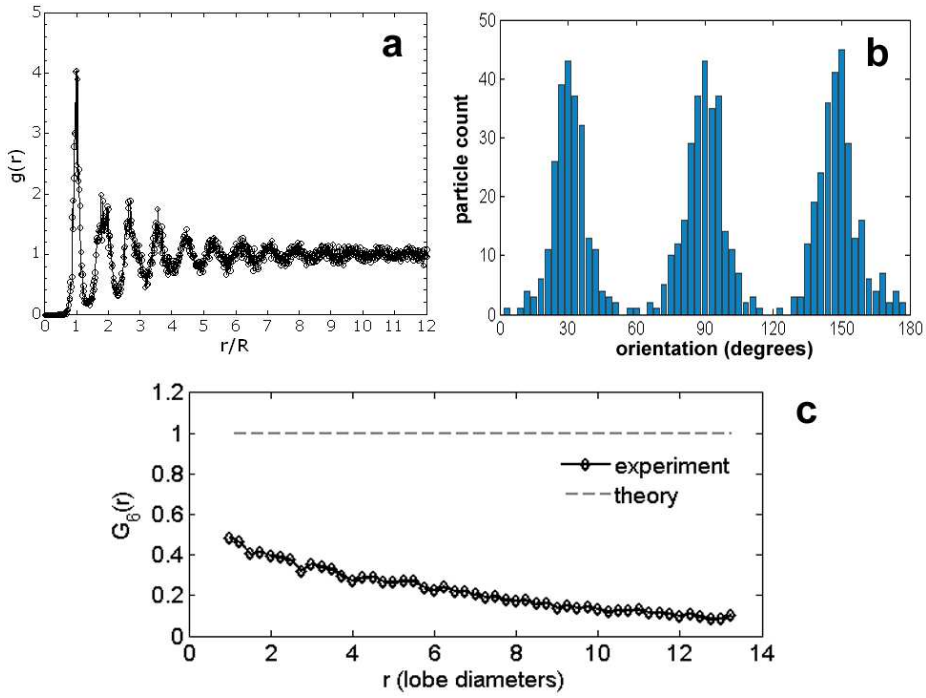

Figure 2.3: Structural characterization. (a) Lobe radial distribution function, $g(r)$. b) Histogram of particle orientations taken from various crystallites. The first peak measured from each grain is shifted to $\theta = 30°$. (c) The orientation correlation function, $G_6(r)$ for an ideal structure (gray hatched line) and our experimental system (black line). The latter shows a non-zero but decreasing long-range value, indicating that while interparticle angles are ordered close to multiples of $\pi/3$, crystal defects may be present.

As demonstrated by the trimodal distribution in Fig. 2.3b, the dimer particles are oriented with equal probability along the three crystalline axes defined by the lobes. In addition, because the interparticle angles occur predominantly at intervals of $\pi/3$, they can be well characterized by the orientation correlation function

$$G_6(r) = \left\langle \sum_{1 \leq i < j \leq N} \cos(6\ \Delta\theta_{ij}) \cdot \delta(r_{ij} - r) \right\rangle$$

where $\Delta\theta_{ij}$ is the difference in orientation for the ith and jth particles, and r_{ij} is the separation between their particle centers. The function $G_6(r)$ provides spatial information on the dimer orientations and expresses their degree of ordering to $\Delta\theta_{ij}$ values of $\frac{n\pi}{3}$, $n \in \mathbb{Z}$. Given perfect lobe positional order and dimer orientations, $G_6(r)$ should equal unity as seen in the theoretical curve of Fig. 2.3c. In the experimental system, $G_6(r)$ exhibits lower values due to the angular spread in $\Delta\theta_{ij}$ (Fig. 2.2b). It also displays a decaying long-range orientational order in the dimer axes, which may be suggestive of crystalline defects or grain boundaries.

The observed structure is reminiscent of the degenerate crystal (DC) which has thus far been seen only in Monte Carlo (MC) simulations of dimers with aspect ratio ≤ 2 [73]. As with our colloidal particles, in the simulated DCs, dimer lobes tile a triangular lattice while particle orientations are along any one of three crystalline directions. Such a phase exhibits strong configurational degeneracy, and was determined numerically to be the thermodynamically-stable phase [71]. An additional feature characterizing DCs is that the dimer centers irregularly decorate a kagomé lattice so that exactly one site is occupied in each

unit hexagon (Fig. 2.4a). Although the particles in the current study are elongated with aspect ratio 2.074, rather than shortened as in the MC simulations, the particle centers nevertheless satisfy this kagomé requirement (Fig. 2.4b).

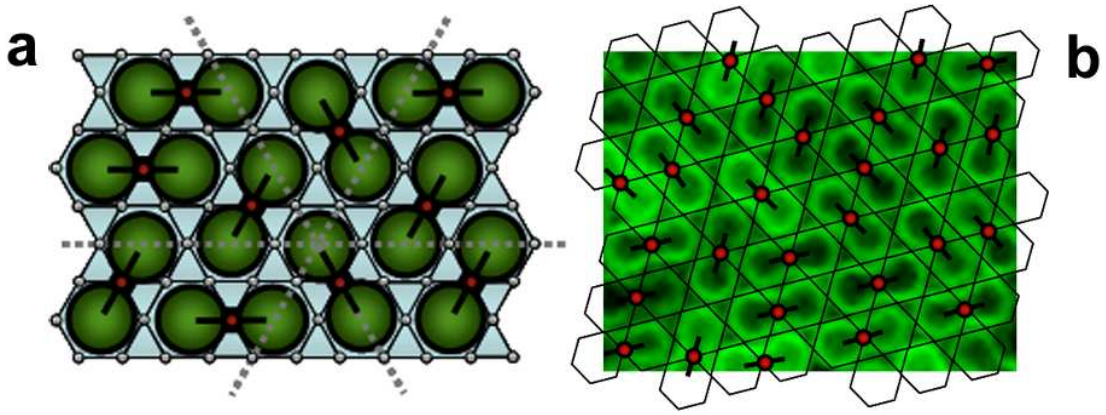

Figure 2.4: Kagomé construction of the Degenerate Crystal. (a) Schematic of the structure of the DCs observed in prior simulations [71]. Red dots represent the particle centers, white circles show the kagomé lattice sites, and dashed grey lines indicate the three crystalline axes (after [71]). (b) Kagomé construction applied to the experimental data with dimer colloids. The overlaid kagomé net is a guide for the eye.

2.4 Defects in the dimer crystals

A distinct difference between the simulated single-grain DCs and the experimentally observed structures of colloidal dimers is that the latter contain many crystallites with an average dimension of 10 ± 1 lattice constants (LC). This small grain size is reflected in the lobe pair correlation function, whose peaks decay beyond this length scale (Fig. 2.3a). Fig. 2.5a highlights the defect distribution in a typical sample using a Voronoi reconstruction, in which every particle lobe is colored according to its coordination number. This schematic reveals that while

some defects are isolated, many coalesce into string-like grain boundaries separating DC crystallites of different orientations. The mean fraction of defects is 15% and of those, 61% are located on the grain boundaries. While the individual defects are not frozen in place, the total number of defects remains nearly constant over a timescale of weeks. This observation of defect mobility in the experimental DC is in stark contrast to defects in crystalline monolayers of hard spheres with comparable particle size and area fractions, which anneal over a timescale of hours.

The importance of defect mobility lies in its crucial role in determining many material properties ranging from yield and plastic flow to work hardening and fatigue [46, 50, 64, 10]. In crystals of spheres, the motion of defects is achieved through simple particle rearrangements. In the dimer system, however, each lobe is permanently attached to one of its neighbors, and thus a rearrangement necessitates not only a translational but also an orientational change.

To illustrate the significance of this lobe pairing on defect annealing, and consequently on defect fractions, MC simulations of 2-D crystals of spheres formed under compression are compared to similarly formed 2-D crystals of dimers. We model ideal monodisperse particles in an isothermal ensemble starting from a disordered state at low density. The system is then compressed by incrementally increasing the pressure until it crystallizes (Fig. 2.5b,c). In the simulations, compression rates are varied by changing the number of MC cycles used for equilibration at each pressure. Fig. 2.5d illustrates that crystals of dimers have a higher fraction of defects than crystals of spheres at all compression rates. Furthermore, this effect is more pronounced at higher compression rates, where the fraction of defects increases for dimers but remains nearly zero for spheres.

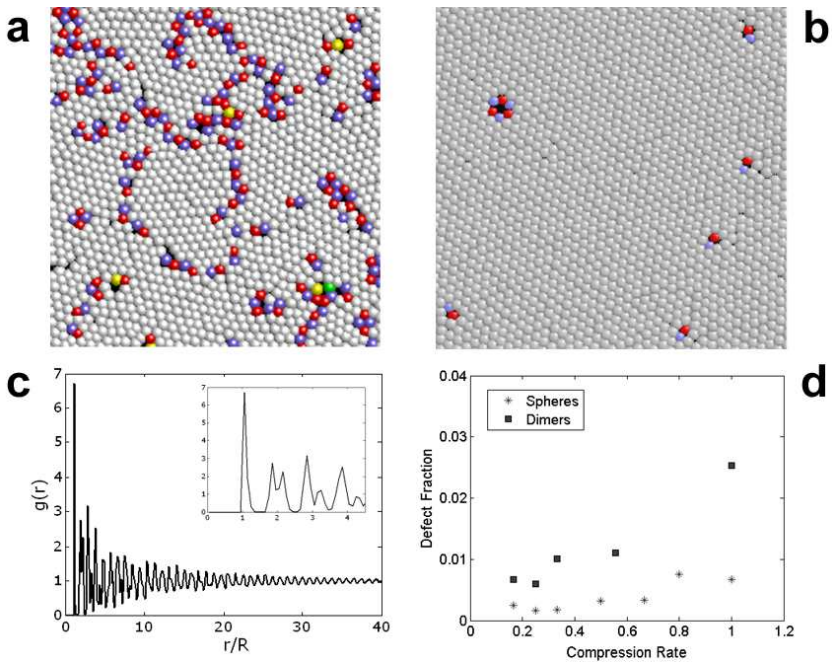

Figure 2.5: Defects and Monte Carlo simulations. (a) Voronoi reconstruction for experimental data, showing $N = 2394$ particle lobes color-coded by their coordination number. Defect lobes with a coordination number other than six are highlighted with non-white colors. (b) Voronoi reconstruction from MC simulations at a compression rate of 0.17. A magnified region of the total sample area ($N = 7200$ lobes) is shown for clarity. (c) Lobe pair correlation function associated with the simulation set from b. Inset, magnified view of the first few peaks. (d) Comparison of the defect fraction in crystals made of dimer particles (black squares) versus spherical particles (gray asterisks) at various compression rates. Trend lines are added to guide the eye.

Together with our experiments, these simulations suggest that defect dynamics in DCs is considerably more constrained than in crystals of spheres. Future investigations should help to clarify the differences in defect transport between the two systems. In addition, it would be interesting to probe whether DCs have a hexatic phase with long-range orientational order and short-range translational order. However, such a phase is challenging to identify, particularly in hard-sphere or polycrystalline systems.

2.5 Conclusions

The present report illustrates that proper selection and synthetic control of colloidal building blocks can open opportunities for the self-assembly of materials with novel structures, as exemplified by the observed DCs. Further studies, such as transition path sampling simulations and nucleation and growth experiments, should help to elucidate the mechanisms of the isotropic to DC phase transition. It may also be possible to design new assemblies of these particles by introducing further interactions with templated substrates. Most importantly, our studies of these simple anisotropic particles hint at the diversity of assemblies that can be constructed using nonspherical colloids. As such, it represents a positive step toward achieving molecular mimicry, whereby self-organization of systems with novel properties is driven by codes embedded within the constituent building blocks.

2.6 Supplementary materials

2.6.1 Monte Carlo simulations

In the Monte Carlo (MC) simulations, monolayers of dimer or spherical particles ($N = 3600$ dimers or $N = 7200$ spheres in each simulation) are compressed until they crystallize. The dimers are modeled as two spheres whose centers are located a distance of 1.075 particle diameters apart. The samples are kept at isothermal conditions throughout the simulations. Compression is induced by increasing the pressure in steps and allowing for equilibration at each step

using translation and rotation of randomly chosen dimers, with an acceptance rate based on the Metropolis criteria.

We initially define the compression rate as the ratio of the Gibbs free energy difference, ΔG, between initial and final pressures P_1 and P_2, to the total number of MC cycles in millions of cycles. The value of ΔG is chosen to be equal in crystals of spheres and crystals of dimers, thus providing the same thermodynamic driving force toward compression, even though crystallization for the two systems occurs at different area fractions. Because ΔG is constant, we can then simply redefine the compression rate as the reciprocal of the millions of MC cycles used to go from P_1 to P_2.

The Gibbs free energy difference ΔG is determined from

$$\Delta G = \int_{P_1}^{P_2} A \, \mathrm{d}P$$

where A is the total surface area of the system, and P_1 and P_2 are chosen so that:

1. $P_1(P_2)$ is well inside the isotropic(crystal) branch of the equation of state.
2. The value of ΔG between P_1 and the isotropic-crystal transition pressure P_* and the value of ΔG between P_* and P_2 are equal in both the dimer and the sphere systems.

The integrations are evaluated based on the equilibrium equation of state data. For the spheres: $P_1 = 5$ (area fraction, $\phi = 0.601$) and $P_2 = 14.8$ (equilibrium $\phi = 0.785$); For the dimers: $P_1 = 3.4$ ($\phi = 0.624$) and $P_2 = 13.0$ (equilibrium $\phi = 0.843$). The compression rate is maintained at a low enough value to allow

the systems to approach the final equilibrium area fraction and crystallize. Since we find that crystals of spheres always form single grains, simulation results are also restricted to those that formed single DC grains in order to compare the two systems on an equal basis.

CHAPTER 3

VACANCIES IN DEGENERATE CRYSTALS OF COLLOIDAL DIMERS

3.1 Abstract

Recent experimental observations of long-lived defects in crystals of colloidal dimer particles have prompted the question of how vacancy defects move in such crystals. In this chapter, Monte Carlo simulations of vacancy motion are described for both initially aligned and initially randomized dimer crystals. These simulations indicate that vacancies in dimer crystals are restricted by certain particle orientations. Interestingly, the restrictions on vacancy motion rarely lead to a scenario where a vacancy is completely trapped in a finite cage. Furthermore, even in the unusual scenario where a vacancy is trapped, it can still be released through cooperative interactions with additional vacancies in the system.[1]

3.2 Introduction and experimental setup

Recent experiments on self-assembled 2-D structures of colloidal dimer-shaped silica particles have determined that at high area fractions, the ground state of the system is the 'Degenerate Crystal' (DC) structure first proposed in simulations by Wojciechowski [71]. In this phase, the particle lobes occupy triangular lattice sites while the particle centers appear disordered. Further investigation reveals that the dimer centers actually are not randomly situated; they sparsely

[1]The information in this chapter is taken from my response to Jim Sethna's A Exam question.

decorate a kagomé lattice. An exemplary pair of confocal microscope images demonstrating the DC phase is shown in Figure 3.1. In the first image, a focal slice through the dimer centers displays a dense arrangement of unaligned dimers in apparently random positions, while in the second image, a triangular ordering of the lobes is revealed.

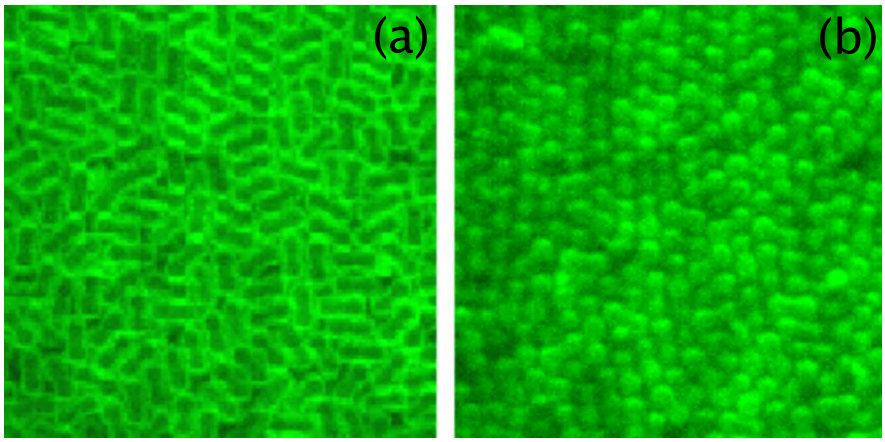

Figure 3.1: Confocal images of a Degenerate Crystal grain of dimer particles. A focal slice through the dimer centers looks disordered (a), but a slice through the tips resembles close-packed spheres (b).

A detailed description of the experimental system is provided in [34]. Briefly, the particles are sterically stabilized fluorescent silica dimer shells consisting of two approximately spherical lobes with diameter $D \approx 1\ \mu m$, separated by a small distance on the order of $0.07D$.(Figure 3.2). The significance of the lobe spacing is to allow the lobes to crystallize with a lattice constant slightly greater than D, giving the lobes some free volume surrounding their lattice positions. A detailed treatment of the effect of lobe separation on the phase diagram using simulations is described in [71]. The dimer particles are suspended in water and are confined in 2-D wedge-shaped confinement cells in which they are restricted to lie in the plane (details of the confinement cells are provided in Appendix B). The particles are slightly density mismatched (density mismatch ~ 0.5 g/mL)

in the water, a fact which is exploited to tune the particle area fraction. The particles are then observed using a Zeiss 5 Live confocal microscope.

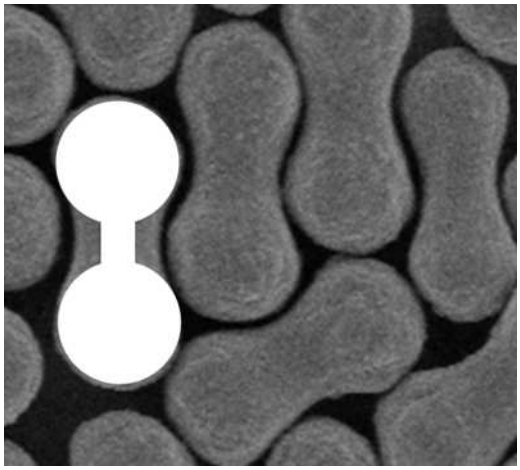

Figure 3.2: Scanning Electron Microscope image of the fluorescent silica dimer shells. A stretched dimer is overlaid in white as a guide to the eye.

3.3 Experimental results

The DC phase may be quantitatively verified by using image analysis to locate the positions of each dimer lobe. The *lobe* pair correlation function $g(r)$ is then calculated using the lobe positions. Fig. 3.3a shows the pair correlation function of a typical experimental DC configuration. The distinct peaks suggest crystallization, but they damp out quickly, indicating imperfect lobe crystallization in the sample. The DC phase was further corroborated by Monte Carlo simulations as described in [34]. The pair correlation function of the simulated DC phase is shown in Fig. 3.3b, and the sustained, undamped peaks indicate that the simulations produced DC configurations with fewer defects.

To elucidate the origin of the damping in the experimental $g(r)$, coordina-

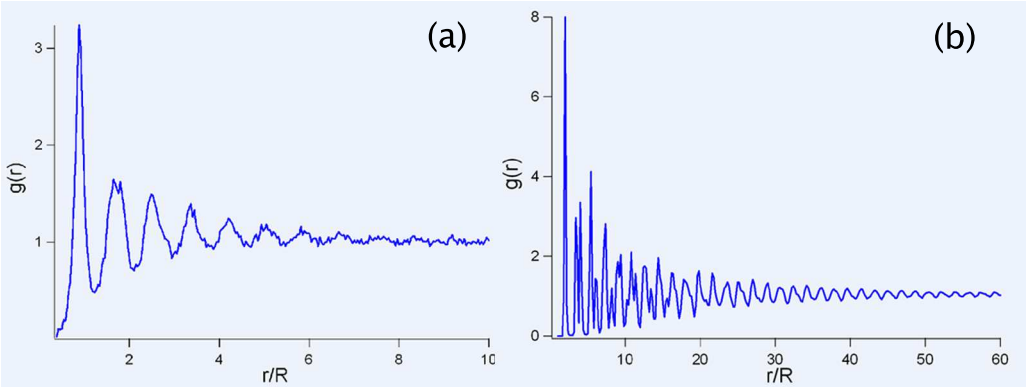

Figure 3.3: The pair correlation function $g(r)$ for experimental data (a) and for simulated data (b).

tion number diagrams are calculated for the lobe positions, using the Voronoi technique to define nearest neighbors. A typical coordination number diagram is shown for a high area fraction sample in Fig. 3.4c. This plot reveals domains of DC dimer lobes surrounded by defect rich, string-like boundaries. The pair correlation function dies out for pair separations beyond the average grain size. This result parallels a similar phase in colloidal spheres, in which crystalline domains surrounded by grain boundaries are formed.

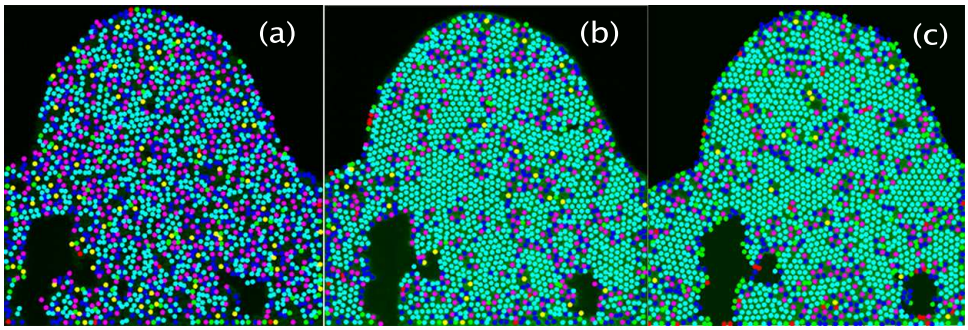

Figure 3.4: Microscope images overlaid with coordination number plots. The frames were imaged at time (a) $t = 0$ hours, (b) $t = 3$ hours, and (c) $t = 21$ hours. Between frames (a) and (b), the area fraction was slowly increased to near lobe close-packing. Coordination number key: light blue = 6, pink = 7, dark blue = 5, yellow = 8.

Coordination number plots and pair correlations are static 'snapshots' which only contain information about a lobe configuration at a particular moment. The striking difference between free spheres and bonded dimer lobes becomes evident when the dynamics are observed. In Fig. 3.4, three coordination number plots are shown for the same region at different times. Relative to the first frame, the second was taken at $t = 3$ hours, and the third was taken at $t = 21$ hours. In between the first two frames, the area fraction was slowly increased to a high value approaching lobe close-packing, and then was allowed to equilibrate. The notable feature in this time series is that, within the first half hour, many of the defects (defined as lobes having a number of nearest neighbors not equal to 6) have left the system, and small DC grains are visible. In the following 20 hours, very little defect annealing has occurred, even though individual defects have moved slightly. The basic defect arrangement is unchanged; the same grains visible in the second frame are present in the third. This slowing down of defect motion once the DC structure begins to form is the essential observation which differentiates the dimer lobes from their free-sphere counterparts.

One simple model for the observed defect slowing is based on the motion of dislocations in triangular crystals with lattice constant L. In a triangular crystal of free spheres, an edge dislocation consists of a pair of defect particles, one with five nearest neighbors, and the other with seven nearest neighbors (Fig. 3.5a). This 5-7 pair occurs at the end of an 'extra' row, when viewed along either of two crystal axes. The third crystal axis defines the direction for dislocation glide, the fundamental mechanism for dislocation motion in the crystal. Glide is enabled by the movement of the 7-fold coordinated particle along the glide direction (Fig. 3.5b). After the 7-particle has been moved by $\sim L$, it is now far enough from one of its 7 previous neighbors that it becomes a 6-fold coordinated parti-

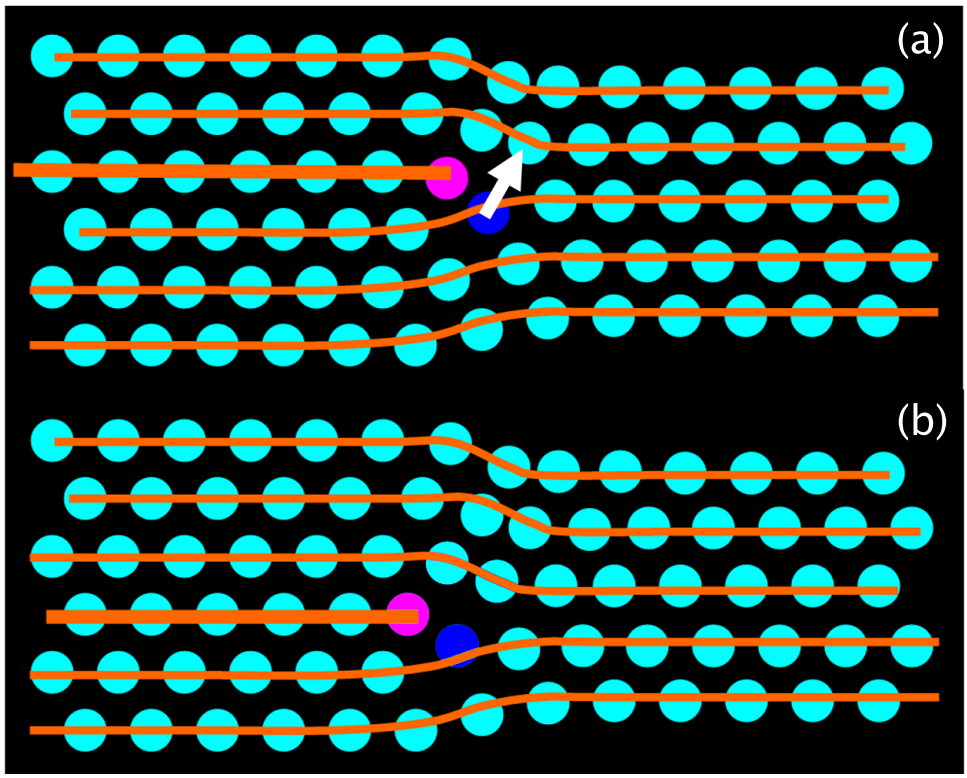

Figure 3.5: Schematic of dislocation glide in a triangular crystal of spherse. (a) An edge dislocation in a 2-D triangular crystal looks like one partial row and is made up of one 5-fold coordinated defect (pink) and one 7-fold coordinated defect (blue). (b) Slight shifting of the 7-defect particle moves the entire dislocation down by one row.

cle, while the old neighbor has become a 7-defect particle. The old 5-defect particle has also become a 6-fold particle in the process, and a new 5-defect particle has appeared next to the new 7-defect particle. In terms of crystal rows, the extra row of particles has now hopped down by one lattice constant L. The incredible feature of dislocation glide is that by only moving one particle, the entire dislocation has shifted down by one row. This energetically cheap mechanism for shifting around extra rows of particles is the dominant mode of dislocation motion in crystals of close-packed spheres.

In triangular crystals of dimer lobes, however, glide is no longer so easy. It is

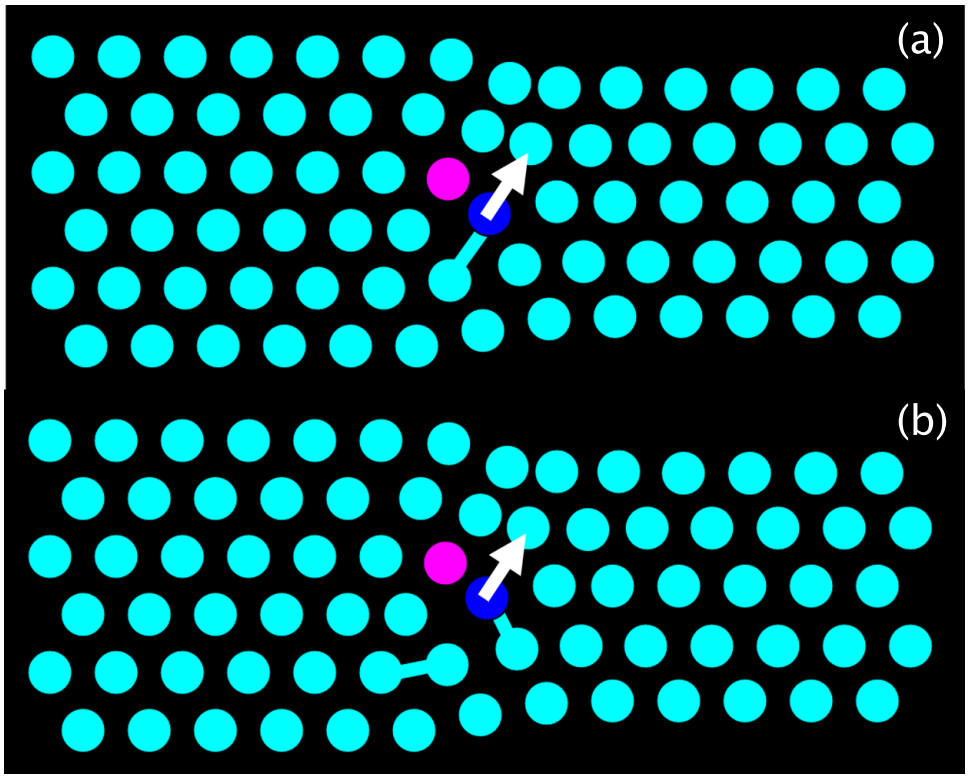

Figure 3.6: (a) Dimers aligned parallel to glide direction allow dislocation glide. (b) Interlocking particles block glide.

clear that glide can occur if the particles happen to be aligned with their dimer axis parallel to the glide direction (Fig. 3.6a). If, however, the particles surrounding the dislocation are interlocked, then glide is blocked (Fig. 3.6b). Observations of dimer orientations both in experiments and in simulations reveal that the DC phase consists of unaligned particles (Fig. 3.7). In fact, the correlations between dimer orientations fall off exponentially with separation distance r, indicating that while neighboring particles' orientation angles are slightly correlated, the orientation of one dimer is uncorrelated with, say, its fourth nearest neighbor's orientation. This exponential decay of orientation correlation means that in general, clusters of aligned particles will be only a few particles big, not nearly large enough to enable dislocation glide. At best, if the dislocation

happens to be located within a locally aligned cluster oriented along the glide direction, the dislocation could glide until it reaches the end of the cluster. Since the cluster sizes are small, this means that even such dislocations can only move a short distance before they encounter obstacles. Further studies are necessary to fully flesh out the picture of how dislocations are able to move through a DC.

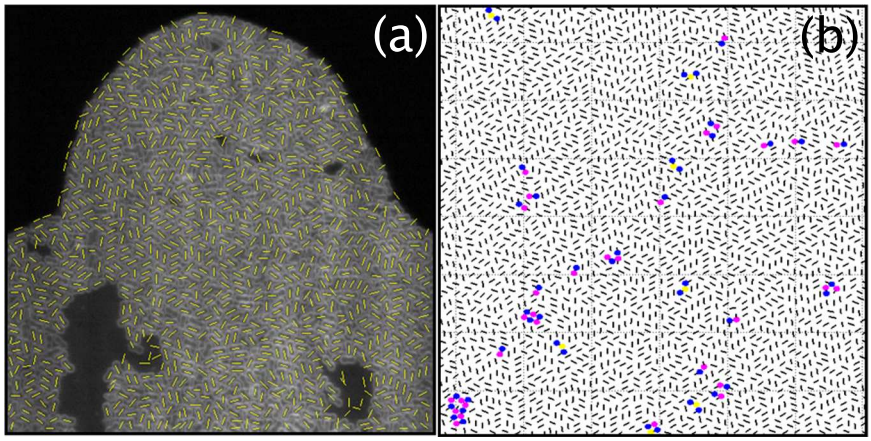

Figure 3.7: The particles in both experimental (a) and the simulated (b) DCs are randomly oriented.

3.4 Vacancy motion

In crystals of free spheres, vacancies diffuse freely. Because they have no topological charge, they do not cause local strain in the crystal, and there is no preferential position for them. Their diffusion in 2-D crystals mimics that of a 2-D random walk. Recent studies of vacancy diffusion in 2-D crystals of colloidal spheres have shown that certain combinations of vacancies move even faster than would be expected based on random walk diffusion. [48] This is attributed to the fact that the vacancies tend to break into pairs of repelling dislocations

which subsequently glide away from each other and then reform into new combinations of vacancies. The question of how vacancies move in a 2-D lattice of bonded dimer lobes is currently unanswered in the literature. The effect of dimer alignment on vacancy motion is also unstudied. Therefore, vacancy dynamics in a dimer lattice seems to be a rich problem with the possibility of producing some interesting insights.

3.4.1 Monte Carlo simulations

Simulations written in the Python programming language are used to study the motion of vacancies in both initially aligned crystals and crystals of disordered dimer particles. To create such crystals, dimer particle lobes are placed onto a triangular lattice. A vacancy is defined to be a lattice site that is not occupied by any dimer lobe. Simulation box sizes of about 100×100 lattice sites with periodic boundary conditions are used, and vacancy motion from a current vacancy position to one of its six neighboring lattice sites is allowed according to the following rules:

1. The neighboring site can not be occupied by a vacancy.
2. If the neighboring site is occupied by a dimer lobe, then the other lobe of that dimer must also be a neighbor of the vacancy.

In terms of dimer motion, this means that a dimer lobe can *swing* into a neighboring vacancy, but cannot *slide* into a vacancy (Fig. 3.8). Furthermore, only one lobe may move at a time. More moves could be incorporated by approximating the energetic cost E of the move and making the move with a prob-

ability equal to the Boltzmann factor $e^{-E/kT}$. This energetic cost can be roughly estimated by calculating the overlap area required for the move. Using this intuition, the cost of the sliding move is twice that of the swinging move (Fig. 3.9), and more complicated moves involving curved trajectories would be even more expensive. In the experiments, only the swinging move has been observed, and so this is the only move that is allowed in the Monte Carlo simulations.

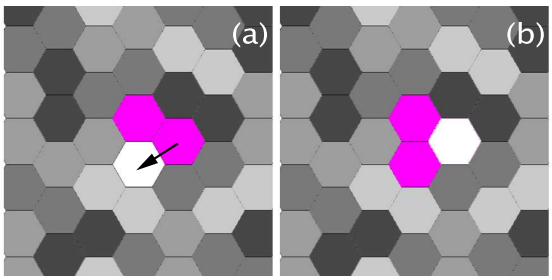

Figure 3.8: The allowed vacancy move corresponds to a dimer swinging one of its lobes into a neighboring vacancy. This is the only vacancy move that is observed in the experiments.

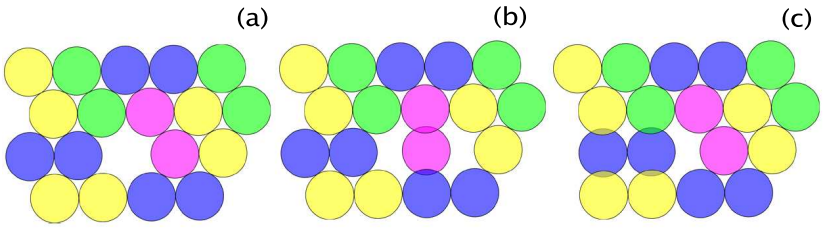

Figure 3.9: The energy cost of a dimer move can be estimated by considering the overlap area that would be required to make the move. (a) No overlap in the initial configuration. The overlap required for dimer swinging (b) is half that for sliding (c).

For initial conditions with multiple vacancies, a time step is defined as follows. In each time step, a random vacancy is chosen, and one of its six nearest neighbor lattice sites is randomly chosen. If the vacancy is capable of moving into that site, it does so, swinging the the dimer lobe which previously occupied the new vacancy site into the old vacancy site.

Aligned dimer initial conditions

Vacancy motion is first studied in an initially aligned crystal of dimers. Fig. 3.10a shows an initial configuration containing a pair of vacancies (colored white) created by removing a single dimer from the lattice. Because all the particles are aligned leaning toward the upper left, the upper vacancy can initially only move to the left, and the lower vacancy can initially only move to the right. As they move apart, they leave behind a wake of reoriented particles which can accommodate vacancy motion in either direction. If they happen to recombine, though, all the surrounding particles will once again be aligned along the original direction and the rule will apply again. Furthermore, the vacancies are both stuck within the dimer row in which they started, since the particles in the adjacent rows are blocking them from moving up or down. Fig. 3.10b shows another image of the same lattice after 1000 dimer moves (corresponding to 1374 time steps). In this image, particles occupying sites that have been visited by the vacancy are represented in grayscale rather than color. It is clear that the vacancies are trapped in their initial dimer row. This highly directed motion is in stark contrast with vacancy diffusion in free spheres, which is isotropic. It is possible that these vacancies diffuse more 1-D random walkers, but with the stipulation that they cannot cross paths.

If the initial configuration is changed slightly so that there is one isolated lobe-sized vacancy in a row, rather than a dimer sized divacancy, the results are similar. If the vacancy is in a top-lobe position, it moves to the left, and if it is in a bottom-lobe position, it moves to the right (Fig. 3.11). However, a strikingly different behavior occurs if two such vacancies inhabit the same row (Fig. 3.12a). Note that in the initial configuration, the particles just above each

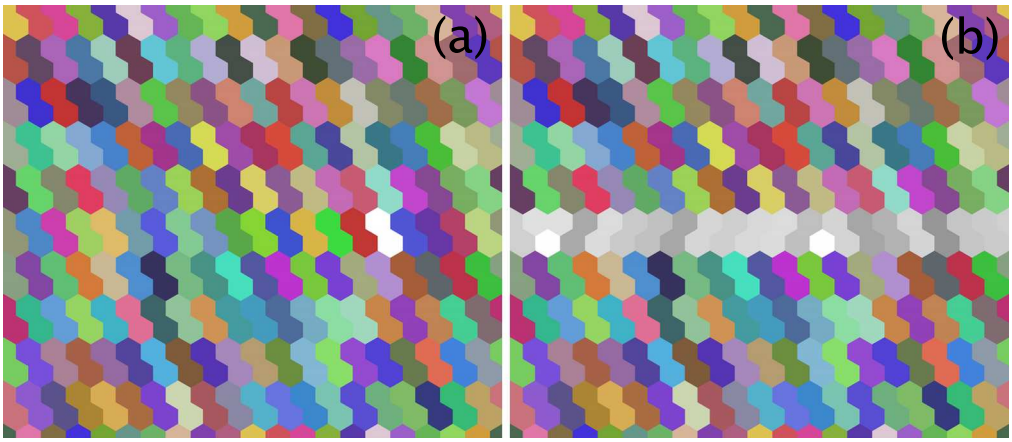

Figure 3.10: (a) A divacancy is created by removing one entiredimer from an initially aligned DC. (b) Lattice sites that have been visited by a vacancy in 1000 dimer moves are represented in greyscale.

vacancy have one lobe in the same row as the vacancy, and the other in the next row up. These particles are special 'ladders' linking the two rows, since if the vacancy can reach one of the positions occupied by the ladders, it can climb up to the next row and continue along to the right. Each vacancy cannot use its own ladder, which is why the result for a single lobe-sized vacancy is the same as it was for a dimer-sized vacancy.[2]

The presence of a second bottom-lobe vacancy to the right of the first bottom-lobe vacancy enables the left vacancy to reach the next row, using the second vacancy's ladder to pull itself up. If the right vacancy is fixed in place, the accessible realm for the first vacancy stretches from its initial position to the site of the second vacancy on its initial row, and then from the second vacancy on to the right on the next row up (Fig. 3.12b). We note that in this case, the moving

[2]Actually, because the simulation is defined with periodic boundary conditions, this is not quite true. The vacancy can reach the right edge of the image and then wrap around to the left side of the row, and continue along until it reaches its own ladder. This effect, however, is entirely an artifact of the simulation boundary conditions, and, in the limit of an infinite system size and would cease to occur in the limit of infinite box size.

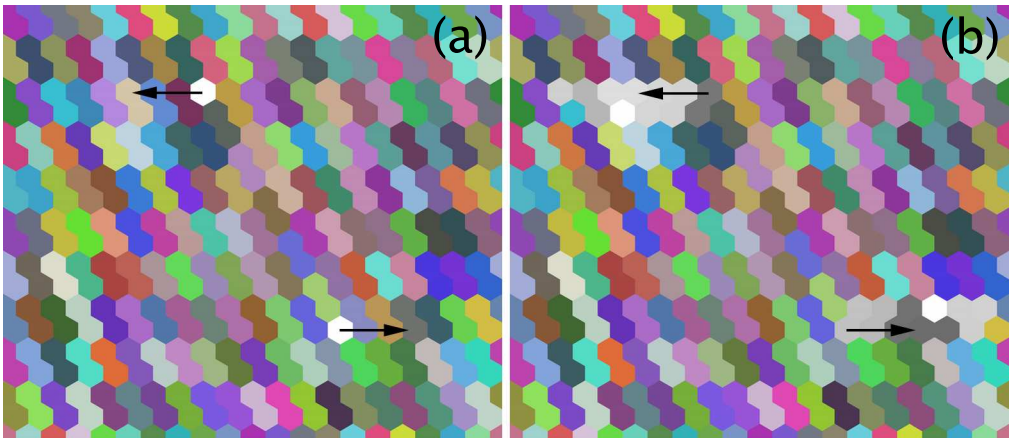

Figure 3.11: (a) One top-lobe vacancy and one bottom-lobe vacancy are shown in their initial positions. (b) The top-lobe vacancy moves to the left, while the bottom-lobe vacancy moves to the right. Sites visited by a vacancy in 100 dimer moves are represented in grayscale.

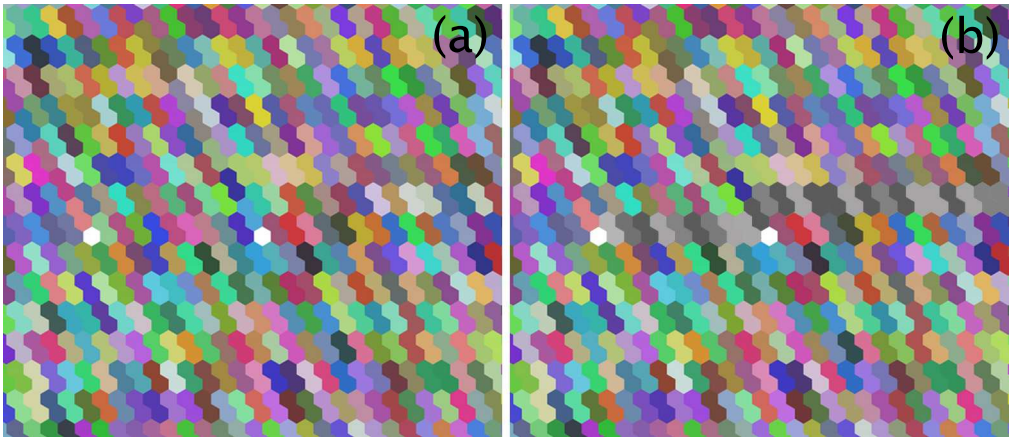

Figure 3.12: (a) Two top-lobe vacancies in a single row. (b) The accessible region for the left vacancy if the right vacancy is fixed is shown in gray.

vacancy cannot reach sites to the right of the fixed vacancy on the initial row, since all of the particles in that row have only one lobe exposed to the next row up. Incidentally, if both vacancies were bottom-lobe vacancies, the mirror image would occur: the right vacancy could move left and then use the second vacancy's ladder to hop down one row.

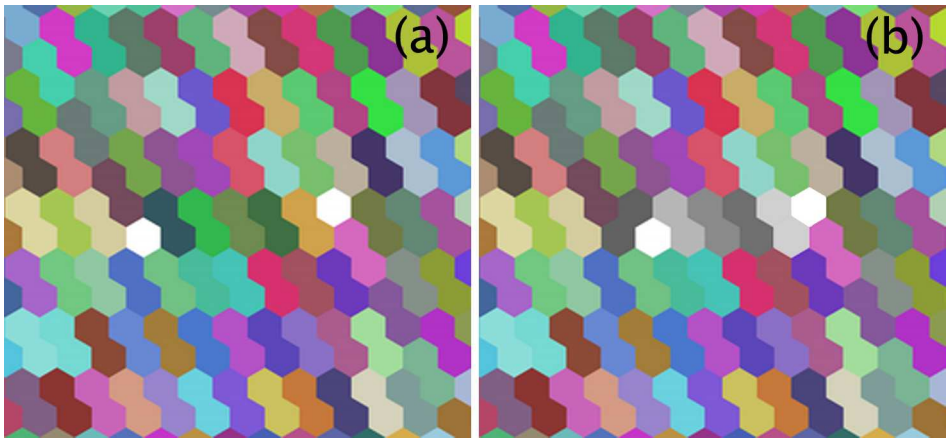

Figure 3.13: One top-lobe vacancy and one bottom-lobe vacancy in a single row before (a) and after (b) 1000 dimer moves.

If two vacancies are within the same dimer row, but one on the left is a top-lobe vacancy while the right vacancy is fixed in a bottom-lobe vacancy, then the left vacancy is trapped within its starting dimer row in the small segment separating the initial vacancy positions (Fig. 3.13).

The picture becomes much more complicated for a system of two same type (both bottom-lobe or both top-lobe) vacancies in the same row if both vacancies can move. Fig. 3.14 shows a time series in the vicinity of a bottom-lobe vacancy. Not pictured in Fig. 3.14a is another bottom-lobe vacancy on the same row, to the left. If that left vacancy were to move to the site initially occupied by the lower lobe of the ladder dimer (colored bright pink) before the right vacancy moved, it would be barred from continuing on its initial row, because there would be no dimer with both lobes neighboring that site. However, if the right vacancy shown in Fig. 3.14a were to move to the right, it would leave behind a wake of reoriented particles, including the (mauve) dimer immediately next to the ladder dimer. After this reorientation, if the left vacancy moves to the site of the lower lobe of the ladder, it could then move down into the tilted mauve

dimer just below the ladder. This is one very simple example of how nearby vacancies can cooperate to enhance each other's mobility.

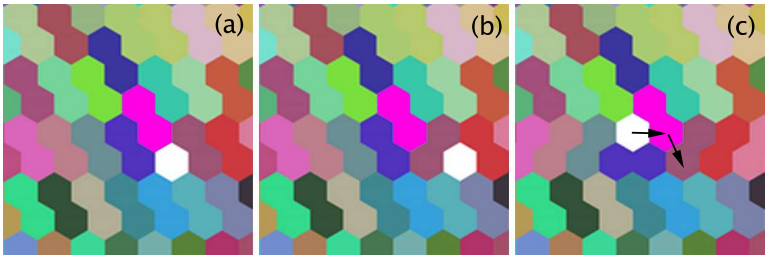

Figure 3.14: Ladder effect with two vacancies: a top-lobe vacancy on the left and a bottom-lobe vacancy on the right. (a) Initial configuration near the bottom-lobe vacancy. A second vacancy in the top-lobe position is out of the field of view to the left. (b) After the bottom-lobe vacancy moves, the nearby dimer (mauve) is reoriented. (c) Now the left top-lobe vacancy can move down from the ladder dimer (bright pink) to the reoriented dimer, entering the lower row.

The above descriptions provide a taste of the kinds of vacancy dynamics that are observed in systems of initially aligned particles. Even these few examples demonstrate the fact that vacancy motion in crystals of dimers is very different from their motion in a crystal of free spheres. While it is interesting to play around with various aligned systems, in order to make connection with the experimental observations of DCs, it is necessary to look at vacancy dynamics in systems of randomly oriented particles.

Randomly oriented dimer initial conditions

The task of creating an initial configuration of randomly oriented particles filling a triangular lattice (except for a few specified vacancies) turns out to be non-trivial. Luckily, K. W. Wojciechowski put a lot of effort into developing a method for sampling many different dimer configurations. [72] His technique

involves three multiple dimer reorientations, or 'switches', sketched in Fig. 3.15. Wojciechowski proved that these three moves are sufficient to ensure configurational ergodicity, since (1) it is impossible to create a random dimer configuration that does not contain one of the three clusters, and (2) these moves can transform any random dimer configuration into a perfectly aligned configuration. Wojciechowski used these switches to sample different dimer configurations when melting an initially defect-free random DC. His motivation for introducing the switches was that without them, the particles would remain in their initial orientation until the density dropped so low that each dimer could rotate freely without touching any neighbors.

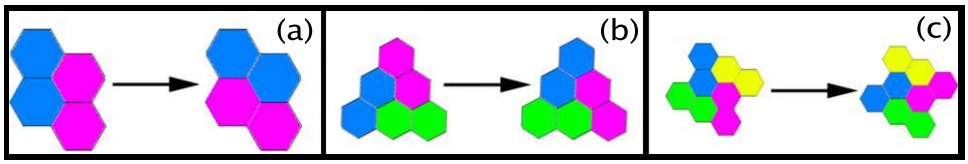

Figure 3.15: The 'bi-switch' (a), 'tri-switch' (b), and 'quad-switch' (c) reorient particles without changing their collective footprint on the lattice.

These Wojciechowski switches are used in the current study to transform an initially aligned configuration into an equilibrated random dimer configuration. The 'bi-switch' which rotates two particles is applied with probability 0.9; the 'tri-switch' and 'quad-switch' occur with probability 0.05 each. These probability values are taken from the Wojciechowski paper, where it was ensured that the probability of making each switch was equal to that of unmaking the switch; that is, detailed balance is upheld. Fig. 3.16 shows an initially aligned configuration and then the resulting configuration after 10^5 switches, a typical number of switches used to create a randomly oriented DC for the vacancy simulations. Once the random initial configurations are created, vacancies are allowed to move according to the same rules described above.

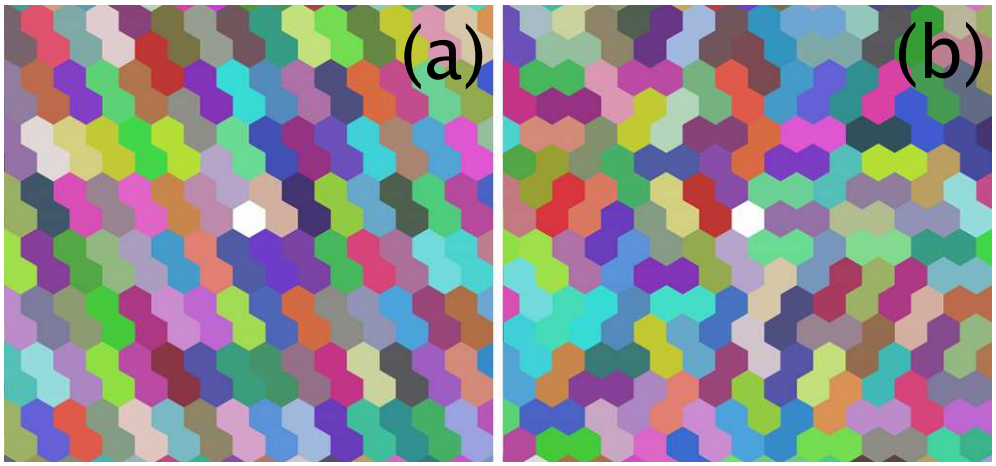

Figure 3.16: (a) An initially aligned dimer lattice. (b) The same lattice after 10^5 Wojciechowski switches.

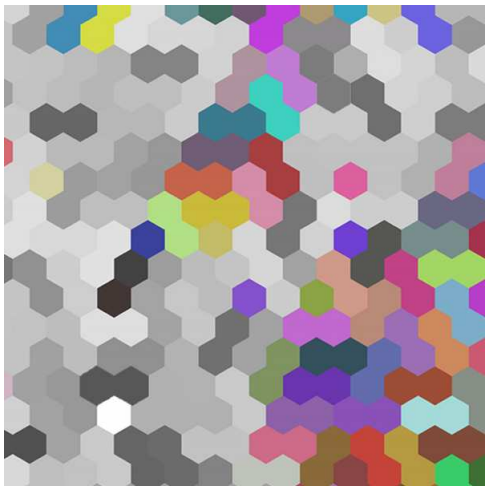

Figure 3.17: Most single vacancies in randomly oriented dimer lattices can visit all lattice sites. Here the sites visited within 10^3 dimer moves are shown in grayscale. The gray cluster percolates the system.

The results from these simulations are rather surprising, given how restricted the motion of vacancies was observed to be in aligned crystals. Most vacancies can move freely all over the system. After enough time steps (typically 10^3 for a system size of 20×20 lattice sites), the region that has been visited by the vacancy (colored gray in Fig. 3.17) percolates the system. This indicates

that in most cases, vacancies can visit all the lattice sites in random DC dimer configurations. However, the motion of the vacancies through the DC still looks slower than the standard 2-D diffusion observed for crystals of spheres.

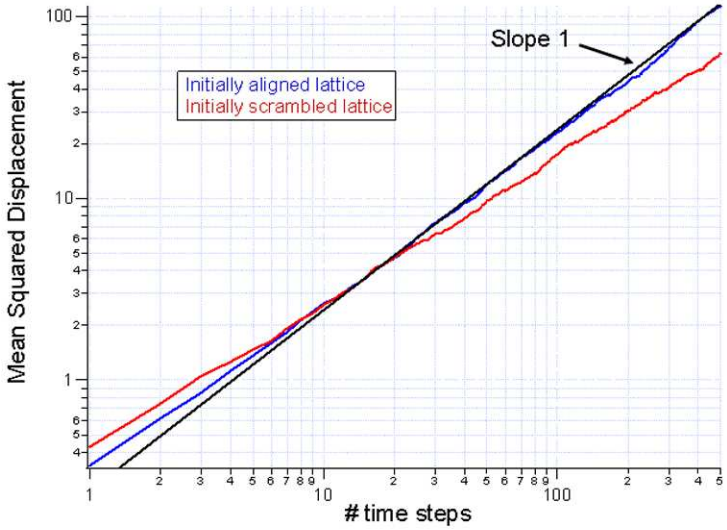

Figure 3.18: The MSD for vacancies in aligned dimer crystals (blue curve) and randomly oriented dimer DC crystals (red curve). The black curve represents an MSD of slope 1 on the log-log plot, representing what would be expected for a diffusive system. For waiting times up to 500 time steps, the motion of vacancies in DCs is subdiffusive.

In order to characterize the motion of the vacancies both in the aligned crystals and in the disordered DCs, the motion of vacancies is tracked between timesteps and the mean squared displacement (MSD $= \langle \Delta r^2 \rangle$) is calculated as a function of wait time δt, in units of time steps. The MSD for vacancies in aligned crystals and DCs is shown in Fig. 3.18. Interestingly, in the aligned dimer crystals, the vacancy MSD is consistent with 1-D diffusion, while in the DCs, the vacancy MSD is subdiffusive for waiting times up to $\delta t = 500$ time steps.

The observed subdiffusive behavior of vacancies in DCs for waiting times up to 500 time steps suggests that there could be some kind of caging occur-

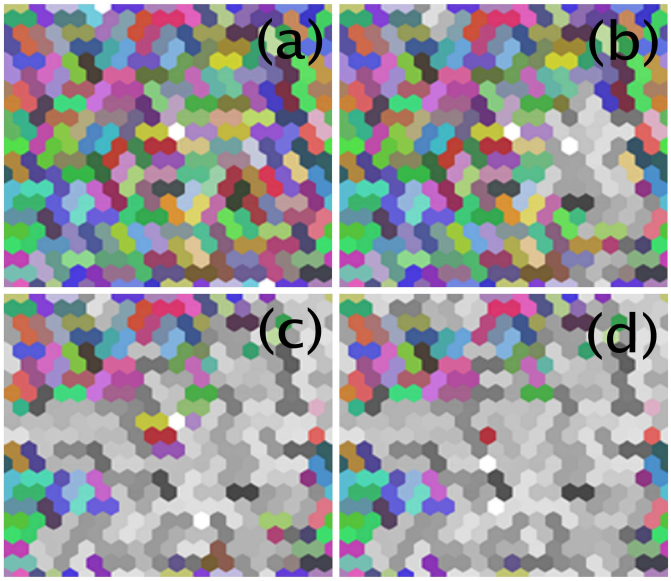

Figure 3.19: (a) Initially the central vacancy is stuck and the top left one is mobile. (b) After 60 moves, it is still stuck. (c) After 1400 moves, it is still stuck, even though the mobile vacancy has visited some neighboring sites. (d) After 1800 moves, it is finally released.

ring that restricts the motion of vacancies. In fact, it is possible for a vacancy to be completely caged by the particle configuration surrounding it. One example of such a configuration is depicted in Fig. 3.16b. Such vacancies will never move and have no diffusion whatsoever. However, in systems containing two vacancies, one of which is jammed and the other of which can diffuse freely, the free vacancy is capable of releasing the jammed vacancy by locally rearranging the particles nearby. In Fig. 3.19a, one vacancy (near middle) is stuck in a jammed configuration and another (top left) is mobile. In Fig. 3.19b, after 60 dimer moves, the mobile vacancy has navigated the periodic boundary conditions to enter the region to the right of the jammed vacancy. In Fig. 3.19c, after 1400 moves, the free vacancy has even visited sites neighboring the stuck vacancy, but still has not been able to unlock it. Finally, in Fig. 3.19d, after 1800 moves, the jammed vacancy has been released. This is another example of how

vacancies can cooperate to increase their mobility.

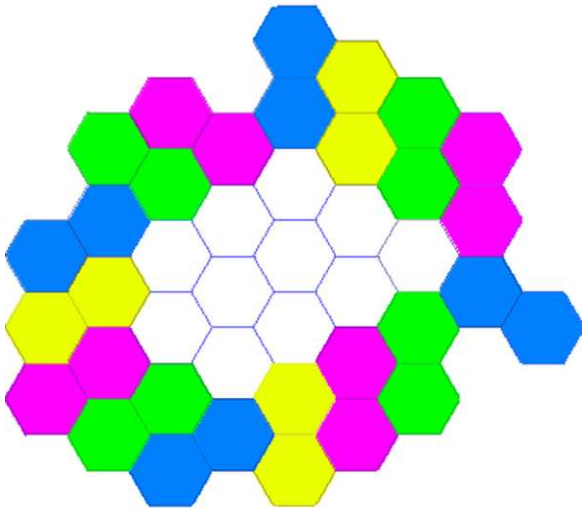

Figure 3.20: A theoretical cage containing 11 lattice sites. None of the surrounding particles are oriented in such a way that they can swing in to release the vacancy.

The jammed vacancies shown in Figures 3.16b and 3.19 are both caged in a very small region. The cage walls are defined by inward-pointing particles that do not lie parallel to the cage wall and therefore cannot be penetrated. It is certainly possible to create a cage of any particular size, see for example Fig. 3.20, which shows a cage of size 11 lobes. However, the larger the cage, the more aligned particles are needed to form the wall on a given side, and the less likely it is to produce one randomly. It would be very interesting to look at the distribution of cage sizes produced in random configurations made using the three switching moves. Incidentally, in order to find the cage limit for a particular vacancy, it is actually not necessary to run the vacancy movement simulation. Instead, the cage limit can be identified much more rapidly by using an analogous percolation rule: Color the vacancy position white. Then color subsequent particles white if both dimer lobes neighbor a white site. The white 'disease'

spreads very quickly, and tends to break down partial cage walls by reaching around them through small breaches and eating them from behind. Future investigations of cage size distributions could use this method to quickly find cages from an initial vacancy position.

3.5 Conclusions

Simulations of vacancy motion in crystalline arrangements of dimers have been studied for both initially aligned and initially randomized crystals. The results of these simulations indicate that there is a strong dependence of vacancy mobility on the local dimer configuration. In initially aligned crystals, single lobe-sized vacancies are trapped within their initial rows, and their motion is therefore highly anisotropic (though still diffusive). Multiple lobe-sized vacancies can cooperate to widen their realms of accessible positions. In initially random configurations, there is some distribution of the number n of unique lattice sites that can be reached by a lobe-sized vacancy. The results of the simulations described here indicate that this distribution contains only two values; either the vacancy is completely jammed and can occupy only $n = 1$ unique positions, or it can move to any position in the system: $n = N$, the system size. Theoretically, cages of all sizes n can exist, although it seems feasible that the probability of making such a cage would decrease with cage size.

Inspired by the above results, further simulations implemented by J. Schwarz and M. Jeng of Syracuse University have revealed that in the limit of large system size, the vacancy MSD in DCs eventually turns up and reaches a slope of 1, indicating that the observed subdiffusive nature of vacancy motion is

only short-lived. This suggests that vacancy diffusion is not the only important factor in determining how defects (lobes having a number of nearest neighbors that does not equal 6) move around in DCs. Further study of dislocations is necessary to fully understand why defects are so long-lived in these degenerate dimer crystals.

CHAPTER 4

RESTRICTED DISLOCATION MOTION IN CRYSTALS OF COLLOIDAL DIMERS

4.1 Abstract

At high area fractions, monolayers of colloidal dimer particles form a degenerate crystal (DC) structure in which the particle lobes form a triangular lattice while the particles are oriented randomly along any of the three lattice directions. We report that dislocation glide in DCs is blocked by certain particle orientations. The mean number of lattice constants between such obstacles is $\bar{Z}_{exp} = 4.6 \pm 0.2$ in experimentally observed DC grains, and $\bar{Z}_{sim} = 6.18 \pm 0.01$ in simulated monocrystalline DCs. Dislocation propagation beyond these obstacles is observed to proceed through dislocation reactions. We estimate that the energetic cost of dislocation pair separation via such reactions in an otherwise defect free DC grows linearly with final separation, hinting that the material properties of DCs may be dramatically different from those of 2-D crystals of spheres.[1]

4.2 Introduction

The microscopic motion of dislocations plays a crucial role in melting [32, 43] and governs numerous macroscopic phenomena observed in crystalline materials, including plastic flow, yield, and work hardening [46, 50, 64, 10]. Studies

[1]Much of the information in this chapter is taken from our manuscript [22].

of dislocations in colloidal crystals enable direct visualization of such processes [56, 57, 2, 76, 17, 18], providing an illustrative model for addressing fundamental questions in statistical physics and materials science. Thus far, such studies have focused on crystals of spherical particles, whose defect transport mechanisms are well described by existing models [46, 50, 64]. Advances in colloidal particle synthesis techniques have enabled the production of a variety of anisotropic yet monodisperse particles [39, 37, 27, 30, 4, 25, 23]. Dimer particles are a simple, fundamental extension of spherical particles and can be found in systems ranging from granular piles [53, 45] to paired adatoms in thin film epitaxy [52]. Furthermore, dimers are exceptional since although they are nonspherical, their constituent lobes can nevertheless occupy the lattice sites of crystal structures formed by hard spheres. The study of ordered phases formed by such particles therefore constitutes a natural expansion of the existing body of knowledge on crystals of spheres.

Here we directly examine the mechanisms for dislocation nucleation and propagation in a crystalline phase formed by dense monolayers of colloidal dimer particles. This crystalline phase, known as a Degenerate Crystal (DC), was first identified in simulations of dimer particles [73, 71], and is defined by the following two characteristic features. First, the individual dimer particle lobes form a triangular lattice; and second, the particle orientations are disordered, uniformly populating the three crystalline directions of the underlying lattice. We find that dislocation glide in DCs of colloidal dimers is severely limited by geometric constraints formed by certain particle orientations. This restricted dislocation motion suggests that the material properties of DCs may be dramatically different from those of crystals of spherical particles.

4.3 Confining the particles to a quasi 2-D layer

We observe dislocation motion in DCs comprised of hollow, hard dimer particles with spherical lobes of diameter 1.36 μm and lobe separation 1.46 μm. Using sol-gel chemistry, the rhodamine-functionalized silica particles are templated from dimer-shaped hematite cores and are sterically stabilized and suspended in an aqueous solution, yielding nearly hard-core interactions. A detailed description of the particle synthesis is provided in Appendix A. The synthesis procedure produces 95% pure dimer particles with particle polydispersity $< 5\%$. The suspension is pipetted into a sealed wedge-shaped cell, and particle area fraction is controlled by tilting the cell so that particles sediment into the viewing region, which accommodates a monolayer of particles. Before imaging with an inverted microscope, the cell is laid flat, allowing local equilibration until the area fraction is constant over the entire region of interest. The insertion procedure for filling a wedge cell creates small air bubbles; when these bubbles move near crystalline regions they induce defect formation and transport. A detailed description of the procedure for constructing the wedge cells is provided in Appendix B.

4.4 Dislocation nucleation and glide

The observed mechanisms for dislocation nucleation and glide are summarized in Fig. 4.1. Nucleation occurs when a single dimer particle, (highlighted in the image with a thick black dumbbell) rotates, creating a pair of dislocations (Fig. 4.1a,b). Glide is observed to occur either through a swinging move in which one particle lobe remains fixed while the other swings into a new crys-

talline position, or via a sliding move in which a particle translates along its axis. Swinging shifts the dislocation by one crystalline row, while sliding shifts it by two rows. A sequence of a sliding move followed by a swinging move is shown in Fig. 4.1c,d, where the sliding and swinging dimer particles have again been highlighted by thick black dumbbells.

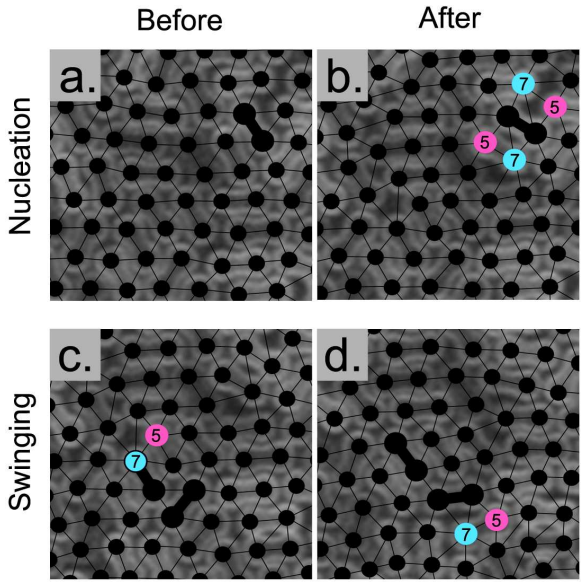

Figure 4.1: Before-and-after micrographs illustrating observed dislocation nucleation and glide moves. Particle lobes have been marked with dots, nearest neighbor bonds are indicated by lines, and dislocations consisting of paired fivefold and sevenfold coordinated lobes have been highlighted. (a,b) One rotating dimer particle (highlighted with a thick black dumbbell) nucleates a pair of dislocations. (c,d) A dislocation glides down by three rows through a combination of one sliding move (upper dumbbell) followed by one swinging move (lower dumbbell).

These observed mechanisms resemble similar mechanisms in crystals of spheres. In such crystals a pair of dislocations is created through the displacement of two adjacent particles (Fig. 4.2a). Each dislocation consists of one fivefold and one sevenfold coordinated particle and is characterized by a Burgers vector. The dislocations glide apart through a succession of moves in which

each sevenfold particle shifts its relative lattice position by moving in the direction of the Burgers vector. This process has the net effect of producing slip in the region between the dislocations, shifting the left side of the crystal upward and the right side downward in Fig. 4.2b,c.

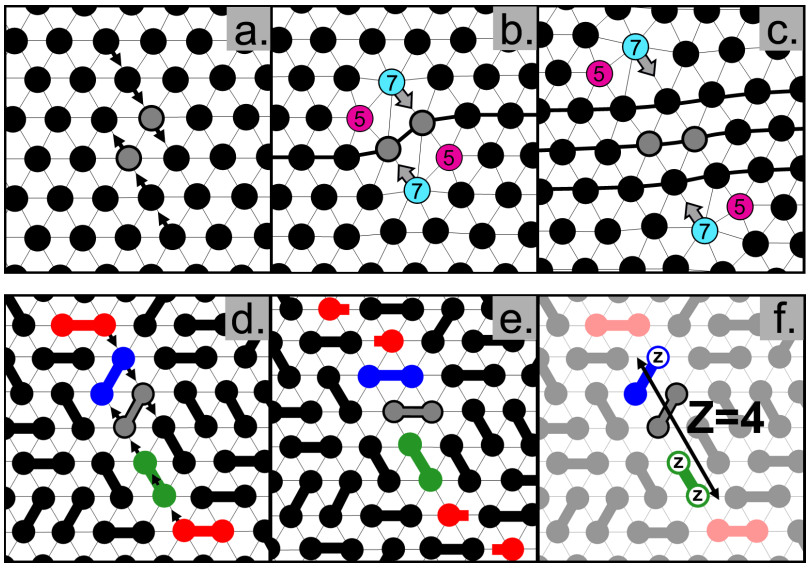

Figure 4.2: A schematic of dislocation nucleation and glide in monolayers of spheres (a - c) and dimer particles (d - f). (a,b) Displacing two spheres (gray) creates a pair of dislocations, each containing one 5-fold and one 7-fold coordinated particle. (b,c) The pair glides apart when the sevenfold particles shift parallel to their Burgers vectors (outlined arrows). (d) In DCs, a dislocation pair is created by rotating one particle (gray). Glide proceeds through the motion of the lobes marked with arrows, either by swinging (blue particle) or sliding (green particle). (e) The separation of a dislocation pair shears the crystal, which leaves swinging and sliding particles intact. The red particles, however, would have to be severed by this deformation, indicating that dislocation motion is blocked by such particle orientations. (f) The sequence of green and blue particles is a zipper of length $Z = 4$.

4.5 Unrestricted glide "zippers"

Guided by our experimental observations, we note that dislocation motion in DCs is restricted by the constraints of the local particle configuration. A schematic of a DC where dimers are represented by black dumbbells is shown in Fig. 4.2d. Nucleation occurs when a single dimer rotates as shown by the arrows on the gray particle. To allow for glide, the dimer lobes marked with arrows must shift in a manner similar to that shown for spheres. The critical difference is that while spheres are free to move independently, these lobes are constrained to move in collaboration with their partner lobes. The three types of particle orientations relative to the glide direction are illustrated by the green, blue and red particles in Fig. 4.2d. Green particles can shift both lobes in the desired direction by sliding, while blue particles can shift one lobe by swinging. Particles like these therefore permit dislocation glide, in concurrence with the experimental observations of swinging and sliding moves (Fig. 4.1c,d). The red particles, however, would need to be broken by the relative shifting of the crystal rows during the slip caused by glide (Fig. 4.2d,e). Since the particles in our suspensions do not break, the orientation of such particles blocks the motion of dislocations. Consequently, only sequences of consecutive swinging and sliding particles allow continuous glide. Since their glide-permitting motion is reminiscent of rearrangements in random square-triangle tilings, we define such sequences as 'zippers' [47]. In Fig. 4.2f, we highlight a single zipper. The zipper lobes, whose motion enables glide, are marked with a "z", and the zipper length, Z, is defined as one plus the number of zipper lobes.

In crystals of spheres, dislocations can glide arbitrarily far apart, but in DCs the zipper length defines their maximum glide separation. Consequently, dislo-

cation mobility in DCs is determined by the distribution of zipper lengths. The ensemble of all particle orientations that allow glide for dislocations produced by a clockwise rotation of one particle is shown in the inset of Fig. 4.3. Naively, one might expect to find a zipper of given length with probability $\rho(Z) \propto (2/3)^Z$ since $2/3$ of the particle orientations correspond to swinging or sliding moves. While this crude approximation accurately predicts that long zippers rarely occur, it overlooks important correlations between neighboring particle orientations.

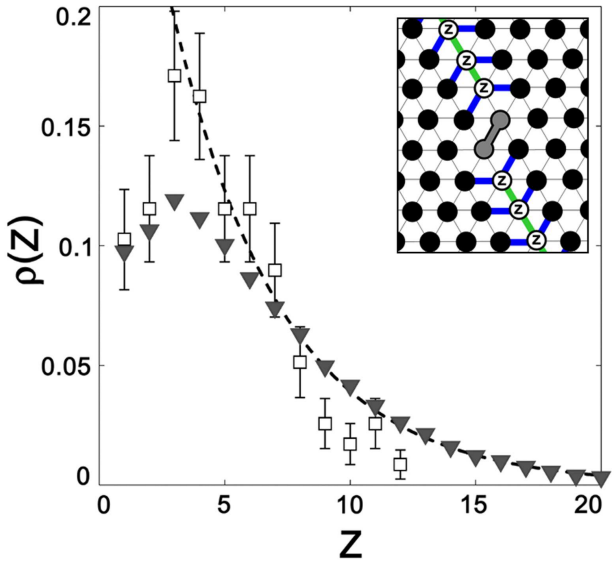

Figure 4.3: The distribution of zipper lengths in both experimental (empty squares) and simulated (solid triangles) DCs. Counting statistics determine the error bars, which for the simulations are smaller than the symbols. The average zipper length measured from experimental DC grains is $\bar{Z}_{exp} = 4.6 \pm 0.2$. Zippers in simulated crystals with 10^4 lattice sites are only slightly longer: $\bar{Z}_{sim} = 6.18 \pm 0.01$. The dotted line is the best fit exponential for $Z > 6$, having the form $\rho(Z) = 0.37e^{-Z/4.4}$. The inset shows the ensemble of glide-permitting particle orientations given nucleation via clockwise rotation of the gray particle. Particle configurations including a subset of these orientations enable glide via swinging (blue/dark gray) or sliding (green/light gray).

Precisely accounting for these correlations is theoretically challenging; in-

stead we directly measure $\rho(Z)$ from experimentally observed DCs. Zippers in DC grains are measured by randomly selecting a particle and counting the number of zipper lobes extending from it. We find that, on average, zippers are $\bar{Z}_{exp} = 4.6 \pm 0.2$ lattice constants long. [2] The mean diameter of the observed DC grains is 10 ± 1 lattice constants. Clearly, $\rho(Z)$ could be affected by this length scale. To determine the zipper length distribution independent of grain size, we prepare ensembles of large DCs using numerical Monte Carlo moves similar to those described in [71]. The simulations generate crystals with 10^4 lattice sites, but the mean zipper length is still only $\bar{Z}_{sim} = 6.18 \pm 0.01$ (Fig. 4.3). The tail of the simulated distribution is well characterized by the curve $\rho(Z) = 0.37e^{-Z/4.4}$, in agreement with predictions of exponentially decaying orientation correlations for dimers on a triangular lattice [41, 33].

4.6 Dislocation reactions

While zippers in DCs are on average only several lattice constants long, shearing or melting processes typically require the transport of dislocations over much larger distances. Our experimental observations reveal a mechanism for surpassing the zipper length limit via dislocation reactions. In such reactions two dislocations may combine or one may split apart so long as the sum of the Burgers vectors is conserved. These reactions allow dislocations to hop onto nearby zippers intersecting the glide path but oriented along a different crystalline axis. An experimentally observed dislocation reaction is illustrated in Fig. 4.4. In this sequence, a dislocation gliding down from the upper right approaches the end

[2] For all quantities $\bar{A}$ reported as $\bar{A} \pm \sigma_{\bar{A}}$, the error $\sigma_{\bar{A}}$ represents the standard error of the mean.

of its zipper. The defect undergoes a reaction and splits into two new dislocations. One dislocation's Burgers vector is aligned with the horizontal crystalline axis and glides to the left along an available zipper, while the second dislocation has moved to the lower right through a set of moves that are slightly complicated by the presence of a nearby grain boundary (Fig. 4.4b).

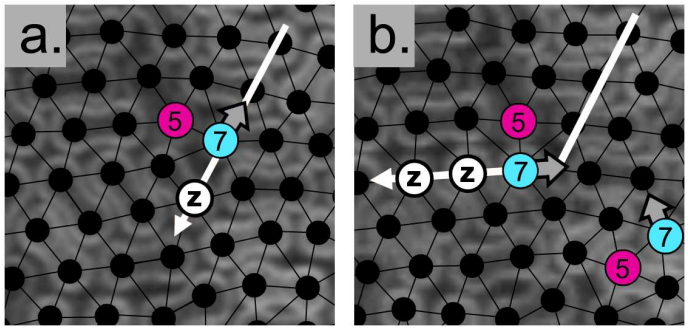

Figure 4.4: An observed dislocation reaction allowing a dislocation to hop from one zipper to another. Only the relevant defects have been highlighted, and their Burgers vectors are indicated by outlined arrows. (a) A dislocation gliding down from the upper right is one lobe from the end of its zipper. (b) The dislocation has reacted and proceeds by gliding down another zipper extending horizontally to the left. A second dislocation, visible to the lower right of the reaction site, was emitted to conserve total Burgers vector.

4.7 Estimate of energetic cost for arbitrary dislocation separation

Such reactions could enable dislocations to separate over arbitrarily large distances along a pathway of intersecting zippers. Nevertheless, the existence of such a pathway does not guarantee that dislocations in DCs are as mobile as those in crystals of spheres. To elucidate the difference between the dislocation

transport energetics in the two systems, we compare the cost of separating a single pair of dislocations over N lattice constants along the direction parallel to their Burgers vectors in an otherwise defect-free crystal. In crystals of spherical particles this energy increases as $E_s = \frac{\mu a^2}{2\pi(1-\nu)}\ln(N)$, where a is the lattice constant, μ is the 2-D shear modulus and ν is the poisson ratio [70, 18]. For dislocations separating via intersecting zippers in DCs, each dislocation reaction between zipper segments requires both a core energy to create new defects and a separation energy as one defect glides along the zipper [70]. The energetic cost of separating two dislocations by Na along their Burgers direction using the shortest pathway of connected zipper segments with length $Z_0 a$ increases linearly with N: $E_{DC} = \frac{\mu a^2}{2\pi(1-\nu)}\ln(Z_0)\left(\frac{4N+Z_0}{5Z_0}\right)$. A detailed calculation of this separation energy is provided in the supplementary materials at the end of this chapter. For crooked or fractal-like pathways this energy may increase as an even higher power of N. While dislocation reactions in which two defects merge can release energy, the presence of additional dislocations in the crystal does not guarantee that these would combine with defects produced at zipper junctions, as would be required to lower the energetic cost of separation. Furthermore, even though vacancy-mediated climb could be used to bypass certain obstacles, vacancy transport in DCs can only occur via sliding or swinging particle moves, and consequently dislocation climb is also restricted in DCs.

4.8 Conclusions

We expect that the material properties of DCs will be strikingly different from those of crystals of spheres. DCs will be more resistant to plastic flow since dislocation glide cannot proceed along a straight line, as is required for slip.

Furthermore, if the separation energy does grow linearly with N, we speculate that this will have important implications for melting. In the KTHNY theory of 2-D melting, the crystal to hexatic phase transition requires dislocation pair unbinding [32, 43]. The competition between the energetic cost of dislocation separation and the entropic contribution to the free energy, both of which increase as $\ln(N)$ for crystals of spheres, determines a unique melting temperature. If in DCs the separation energy increases as N, dislocation unbinding may no longer be feasible at any finite temperature. This suggests that melting in DCs may occur via additional mechanisms. Furthermore, the observed geometric restrictions in DCs may also apply to other dimer systems, such as lipids with dimer-like head groups [26] and granular dimers [53, 45]. For example, these restrictions help explain why avalanches in 2-D piles of dimer beads occur at relatively high critical angles and require tumbling rather than collective slip [45]. Additional comparative studies between crystals of spheres and DCs should further elucidate how the seemingly benign act of pairing particles into dimers introduces constraints that dramatically alter the material properties of the crystal.

4.9 Supplementary materials

4.9.1 Dislocation separation energy calculation

In crystals of spheres, nucleated pairs of dislocations with equal and opposite Burgers vectors $\pm\vec{b}$ separate by gliding apart along a straight line parallel to their Burgers vectors (Fig. S4.5a). This separation allows for relaxation of ex-

ternally applied shear stresses, and also enables the unbinding of dislocation pairs, which is a crucial component of the KTHNY model of 2-D melting. Using continuum models of dislocation interactions, the energetic cost of such a separation over N lattice constants is $E_s = \frac{\mu a^2}{2\pi(1-\nu)}\ln(N)$, where a is the lattice constant, μ is the 2-D shear modulus and ν is the poisson ratio [70]. In addition to this continuum interaction, there is also a core energy required to create the dislocations.

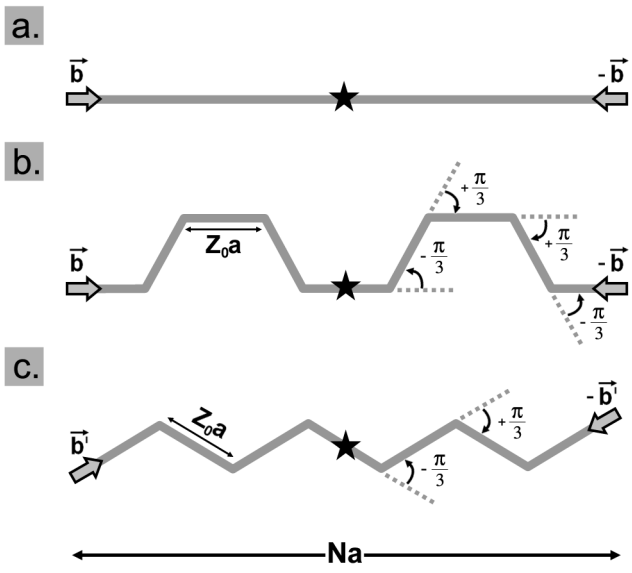

Figure 4.5: Pathways for dislocation pair separation in crystals of spheres (a) and DCs (b,c). Pair nucleation occurs at the location marked with a star in each pathway. (a) Dislocation pair separation is achieved through nucleation and glide along a straight line parallel to the direction of the defects' burgers vectors $\pm\vec{b}$. This process results in a pair separation of Na. (b) In an otherwise defect-free DC, an identical dislocation pair $\pm\vec{b}$ separates by Z_0a, the average zipper length, before undergoing dislocation reactions and traveling along a sequence of tilted path segments of length Z_0a. This pathway also results in a separation of Na along the burgers vector direction. (c) The shortest pathway with segment length Z_0a yields a separation of Na along a direction rotated by $\pi/6$ from the axis of the burgers vectors $\pm\vec{b'}$.

Similarly, the cost for separating a pair of dislocations with Burgers vectors $\pm\vec{b}$ in an otherwise defect-free DC can be estimated for any particular intersecting zipper pathway. For example, consider the pathway schematically depicted in Fig. S4.5b. In this scenario, two dislocations nucleate and initially glide apart along a straight line parallel to their Burgers vector, mimicking the situation observed in crystals of spheres. However, after separating by a characteristic distance $Z_0 a$, equal to the average zipper length, the defects each undergo dislocation reactions, turning to travel along a new zipper segment of length $Z_0 a$ extending along a different crystalline direction. At each reaction site, an extra dislocation is produced, which is assumed to remain stationary.

The energetic cost of separating the dislocations along the initial straight segment in Fig. S4.5b is $\frac{\mu a^2}{2\pi(1-\nu)}\ln(Z_0)$. Again, there is also an additional core energy required to create a new dislocation at the junction. Each additional segment requires more energy, and includes contributions from interactions between all the dislocations along the pathway. The magnitude of the force between dislocations decreases as the inverse of their separation. Consequently, the largest force on a dislocation moving on a given segment will come from the dislocation nearest to it. The energy required for such a separation is $E_{reac} = \frac{1}{2}\frac{\mu a^2}{2\pi(1-\nu)}\ln(Z_0)$. Adding up these energy contributions from each reaction, as well as the cost of the first straight segment, the total energetic cost for the pathway depicted in Fig. S4.5b is then

$$\begin{aligned} E_{DC}(Z_0, N) &= \frac{\mu a^2}{2\pi(1-\nu)}\ln(Z_0) + \frac{8(N-Z_0)}{5Z_0}E_{reac} \\ &= \frac{\mu a^2}{2\pi(1-\nu)}\ln(Z_0)\left(\frac{4N+Z_0}{5Z_0}\right). \end{aligned}$$

This separation energy grows linearly with final separation N, in contrast to the logarithmically growing energy for dislocation separation in crystals of spheres. We also note that this is a conservative estimate that excludes the additional core energy costs at each junction. In the limit that the average zipper length Z_0 approaches the separation distance N, the energetic cost obtained for crystals of spheres is recovered.

The above energetic cost estimation is only strictly valid for the particular scenario depicted in Fig. S4.5b. However, it represents a conservative energetic cost estimate for any pathway spanning N lattice constants along the initial Burgers vector direction, since any other option would require additional segments and dislocation reactions. If the defects are allowed to separate by Na along *any* direction, then the shortest possible pathway is the $-\pi/3$,$+\pi/3$ sequence shown in Fig. S4.5c. The energetic cost for separating along this path is $\frac{\mu a^2}{2\pi(1-\nu)}\ln(Z_0)\left(\frac{2N+\sqrt{3}Z_0}{2\sqrt{3}Z_0}\right)$, which still grows linearly with N. More crooked pathways with many more segments could result in an energetic cost of separation that grows as a higher power of N.

We note that in a real system, it is unlikely to find one isolated dislocation pair separating in an otherwise perfect crystal. The presence of a thermal bath of dislocations may enable other novel, less expensive mechanisms for pair separation.

CHAPTER 5

GLASSY DISLOCATION DYNAMICS IN CRYSTALS OF COLLOIDAL DIMERS

5.1 Abstract

Although glassy relaxation is typically associated with disorder, here we report on a new type of glassy dynamics relating to dislocations within an ordered crystal of colloidal dimers. Previous studies have demonstrated that dislocation motion in dimer crystals is restricted by certain particle orientations. Here, we drag an optically trapped particle through such dimer crystals, creating dislocations. We find a two-stage relaxation response where initially dislocations glide until encountering particles that cage their motion. Subsequent relaxation occurs logarithmically slowly through a second process where dislocations hop between caged configurations. Finally, in simulations of sheared dimer crystals, the dislocation mean squared displacement displays a caging plateau typical of glassy dynamics. Together, these results reveal a novel glassy system within a colloidal crystal.[1]

5.2 Introduction

Dislocation mobility is central to both the materials properties and relaxation mechanisms of crystalline materials [46, 50, 64]. Previous studies of dislocation motion in colloidal crystals composed of spherical particles have allowed a

[1]Much of the information in this chapter is taken from our manuscript [21].

particle-scale view of defect formation and transport [56, 36, 76, 13]. More recent experiments [22, 34] have begun to interrogate the role of particle anisotropy in determining the rules of defect motion. In particular, studies of dislocation motion in crystals of colloidal dimer particles have uncovered novel restrictions on dislocation mobility. In these "degenerate crystals", the dimer lobes occupy triangular lattice sites while the particles are randomly oriented among the three crystalline directions, as shown in Fig. 5.1. One consequence of the random orientations of the dimers is that dislocation glide is severely limited by certain particle arrangements in degenerate crystals [22].

The present work utilizes local mechanical perturbation experiments to investigate the effects of this restricted dislocation motion on the relaxation mechanisms in degenerate crystals of colloidal dimers. Holographic optical tweezers are used to manipulate single lobe-sized spherical intruder particles within an otherwise pure degenerate crystal grain, deforming the crystal and introducing defects. During the subsequent relaxation of the degenerate crystal, dislocations formed during the deformation leave the grain, either via annihilation with other dislocations or by moving to a grain boundary. Interestingly, we find that in large crystalline grains this dislocation relaxation occurs through a two-stage process reminiscent of slow relaxations in glassy systems, suggesting the novel concept that glassy phenomena may be present within certain kinds of colloidal crystals.

We synthesize sterically stabilized silica dimer shell particles with spherical lobes of diameter 1.3 μm and lobe separation 1.4 μm as previously described [22, 34]. For the spherical intruder particles, we include 1% volume fraction of 1.3 μm polystyrene spherical particles that are coated with silica and sterically

stabilized using polyvinylpyrrolidone (PVP) to produce surface chemistry identical to the dimer particles. All particles are suspended in an aqueous solution of dimethylsulfoxide (DMSO) that index-matches the silica shells (with density mismatch ~ 0.5 g/mL). The polystyrene cores of the spherical intruder particles remain index-mismatched, allowing for optical manipulation using laser tweezers. Thus, perturbations to the degenerate crystal are applied only via the motion of the intruder particle. The suspension is pipetted into a sealed wedge-shaped glass cell as previously described [22] and the particle area fraction (maintained at ~ 0.8) is controlled by tilting the cell so that particles sediment into the viewing region, which only accommodates a 2-D monolayer of particles. (A detailed description of the wedge cells is provided in Appendix B.) During the perturbation experiments, the crystal is imaged using a confocal microscope integrated with the holographic optical tweezer system (Arryx, Inc) [14].

5.3 Local mechanical perturbation using optical tweezers

In preparation for a local perturbation experiment, one intruder particle is moved to the center of a degenerate crystal grain, and then the system is allowed to relax for at least 10 hours until the grain is defect-free. Fig. 5.1a-c shows a typical drag experiment for a small degenerate crystal grain consisting of $N \approx 100$ dimer particles. At time $t = 0$ s (Fig. 5.1a) the optical tweezers are turned on and used to drag the intruder particle by one lattice constant (LC) along a lattice direction, arriving at the new lattice position at $t = 20$ s. Then the optical tweezers are turned off and the grain is imaged until all the defects leave the grain or recombine (Fig. 5.1c). Dislocations created by the drag defor-

mation are identified from the microscope images by calculating the number of nearest neighbors for each lobe using Voronoi analysis. Each dislocation, consisting of paired five-fold and seven-fold coordinated lobes, is tracked over the experiment.

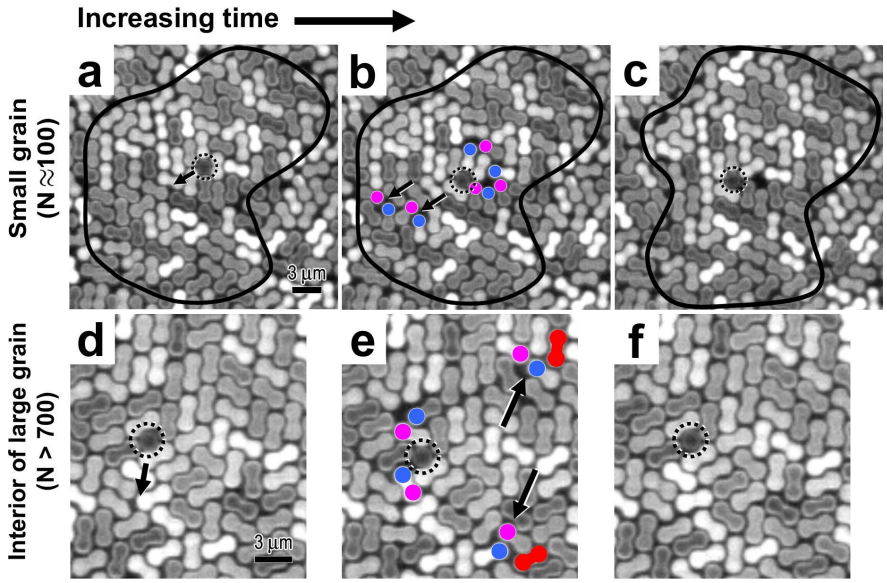

Figure 5.1: Micrographs illustrating a local perturbation experiment. Five-fold and seven-fold coordinated defects created by the perturbation are marked with pink and blue dots, respectively. (a) A single spherical intruder particle in a small grain is dragged by 1 LC using optical tweezers. (b) Two dislocations marked by arrows glide to the grain edge and are absorbed by the grain boundary (solid closed curve). (c) The intruder particle remains stationary after the tweezers are turned off. The vacancy left behind has no topological charge and is stable. (d-f) In a large grain (only the central part is shown here) the dislocations marked by arrows are obstructed by the particles in red. When the tweezers are turned off, the blocked dislocations return along their glide paths, recombining and causing the intruder particle to recoil.

5.4 Effect of grain size on response to perturbations

We observe different relaxation behavior depending on the degenerate crystal grain size. In small grains, the intruder particle remains stationary after being dragged to its new lattice position, even after the tweezers are turned off. In such cases, dislocations like those identified by arrows in Fig. 5.1b glide to the edge of the grain and are absorbed by the grain boundary, which we identify using Voronoi analysis (details in the supplementary materials at the end of this chapter). In larger grains (Fig. 5.1d-f), we observe that dislocations gliding toward the grain boundary are more likely to encounter glide-blocking particles whose orientations prevent further glide [22]. For example, the dislocations marked by arrows in Fig. 5.1e must travel so far to reach the grain edge (beyond the field of view of Fig. 5.1e) that they encounter the blocking particles shown in red. Consequently, when the optical tweezers are turned off, these dislocations return toward the intruder particle, recombining with the other defects produced by the deformation, and causing the intruder particle to recoil.

To elucidate the effect of grain size on the recoil distance of the intruder particle we conduct 19 independent deformation experiments on degenerate crystal grains of varying size. We find that a crossover from the stationary response to the recoiling response occurs when dislocations produced during the deformation must traverse distances $Z > 10$ LC to reach a grain boundary (Fig. 5.2). This result is consistent with the previously reported distribution of unrestricted dislocation glide distances $\rho(Z)$, which was found to decay exponentially (dashed gray curve in Fig. 5.2) [22]. Together these results depict the probabilistic process, governed by the distribution $\rho(Z)$, by which a deformation-induced dislocation may glide to a grain edge without meeting an obstacle.

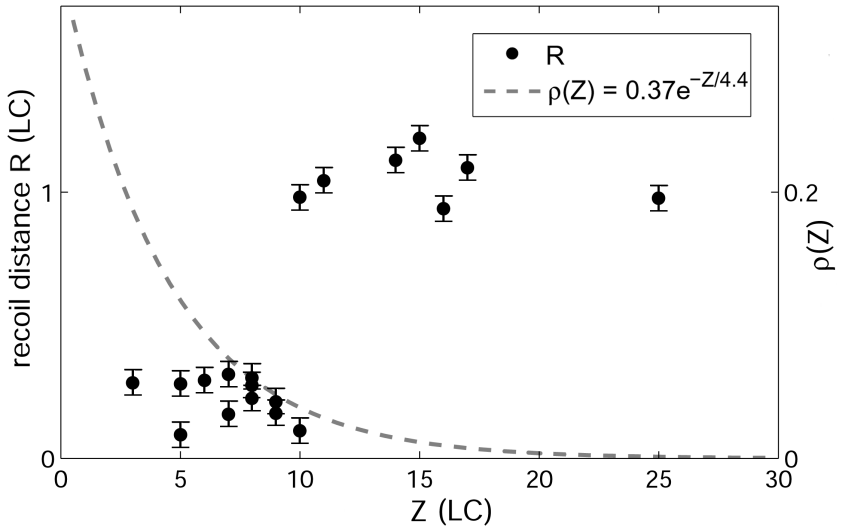

Figure 5.2: Recoil distance R as a function of glide distance Z to the nearest grain boundary. The error bars represent uncertainty in particle position. The distribution of unrestricted glide distances $\rho(Z)$ (dashed gray curve) is reprinted from [22].

5.5 Multi-defect mechanisms: long time relaxation experiments

Although unrestricted dislocation glide over long distances is improbable, multi-defect mechanisms such as dislocation reactions can allow dislocations to bypass glide-blocking obstacles and achieve long range motion [22]. However, since the energy required for such dislocation interactions is higher than that for simple dislocation glide [22], larger mechanical deformations are required to access such processes. Furthermore, mechanisms involving more than one defect are statistically less probable, and consequently may require longer waiting times.

In order to probe such multi-defect relaxation responses we conduct long time relaxation experiments where a perturbation is rapidly applied to a large

degenerate crystal grain. Before each experiment, one intruder particle is placed near the center of a large degenerate crystal grain containing more than 700 dimer particles. At time $t = 0$ s, the intruder particle is quickly dragged by 3 LC, arriving at its new lattice position at $t = 5$ s. The optical trap is turned off and the system is imaged for 10 hr, or until all the defects produced by the deformation leave the crystal grain. We record the number of defects by counting the lobes within the crystal grain that do not have six nearest neighbors. For example, a dislocation consisting of one five-fold and one seven-fold coordinated lobe is counted as two defects.

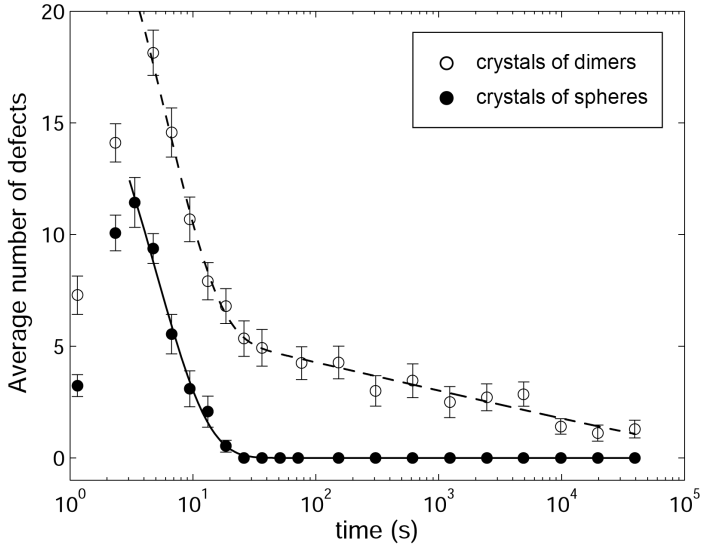

Figure 5.3: Average number of defects versus time for large (> 700 particles) degenerate crystals and crystals of spheres. Error bars represent the standard error of the mean. The solid line is the best fit exponential for the decay in the sphere data ($R^2 = 0.99$); the dashed line is the best fit sum of an exponential and a logarithmic decay for the dimer data ($R^2 = 0.99$).

To compare the relaxation response of degenerate crystals with a system where dislocations are known to glide without geometric restrictions, we repeat this experimental procedure on crystals of spheres. Here we prepare crystals

of PVP-stabilized 1 μm silica spheres suspended in an index-matching aqueous solution of DMSO, and we use 1 μm PVP-stabilized silica-coated polystyrene spheres as the intruder particles.

5.6 Glassy two-stage dislocation relaxation

The results from long time relaxation experiments on both degenerate crystals and crystals of spheres are shown in Fig. 5.3. In crystals of spheres, the decrease in the average number of defects $\overline{N_d}$ after the optical trap is turned off follows an exponential decay. The best fit exponential for this decay is $\overline{N_d} = 23e^{-t/\tau_S}$, where $\tau_S = 5 \pm 0.5$ s. In degenerate crystals, the initial decay of $\overline{N_d}$ is also characterized by an exponential decay, but a long tail is evident for later times. The best fit curve for this system combines both exponential and logarithmic decay terms: $\overline{N_d} = 25e^{-t/\tau_\beta} + 0.55\ln(1 + \frac{\tau_\alpha}{t})$, where $\tau_\beta = 6 \pm 1$ s and $\tau_\alpha = 2 \pm 1 \times 10^5$ s. These data depict strikingly different relaxation responses in the two systems. In crystals of spheres, dislocations leave the grain via one fast mechanism with characteristic timescale τ_S. In degenerate crystals, a similar initial fast response with timescale τ_β is followed by a much slower process with a timescale τ_α that is 5 orders of magnitude larger than τ_β.

Such two-stage relaxation is reminiscent of the slow relaxation dynamics common to many glassy systems [24, 9, 68]. Studies of colloidal glasses have revealed a caging effect where particles are confined by their neighbors [68] and are transported through the glass in two stages: an initial fast diffusion until encountering the caging neighbors, and a much slower cage-hopping process caused by multi-particle rearrangements that shift the cage structure. This two-

stage glassy relaxation is characterized by a long tail similar to that observed in defect relaxation for degenerate crystals (Fig. 5.3), suggesting that defect dynamics in dimer crystals is glassy.

Similarly to a particle in a glass, a dislocation in a degenerate crystal is caged. Initially, it moves via unrestricted glide at a rate characterized by τ_β, until it reaches particles with glide-blocking orientations. Here it remains caged until a second process characterized by the time scale τ_α can allow it to hop to a new region of unrestricted glide. This two stage relaxation process also explains the recoil measurements in Fig. 5.2. For small grains where dislocations only need to travel a short distance to reach the grain boundary, relaxation can occur through unrestricted glide alone. For larger grains, both stages of relaxation would be needed for the dislocations to exit the grain. However, this would require sufficiently long time scales for cage hopping processes to occur. Particles in the recoil experiments are only dragged 1 LC with a drag duration of $\tau_\beta < 20$ s $\ll \tau_\alpha$, which does not create enough defects to trap the system and allow enough time for multidefect relaxation processes, thus leading to the observed recoil in large grains.

5.7 Cage-hopping dislocation motion

Glassy relaxation can be directly observed in colloidal glasses by measuring the particle mean square displacement (MSD) versus time. Visualizing dislocation trajectories in local deformation experiments is complicated by the fact that all the defects originate near the intruder particle, rather than uniformly throughout the system as would occur during macroscopic deformations. To explore

such macroscopic deformations we run Non Equilibrium Molecular Dynamics (NEMD) simulations of dimer and sphere crystals under uniform shear. This approach probes defect dynamics in a non-equilibrium "steady state" rather than a perturbation. Furthermore, such simulations allow for comparison of dimer and sphere crystals in ideal conditions without grain boundaries or particle polydispersity. The simulations are conducted in a 2-D canonical ensemble wherein hard spheres (or dimer lobes) interact via the Weeks-Chandler-Andersen potential [69]. In reduced Lennard-Jones units, the system has size 50×50, sphere or lobe diameter $d = 1$, dimer lobe separation 1.07 maintained using holonomic constraints, and temperature of 1 maintained via a configurational thermostat [5]. Area fractions of 0.808 for dimers and 0.792 for spheres are chosen to have both systems at identical pressure, temperature, and chemical potential. A homogeneous shear field is applied to initially defect-free crystals using SLLOD equations of motion [19] and Lees-Edwards periodic boundary conditions [35]. The equations of motion are integrated using the Runge Kutta 4th order method with time step $\delta_t = 0.01$. Uniform shear is applied at a strain rate $\dot{\gamma} = 5 \times 10^{-5}$ per δt, a value small enough to drive dislocation motion at a speed independent of $\dot{\gamma}$. Dislocations are monitored after the number of defects has reached a steady value (Full simulation details provided in the supplementary materials section at the end of this chapter).

These simulations confirm strikingly different defect transport mechanisms in the two systems. Fig. 5.4a-b show plots of defect positions, where color corresponds to time. In crystals of spheres, dislocation pairs form and glide apart along straight paths nearly aligned with the shear direction (Fig. 5.4a). In stark contrast, defects in degenerate crystals follow crooked trajectories (Fig. 5.4b) and do not glide throughout the crystal, but rather are trapped within local

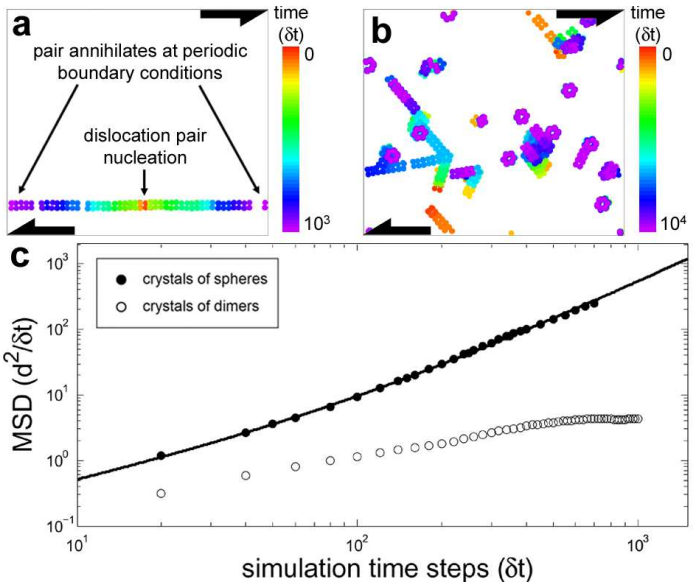

Figure 5.4: Defect trajectories in simulated crystals under shear (large arrows). (a) Dislocations in a crystal of spheres glide along straight paths in response to the applied shear. (b) Dislocations in a degenerate crystal follow crooked trajectories as they hop between caged configurations. (c) MSD of individual dislocations in crystals of spheres and degenerate crystals. Error bars are smaller than the markers. The solid curve is the best fit for $MSD = \langle \Delta r^2 \rangle = u^2 t^2 + 2Dt$.

cages. This caging is evident in the dislocation MSD, shown for both degenerate crystals and crystals of spheres in Fig. 5.4c. To calculate the dislocation MSD versus time, individual dislocations that can be resolved from other nearby defects are tracked between time steps. In crystals of spheres, dislocation motion is consistent with a biased 1D random walk (solid curve, Fig. 5.4c) with a diffusion constant $D = 2.3 \pm 0.2 \times 10^{-2}\ d^2/\delta t$, and drift speed $u = 2.23 \pm 0.05 \times 10^{-2}\ d/\delta t$. The dislocation MSD in degenerate crystals displays the characteristic plateau typical of particles in glassy systems.

5.8 Conclusions

In conclusion, we have uncovered a novel glassy system where the constituent particles are assembled into an ordered crystalline structure, but the dislocations within these crystals are caged and demonstrate slow, two-stage glassy relaxation. Such crystals also have a natural mechanism for encoding memory effects commonly observed in glasses, since moving dislocations reorient the dimer particles, encoding constraints for subsequent defect motion. While the transition into the glassy state typically occurs through an increase in particle density [38], here the glassy dislocation dynamics arise from constraints in an already dense crystal. Future studies of crystals of spheres doped with increasing concentrations of dimers will probe for this transition and determine whether it can be thought of more generically as an additional route to the jammed state. Finally, unlike typical jammed systems, increasing the dislocation density can reduce the amount of caging, suggesting that degenerate crystals may be self-healing materials.

5.9 Supplementary materials

5.9.1 Experimental techniques

Computing grain boundaries

To locate the grain boundaries in the experimental degenerate crystals, Voronoi analysis is used to compute the number of nearest neighbors for each lobe. Crys-

talline grains containing many ordered lobes with 6 nearest neighbors each are surrounded by a string-like collection of defect lobes having a number of nearest neighbors not equal to 6. The grain boundary defects for the small grain shown in Fig. 5.1c above are explicitly highlighted in Fig. 5.5.

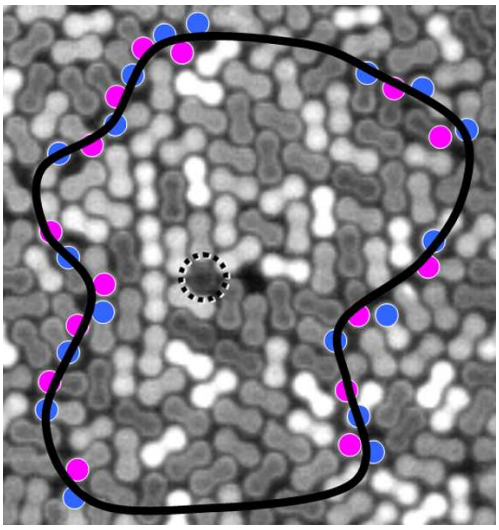

Figure 5.5: The grain boundary defects are highlighted around the small grain also shown in Fig. 5.1c above. Pink and blue dots represent lobes having a number of nearest neighbors equal to 5 or 7, respectively. The dotted circle marks the spherical intruder particle.

5.9.2 Molecular dynamics simulations

We have performed 2-D Number Volume Temperature (NVT) Non Equilibrium Molecular Dynamics (NEMD) simulations of both pure sphere and pure dimer crystals. The separation between lobes in the dimer particles is set to be 1.07 times the diameter of the spherical lobes, in approximation of the experimental system. The hard spheres (or dimer lobes) interact with each other via the Weeks-Chandler-Andersen potential [69] given by

$$U(r) = \begin{cases} 4(r^{-12} - r^{-6}) + 1 & r \leq r_m = 2^{\frac{1}{6}} \\ 0 & r > r_m \end{cases}$$

where r is the interparticle distance and r_m is the minimum of the potential. In this and all the following equations, all the properties are expressed in terms of reduced Lennard-Jones units.

The crystals are initially defect-free, with every sphere (or dimer lobe) located exactly on a triangular lattice site. Dimer crystals are in a degenerate crystalline state such that the dimers are oriented randomly along any of the three lattice directions [73]. The simulations of both dimer and sphere crystals are performed at equivalent area fractions, as defined below, at reduced temperatures $T^* = 1.0$ (sufficiently below their melting temperatures) with a time step $\delta t = 10^{-2}$. To preserve the heterogeneities in the system we use a novel configurational thermostat which does not constrain the flow profile [5].

Area fraction

In order to fairly compare crystals of dimers with crystals of spheres at equivalent area fractions, we first perform direct interfacial NVT simulations of compound systems of sphere and dimer lattices. On equilibration, once both lattices share the same chemical potential, pressure and temperature, these simulations provide estimates of the coexistence area fractions for the two species. Then, for our NEMD simulations, we have used one set of these equivalent area fractions: 0.808 for dimers and 0.792 for spheres, both well above the melting densities.

Shear rate

Both the crystals of pure spheres and the crystals of pure dimers are sheared at a shear rate $\dot{\gamma} = 5 \times 10^{-5}$. In order to choose the value of $\dot{\gamma}$, several factors were considered. First, in order to study dislocation motion in the crystalline regime, the shear rate must not be high enough to destroy the crystalline order. When shear is applied to the initially defect-free system, some defects are created, thereby reducing the crystalline order. However, if the shear rate is chosen to be low enough, then after some characteristic 'stabilization time' – about 10^6 time steps in our simulations – the number of defects in the system fluctuates around a steady value and the crystalline order does not decrease further.

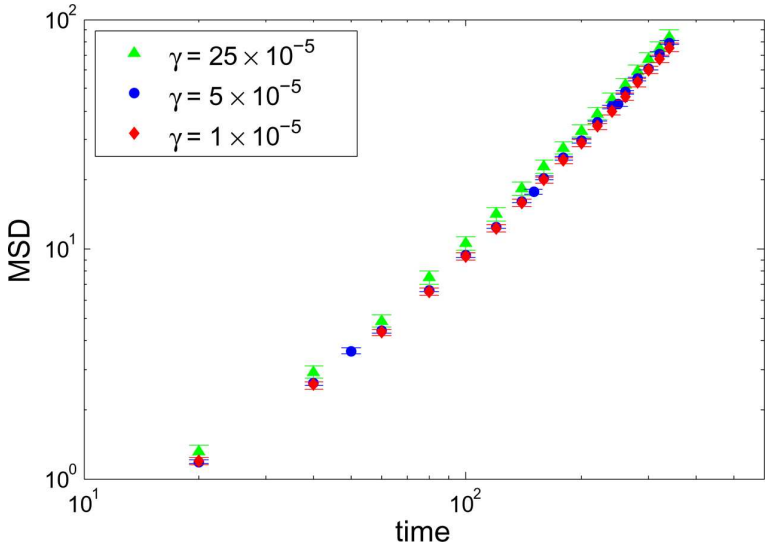

Figure 5.6: Dislocation mean squared displacement in crystals of spheres under uniform shear at three different shear rates $\dot{\gamma}$. Error bars represent the standard error of the mean.

A second important consideration is the effect of shear rate on dislocation glide speed in crystals of spheres. To ensure that we are studying dislocation motion in a 'quasi-static' regime where dislocation motion is independent of the applied shear rate, we have also tracked dislocation motion in crystals sheared

at two additional shear rates: $\dot{\gamma} = 25 \times 10^{-5}$ and $\dot{\gamma} = 1 \times 10^{-5}$. We compare the dislocation mean squared displacement (MSD) for the 3 shear rates and find that while dislocation motion is slightly faster for $\dot{\gamma} = 25 \times 10^{-5}$, the lower two shear rates are indistinguishable within the error bars (Fig. 5.6). This indicates that at $\dot{\gamma} = 5 \times 10^{-5}$, we are in the regime where dislocation motion is independent of $\dot{\gamma}$.

This shear rate independence can be understood by considering dislocation motion in crystals of spheres, where we find that long periods of dislocation inactivity are punctuated by brief glide events. In such glide events, two dislocations form and glide apart along the lattice axis aligned with the shear direction. Between the glide events, shear stress caused by the applied shear rate $\dot{\gamma}$ slowly builds up until enough stress is present to separate a pair of dislocations. Once the dislocations start to separate, they quickly glide apart and annihilate after traversing the periodic boundary conditions. Changing the shear rate $\dot{\gamma}$ only affects the average waiting time between glide events, not the speed of dislocation motion during the events. To quantify how small the applied shear rate is, we compare the time $\tau_{\dot{\gamma}}$ for the applied shear to cause a shear displacement of 1 LC to the time τ_d for a dislocation pair to separate across the simulation box, causing a shear displacement of 1 LC. For $\dot{\gamma} = 5 \times 10^{-5}$, $\tau_{\dot{\gamma}} = 4 \times 10^4$, while $\tau_d = 990 \pm 16$ (mean $\pm$ standard error of the mean). Thus, $\tau_{\dot{\gamma}}$ is about 40 times larger than τ_d.

Calculating dislocation mean squared displacement

To calculate the dislocation MSD, we have tracked the positions of individual dislocations consisting of paired 5-fold and 7-fold coordinated lobes (or

spheres). In both degenerate crystals of dimers and crystals of spheres, our analysis is restricted to dislocations that can be distinctly resolved from any other nearby defects. In dimer crystals, this requirement limits our analysis to dislocation motion before or after – but not during – a dislocation reaction.

In order to correct for affine displacements imposed by the applied external shear $\dot{\gamma}$, relative dislocation x-displacements $\Delta x(\tau)$ were shifted by the accumulated strain displacement $\delta x(\tau)$ corresponding to the relative y-displacement $\Delta y(\tau)$. The shear-corrected dislocation displacement $\Delta x_c(\tau)$ after a time interval τ is given by:

$$\begin{aligned} \Delta x_c(\tau) &= \Delta x(\tau) - \delta x(\tau) \\ &= \Delta x(\tau) - \dot{\gamma}\tau\Delta y(\tau) \end{aligned}$$

Typical values of $\delta x(\tau)$ for time intervals τ measured in calculating the dislocation MSD were approximately 3 orders of magnitude smaller than $\Delta x_c(\tau)$.

CHAPTER 6

TRANSITION INTO THE GLASSY DISLOCATION STATE

6.1 Abstract

Recent studies of relaxation in crystals of colloidal dimer particles have demonstrated that the dislocation dynamics in such crystals is reminiscent of glassy systems. In particular, the decay of the number of defects following a mechanical perturbation applied using an optically trapped particle displays two-stage relaxation including a fast process with timescale τ_β and a much slower process characterized by τ_α. Furthermore, the motion of dislocations in dimer crystals is caged, resulting in a plateau region in the dislocation mean squared displacement. The observed glassy dislocation phenomena in dimer crystals arise as a result of restrictions on dislocation glide caused by interlocking dimers. In the current study, we investigate the transition from the usual dislocation dynamics observed in crystals of spheres to the glassy dynamics in crystals of dimers. In order to enter the glassy state from the usual state, crystals of spheres are doped with increasing concentrations of dimers ϕ_d. The glassy restrictions on dislocation motion are monitored as a function of ϕ_d, and the relaxation response of perturbed crystals is also studied.

6.2 Introduction

Glassy dynamics are typically attributed to disordered systems such as jammed granular packs [31, 6] or molecular or colloidal glasses [67, 68, 60, 15]. However,

recent studies of defects within 2-D crystals of colloidal dimer particles have revealed that glassy relaxation can occur within an ordered, crystalline system [21]. The glassy behavior in this system arises as a result of geometric restrictions to dislocation glide caused by interlocking dimer particles. In the degenerate crystal (DC) phase formed by colloidal dimer monolayers at high area fractions, each dimer lobe occupies a triangular lattice site while the dimer bonds are oriented randomly along any of the three lattice directions. Dislocations in a DC are caged by dimers in certain glide-blocking orientations; dislocation motion beyond such particles occurs through multidefect mechanisms that allow the defects to hop between cages [21]. This slow cage-hopping is reminiscent of the motion of particles within a colloidal glass [68] and invites the question of how this glassy state is approached from the usual state of free dislocation motion in 2-D crystals of spheres.

In the current study, we investigate the geometric restrictions to dislocation glide in mixed crystals composed of both spheres and dimers. We find that the peak dislocation cage size decreases smoothly from infinity for crystals of spheres where dislocation glide is unrestricted down to several lattice constants (LC) as more dimers are added. The transition into glassy dislocation dynamics is still under experimental investigation at the time of writing this thesis.

6.3 Experimental system

The experimental system has been described in detail elsewhere [21]. Briefly, sterically-stabilized fluorescent silica dimer shells with lobe diameter $D \approx 1.3$ μm and lobe separation $l \approx 1.4$ μm are suspended in an index-matching

aqueous solution of dimethylsulfoxide. The dimer shell particle synthesis protocol is provided in [34] and in Appendix A. Also included in the suspension are 1.3 μm diameter silica spheres (Sekisui Micropearl Spacers, Dana Enterprises International, CA). The suspension of dimers and spheres is confined in a wedge-shaped cell constructed from two bonded glass coverslips, as described in Appendix B. The particles are viewed in the 'monolayer' region of the cell where the gap between the two coverslips only accommodates a single layer of particles lying flat. The density mismatch ($\sim$ 0.5 g/mL) between the shells and the fluid is exploited to sediment the particles into the monolayer region, and to set the area fraction to ~ 0.8, where the dimer shells and the spherical particles assemble into a mixed crystal.

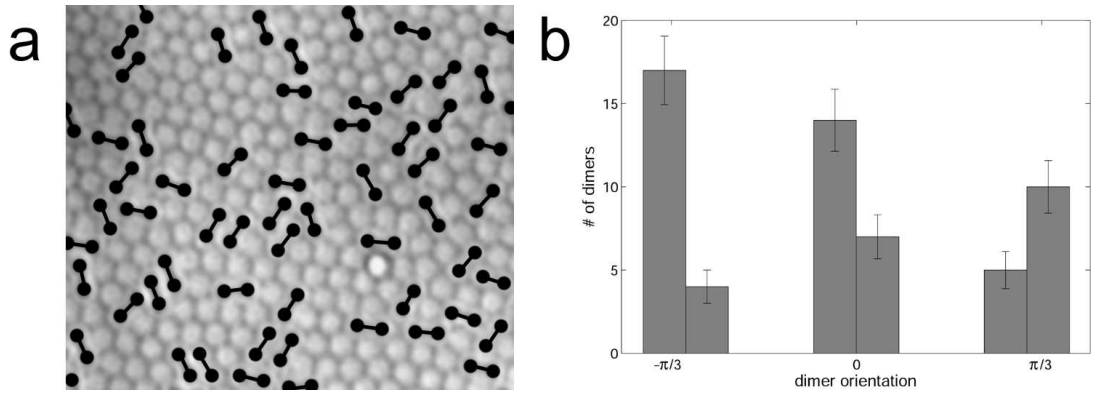

Figure 6.1: (a) Optical microscope image of a mixed sphere and dimer crystal with $\phi_d = 0.4$. Dumbells are overlaid on top of the dimers for clarity. The bright white sphere is a PS intruder particle. (b) Distribution of dimer orientations within the grain. Error bars are derived from counting statistics.

To probe their defect relaxation dynamics, the mixed crystals are perturbed using an optically manipulated 1.3 μm diameter spherical particle that is composed of silica-coated polystyrene (PS) and is also sterically stabilized [21]. The index mismatch between the spherical intruder particle and the suspending fluid allows the optical trap to exert a force on the sphere with negligible ef-

fects on the silica dimer shells and spheres. The PS spheres are first used to push dimer particles into an initially pure sphere crystal within the monolayer region of the wedge cell until the desired dimer concentration ϕ_d is reached. Once a grain is assembled, one PS sphere is placed near the center of the grain and then may be moved within the grain to cause perturbations.

An example of one mixed crystal grain prepared using a PS sphere to add dimer particles is shown in Fig. 6.1a. While such mixed crystal grains are not self-assembled, the dimers are nevertheless oriented with approximately equal probability among the three lattice directions, as can be seen in the distribution of dimer orientations shown in Fig. 6.1b.

6.4 Numerically generated mixed crystals

The distribution of dislocation cage sizes can be computed within any mixed crystal grain such as the one pictured in Fig. 6.1 by counting how far a dislocation with any of the three possible Burgers vectors could glide from each starting lattice position. While in principle it would be possible to collect sufficient statistics on such cage sizes by experimentally forming numerous large grains at each dimer concentration ϕ_d, this is not feasible within a reasonable time frame. Instead, we simulate ensembles of large triangular crystal grains containing 10^4 to 1.6×10^5 lattice sites for each value of ϕ_d.

Each simulated mixed crystal is initialized as a perfect triangular lattice of unbonded sites with periodic boundary conditions. In order to achieve the desired dimer concentration ϕ_d, bonds are added at random between neighboring lattice sites, creating dimers on the lattice. An example of such a numerically

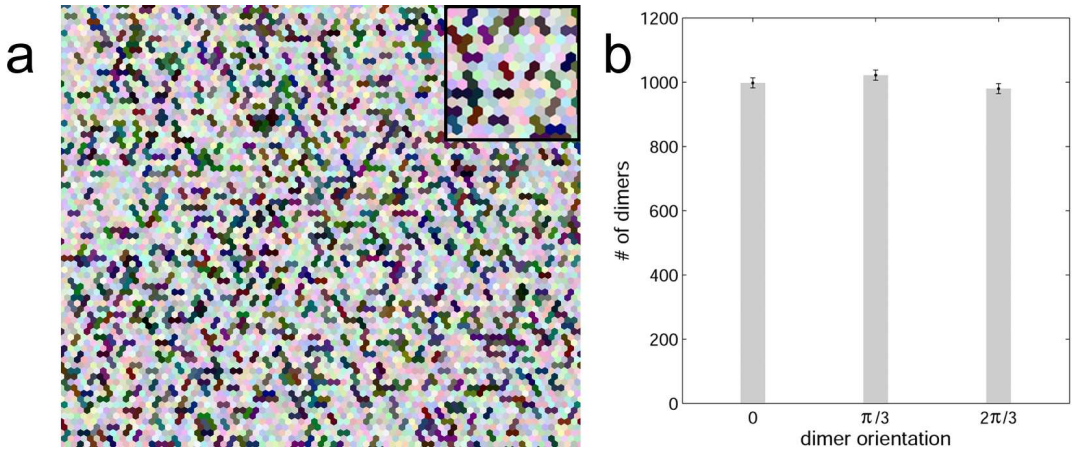

Figure 6.2: Example of a numerically calculated mixed crystal with dimer concentration $\phi_d = 0.3$. (a) The lattice sites that are dimer bonded are colored in matching darker hues, while the sphere lattice sites are uniquely colored lighter hues. Inset: Zoomed in view illustrating the color-coding for dimers versus spheres. (b) The distribution of dimer orientations for this mixed crystal demonstrates that the three lattice directions are equally weighted. Error bars are derived from counting statistics.

calculated mixed crystal with $\phi_d = 0.3$ is shown in Fig. 6.2a (for clarity, only a subset of the 10^4 lattice sites are shown). The distribution of dimer orientations, shown in Fig. 6.2b, demonstrates that the 3 lattice directions are equally populated.

The distribution of dislocation cage sizes z, taken over an ensemble of large mixed crystals for each dimer concentration, is plotted for $\phi_d = \{0.1, 0.2, ...1.0\}$ in Fig. 6.3. At least 10^5 individual cage sizes are included in the distributions for each dimer concentration, and the error bars due to counting statistics are comparable to the marker size. For clarity, the inset of Fig. 6.3 shows the same distributions on a semilog plot. We find that a functional form of $\rho(z) = Az\ \mathrm{e}^{-z/z_*}$ is consistent with the cage size distributions observed for every dimer concentration. Although we note that the fit is not perfect for small cage sizes z, this

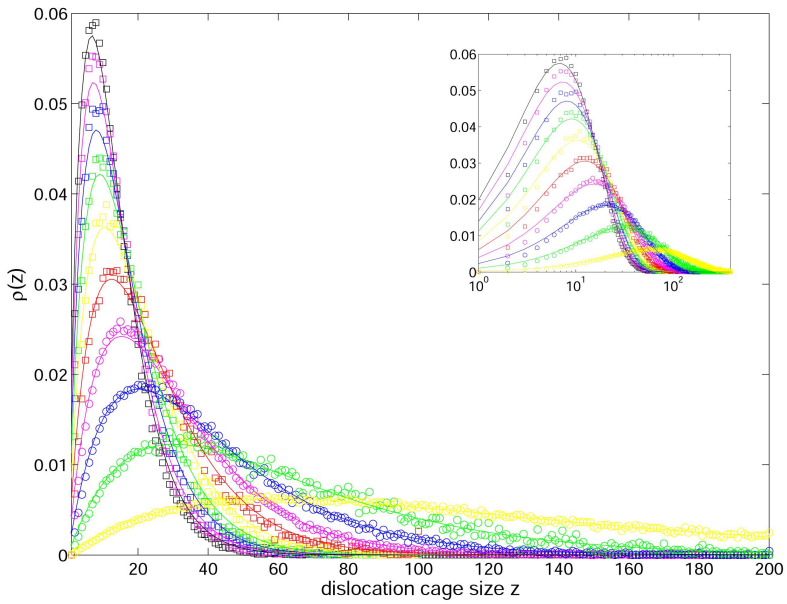

Figure 6.3: The distribution of cage sizes for each dimer concentration. Marker key: black squares: $\phi_d = 1.0$, purple squares: 0.9, blue squares: 0.8, green squares: 0.7, yellow squares: 0.6, red squares: 0.5, purple circles: 0.4, blue circles: 0.3, green circles: 0.2, yellow circles: 0.1. The curves are fits as described in the text. The distribution is also shown in a semilog plot as the inset.

functional form conveniently predicts the peak cage size z_* for each dimer concentration.

We find that the peak cage size z_* taken from the fit for each distribution decreases smoothly with ϕ_d, as shown in Fig. 6.4. The line is the best fit power law, $z_* = Z_0 \phi_d^{-\alpha}$, with $Z_0 = 6.3 \pm 0.1$ LC and $\alpha = 0.98 \pm 0.02$. This is consistent with the idea that if the concentration of dimers is doubled, the distance between dimers is halved. We note that the value of the peak cage size for a crystal of pure dimers is consistent with the previously reported average maximum glide distance of 6.2 LC.

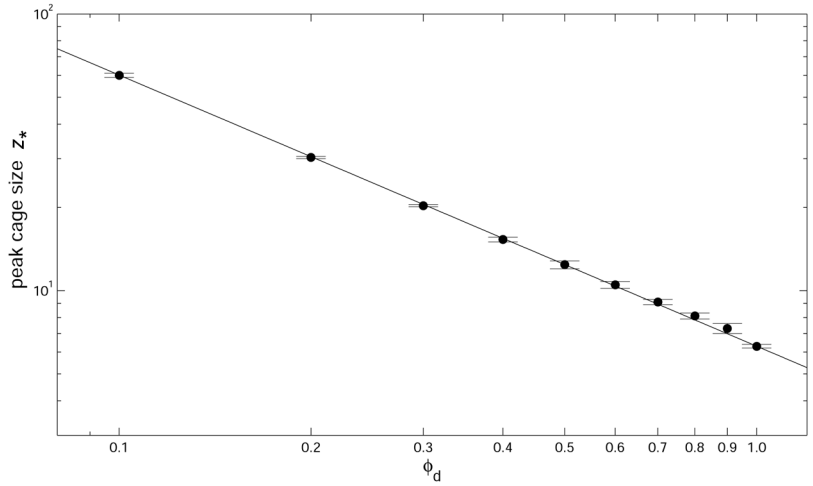

Figure 6.4: The peak cage size z_* as a function of dimer concentration ϕ_d. The line is the best fit power law, as described in the text.

6.5 Conclusions

While experimental studies of relaxation of mixed crystals are still underway, the preliminary results from the simulations suggest that the transition into restricted dislocation motion is characterized by smoothly decreasing dislocation cage sizes. Interestingly, the functional form of the cage size distribution $\rho(z)$ is universal to every dimer concentration we have studied, from 0.1 to 1.0. The peak cage sizes decrease as a power law very close to $1/\phi_d$, an indication that the peak caging distance scales as the average dimer separation. Experimental investigations of dislocation motion will probe for a possible similar power law scaling of dislocation waiting times as a function of the dimer concentration.

CHAPTER 7

DIMER DREAMS FOR THE FUTURE AND A DOSE OF REALITY

7.1 Abstract

The studies described in Chapters 2 to 6 of this thesis have uncovered such unexpected results that further investigations of colloidal dimers seem desirable. The effect of dimer bonds on the dislocation dynamics within 2-D crystals suggests that such bonds may also lead to other pronounced differences between suspensions of dimers and of spheres. In this chapter, I briefly describe some of the many interesting directions for possible future studies of colloidal dimers. However, I also outline some of the setbacks that currently limit our ability to pursue such studies.

7.2 Dimer dreams

Perhaps the most obvious direction for future studies is to investigate dislocations in 3-D crystals of dimer particles. In fact, the initial plan for my thesis research was to study assemblies of dimers in 3-D. However, due to some technical difficulties outlined below in the "Reality" section of this chapter, such studies are not feasible without significant particle synthesis advancements. If such difficulties could be overcome, the dream 3-D dimer project would focus on dislocation motion in a slowly sheared slab of dimer degenerate crystal. While macroscopic shear is difficult to achieve in 2-D experiments, it is possible to shear a 3-D crystal of dimers using the shear cells commonly used in the

Cohen lab to study systems of spherical colloidal particles. Such a study would elucidate whether dislocations in 3-D dimer crystals encounter similar restrictions to glide caused by particles that cross slip planes in certain shear-blocking directions. One possible implication of such restrictions in 3-D might be that collective dislocation motion similar to the dislocation avalanches observed in highly confined nanowires [12] would play an important role in macroscopic shear deformations. It would be especially interesting to investigate how the collective dislocation interactions vary as the sample height is controlled.

It would also be interesting to study the effect of dimer bonds on the colloidal glass transition. As outlined in the introduction to this thesis (Chapter 1), much groundwork has been laid for understanding the glass transition on the particle scale for suspensions of spherical particles. However, many molecular glasses such as polymer glasses are composed of anisotropic constituents. In such systems, the glassy behavior is often characterized by the reorientations of the constituents. While rotations of spherical colloids cannot be observed, the reorientation of colloidal dimers within a dense disordered dimer suspension could be monitored - this would certainly be feasible in 2-D studies. Clearly in dense suspensions of dimers, particle rotations are limited by the orientations of nearest neighbor particles. One would expect that the orientational freedom of individual dimers within such a suspension would decrease dramatically as the particle area fraction is increased. In particular, it would be interesting to check whether the number of particles that must reorient in order to allow a given particle to rotate diverges as a glass transition area fraction is approached.

In the spirit of the previous idea, it would also be interesting to include a small number of dimer particles in a 3-D colloidal glass composed primarily

of spherical particles. These few dimers could be used as orientational thermostats; their rotational fluctuations could be monitored as a function of, say, confinement of a disordered glassy suspension. By comparing orientational fluctuations with translational fluctuations it would be possible to see which modes are suppressed first as the system approaches the glass transition.

7.3 Reality

We have been very lucky to collaborate with the Liddell group at Cornell, who were the first to develop successful, repeatable particle synthesis techniques for making porous dimer shells. In fact, we know of at least two other prominent colloid groups who have also been racing to get results with colloidal dimers. Part of our success in being the first to publish on this exciting new system is due to the particle synthesis techniques of the Liddell lab. However, no system is perfect, and these dimer colloids have their fair share of issues which have hindered experimental progress at several points along the way.

The first challenge is that the particle synthesis procedure produces numerous mutant particles, some examples of which are depicted in Fig. 7.1. These mutants suppress crystallization and significantly limit the size of grains that can self-assemble. There are also many larger non-dimer-shaped aggregates which complicate crystallization. By using a wedge-shaped ramp cell geometry, we filter out the vast majority of larger aggregates that cannot fit into the monolayer region where the 2-D experiments are recorded. However, there are still many (about 15%) mutant particles that are small enough to pack alongside the dimers in the monolayer region and interfere with crystal formation.

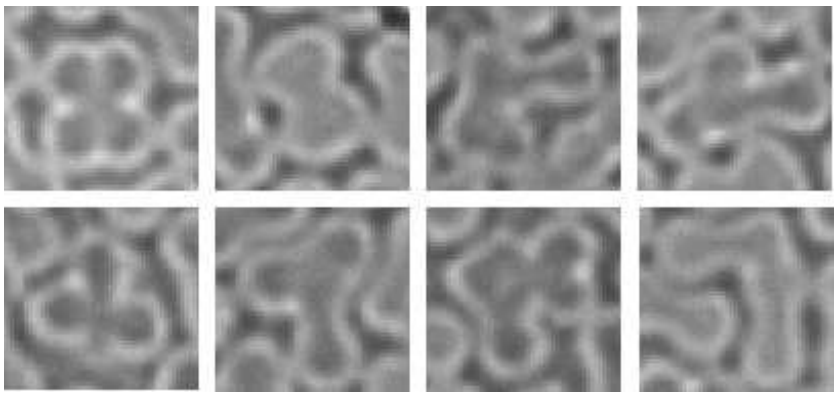

Figure 7.1: Examples of typical nearly dimer-sized mutant particles commonly found in the monolayer region of the wedge-shaped ramp cells used for experiments.

Our method for overcoming the obstacle of the remaining nearly dimer-sized mutants was to spend about 30 hours over the course of 1.5 weeks to prepare each crystalline grain. Each grain was prepared by using an optically trapped polystyrene sphere as a bulldozer to push mutants out of a region and then waiting for the region to crystallize before starting each experiment. This technique is painstaking, and unfortunately the time required for such mutant removal severely limits the number of experimental grains that can be studied in a given time period. However, with a bit of determination, it is still feasible to prepare grains containing about 700 particles for 2-D studies. This method would not be feasible for 3-D studies, where a region containing $\sim 10^6$ particles would be needed to study dynamics within a grain with a characteristic length-scale of 100 LC (still a small grain size by 2-D standards). Furthermore, using the optical trap in a dense 3-D suspension of particles is much more challenging due to laser scattering off of any imperfectly index-matched particles and may not be possible for a 3-D crystal of dimers.

The second main challenge involved in collecting significant statistics from

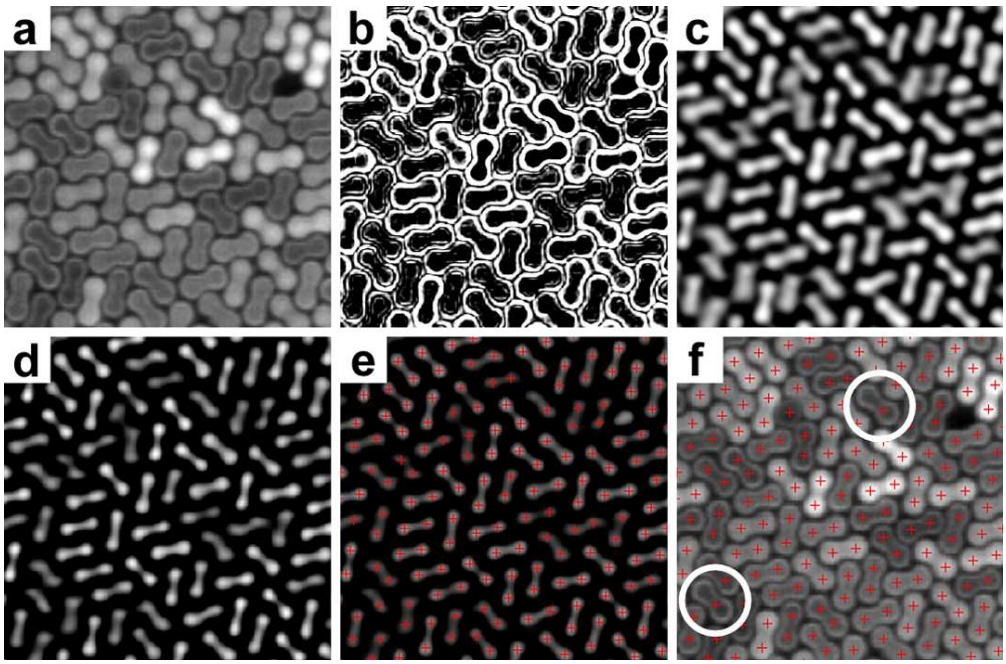

Figure 7.2: The process of semi-automatic lobe identification. (a) A typical confocal image, demonstrating the variety of particle appearances. (b) The same image a brightness/contrast adjustment and an edge-finding algorithm defined in ImageJ. (c) The same image after inversion and a bandpass filter applied using ImageJ. (d) The same image after an additional bandpass filter applied using Matlab. (e) The same image shown in (d) with the located lobe positions overlaid as red plus symbols. (e) The lobe positions overlaid on the original image. Note that the vacancy does not get counted as a lobe. Also note the two misidentified dimers marked with circles.

images of these particles is that lobe identification cannot be completely automated. Due to uneven fluorescent dye concentrations during particle synthesis, the brightness and appearance varies significantly from one particle to the next (Fig. 7.2a), a fact that seriously complicates any typical automatic image processing scheme. After many different attempts to automatically locate the dimer lobe positions, we found that the best results occur when a sequence of image brightness/contrast adjustments, edge-finding algorithms, and band-pass Fourier filters are used to transform such images into something more closely

approximating bright gaussian blobs on a dark background (Fig. 7.2b-d). Then standard feature-finding algorithms [11] are used on these pre-processed images to find lobe positions (Fig. 7.2e,f). Any false lobes corresponding to locations that are darker than a threshold value in the original image are automatically omitted, so that vacancies such as the one shown in Fig. 7.2 are not counted as lobes. This technique commonly determines the positions of dimer lobes with $\sim 90\%$ accuracy. The remaining 10% are corrected manually using a custom interactive graphical user interface (GUI) written using Matlab. While 10% may at first seem like a small correction, in practice a single experiment consisting of about 300 images typically takes about 5-7 hours to correct using the GUI, which is nevertheless about an order of magnitude faster than previous techniques. However, this semi-automatic lobe finding, which is crucial for determining the positions of defects within a crystal, limits the statistics that can be collected in a reasonable amount of time. I also emphasize that this issue would be even more challenging for trying to process 3-D image stacks of dimer crystals or glasses.

The third and perhaps most fundamental technical challenge is that the dimer particles are synthesized in small batches. Within each batch, the dimer size and shape is roughly constant, but between batches, these parameters vary and cannot be exactly controlled. Together these issues amount to the fact that only a very small ($\sim 200\ \mu L$ at 60% volume fraction) batch is available for experimentation. Particle separation techniques such as using density gradients to distinguish bands of abnormally large particles from pure dimers are not feasible with such small total sample sizes. Our wedge-shaped cells for 2-D studies have once again come to the rescue on this issue, since each cell requires only a tiny amount of sample (approximately $10\ \mu L$ at 5% volume fraction). In or-

der to allow for 3-D studies, much larger batch sizes would be needed so that proper particle filtering techniques could be used to remove the mutants and large clusters.

Given the technical challenges that have arisen in our studies of the colloidal dimers, it is perhaps surprising that such interesting results about differences between dimer crystals and sphere crystals have nevertheless emerged. Despite the challenges, I believe that the system of dimer particles is rich with new phenomena while still fitting within the larger infrastructure of what is already understood about suspensions of spheres. This combination makes further studies quite appealing, but clearly much work needs to be done to address the technical issues before further progress can be made in understanding the physics of this interesting new system.

CHAPTER 8

EPITAXIAL CRYSTAL GROWTH: SPHERICAL PARTICLES

8.1 Introduction

In addition to my main focus on colloidal crystals of dimer particles, I have also significantly contributed to a study on thin film epitaxial growth of colloidal sphere crystals.[1] In epitaxial thin film growth, a crystal forms on the surface of an existing crystalline substrate. While epitaxial growth has been extensively studied in atomic systems [77], little is known about whether the existing descriptions can also be applied to the epitaxial growth of colloidal or nanoparticle crystals. In this chapter, I will describe my contributions to a study led by Rajesh Ganapathy on crystals of spherical colloidal particles epitaxially grown on templated glass surfaces. These experiments explore the Ehrlich-Schwoebel barrier [16, 59] which plays a crucial role in determining the morphology of the growing crystals. Interestingly, we find that in the colloidal crystals, this barrier arises due to diffusive effects rather than being purely energetic in origin.

8.2 Experimental system

Briefly, our system consists of charge-stabilized 1 μm diameter silica or polystyrene colloidal spheres suspended in an aqueous solution. An effective interparticle attraction is introduced by adding polymers with a radius of gyration of $\sim$50 nm to the solution. These 'depletant polymers' produce a very

[1] Much of the information in this chapter is taken from our manuscript [20].

short-ranged ($\sim$5% of the particle diameter) attraction induced by the depletion effect.[2] In each experiment, particles sediment through the solution onto a solid substrate. Substrates with crystalline texture must be used to emulate epitaxial growth. In order to achieve this for our colloidal crystals of spherical particles, we lithographically pattern a periodic array of particle-sized holes into a polymethylmethacrylate layer spin-coated on a conducting glass coverslip.[3] Sedimentation of the colloidal particles in pure water onto this patterned coverslip causes a monolayer of particles to form in the holes. These particles are permanently bonded to the coverslip by applying a DC electric field, which drives the charged particles deep into the holes until the particles bind to the exposed conducting coverslip at the bottom of the holes. This monolayer of particles serves as the crystalline substrate on which epitaxial crystallization is studied.

For each epitaxy experiment, a mixture of particles and depletant polymers is sedimented onto the crystalline substrate at a set flux F that is determined by the volume fraction of the sedimenting suspension. When the particles land on the substrate, they undergo thermally-activated hops from one interstitial well to the next along the surface and coalesce into islands like the one depicted in blue in Fig. 8.1. Both the formation of islands and the dynamics of additional particles diffusing on top of the islands are described in our manuscript [20]. However, since my role in the latter topic was more significant, I will restrict the present discussion to the particles on top of already-formed islands.

[2]The depletion effect is described in Appendix C.
[3]A brief overview of this technique is provided in Appendix D.

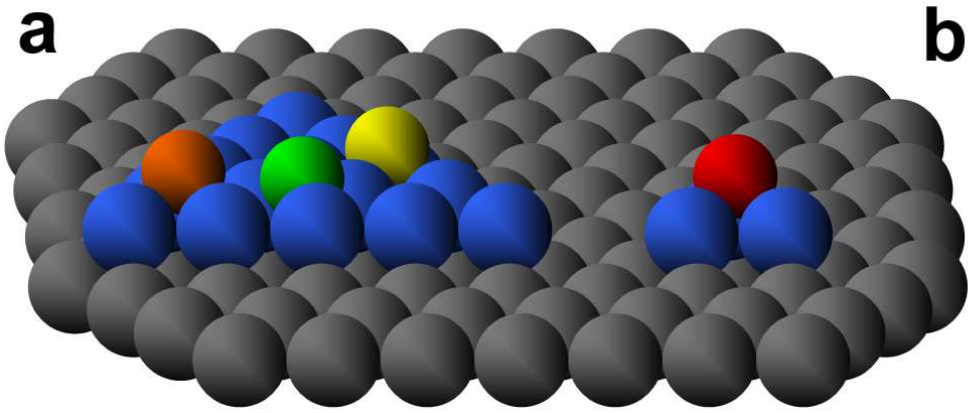

Figure 8.1: Schematic of islands formed on the crystalline substrate. The permanently bonded monolayer is shown in gray, while the particles making up the epitaxially grown islands are colored blue. (a) On top of this 15 particle island, there are 3 additional particles shown in 3 different types of island sites (details in text): $p = 0$ (green), $p = 1$ (yellow), and $p = 2$ (orange). (b) The single particle in red on top of this 3 particle island is in a site with $p = 3$, since all 3 exit pathways descend off of the island.

8.3 Experimental results

In atomic epitaxial growth, the Ehrlich-Schwoebel barrier (ESB) is the observed barrier that prevents particles diffusing on top of islands from descending off of the edge of the island. If the ESB is strong, then additional atoms (or particles) that land on top of existing islands will be trapped on the second layer and will ultimately contribute to pyramid-like growth in 'mounds' such as those pictured in [40, 61]. Such mounds are undesirable in many technological processes where thin films are used, whether the films consist of atoms as in [40] or quantum dots as in [61]. Understanding the ESB would allow for improved design and manipulation of thin film growth.

In atomic systems, it is thought that the primary cause of the ESB is related

to the energetic barrier present at a step edge. A rough schematic of the energy landscape for an atom on top of an island is provided in Fig. 8.2a. Each of the barriers shown on the left half of the schematic represents the energetic cost for an atom to hop from one site to the next while remaining on the island. This energetic cost can be thought of as the energy required to break a bond with one of the three atoms underneath the atom when it is in any site. When an atom hops from a site on the island to a site off the island, the energetic cost increases because the lengthscale of the interatomic attraction is large enough to allow for second nearest neighbor interactions.

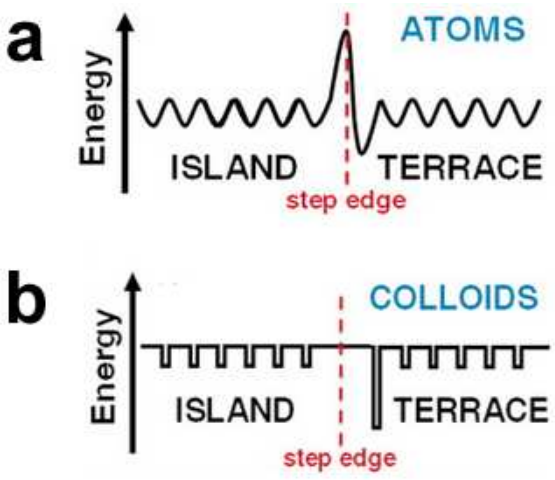

Figure 8.2: Schematic of the energy landscape near a the edge of an island for atoms (a) and for our colloidal system (b). The edge of the island is marked with a red dotted line in each schematic.

In our colloidal system, the interparticle attraction is very short-ranged, so that the energy landscape for a colloidal particle atop an island looks more like the schematic shown in Fig. 8.2b. In particular, we note that there is no additional energetic barrier present at the island edge. Quite surprisingly, we nevertheless observe an ESB-like barrier that prevents particles from descending off of islands.

We characterize this observed barrier by considering the average residence time in a given site on top of an island. There are four distinct kinds of sites where particles on top of an island can reside, as depicted in Fig. 8.1. These four types are distinguished by the number of exit pathways p that take the particle off of the island from that site. For example, the orange particle in Fig. 8.1a is located on a site at the corner of the island. Thus, 2 of its 3 exit pathways from that site would take it off of the island, and $p = 2$. Presumably if there is an ESB preventing particles from descending along a pathway off of the island, then one would expect that the average residence time in a given site would increase with p.

To investigate this expected dependence on p, we use a holographic optical tweezer system (Arryx, Inc) [14] to manipulate individual particles and assemble a triangular island consisting of 15 particles. We then use the tweezers to place a single particle on the island, and finally turn off the tweezers and monitor the position of the particle as it moves from site to site. The plot of mean residence times τ shown in Fig. 8.3 is the result of 100 independent experiments of this variety. Clearly particles hopping from site to site atop an island spend more time in the corner and edge sites than on the interior sites, indicating that there is in fact some kind of barrier preventing particles from descending off of the island edge. Specifically, the longest mean residence time τ is observed in the corner sites ($p = 2$), while τ is lower for the edge sites ($p = 1$), and lowest for the interior sites ($p = 0$). This data is also summarized in Fig. 8.7, where the mean residence time τ is plotted versus p directly.

As mentioned above, going by energetic considerations alone, we would not have expected to observe a barrier. In the colloid system, even after the particle

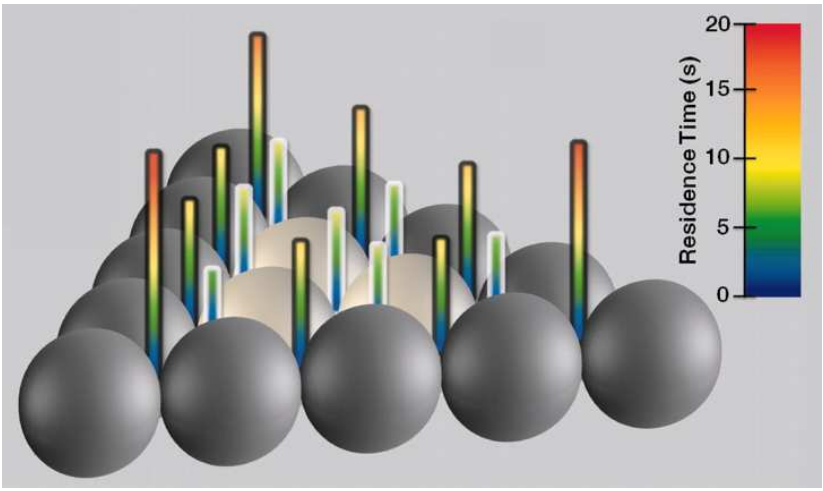

Figure 8.3: Mean residence times spent in each site atop the 15 particle island shown in gray. Colorbars indicate mean residence time. The values of residence time represent averages over 100 independent experiments. The mean residence time is largest for the corner sites ($p = 2$), lower for the edge sites ($p = 1$), and lowest for the interior sites ($p = 0$).

acquires thermal energy to break a depletion bond with an underlying particle, it must move to the next site by diffusing along the energetically flat valley formed by the underlying particles. Depending on the strength of the depletion interaction, there are two limiting regimes. In the weak-interaction limit, the bond breaking time is very short and most of the residence time is spent with the particle diffusing from one site to another. The distance traveled by a particle diffusing off of an island edge on a triangular lattice is 2.8 times the distance between sites on the island. For a diffusive process, the mean-squared displacement increases linearly with time and the interstitial residence time in this limit would be expected to scale as the square of the path length. Specifically the the mean residence time τ for a site with all off-island pathways ($p = 3$) would be 2.8^2 longer than τ for a site with all on-island pathways ($p = 0$). In the strong-interaction limit, the bond breaking time is very long compared to the characteristic diffusion time for a particle diffusing on a flat energy landscape

over the distance between interstitials. One might think that this would even out the playing field for moves on the island versus off the island. However, since the particle must still successfully diffuse from one site to another, the particle could make many returns to the original interstitial site before making it all the way to the next site. Each time it returns to the original site, it would re-form its bonds and then have to wait another bonding time before attempting the diffusive walk to the next site again. Since the number of times a 1-D random walker returns to the origin increases linearly with the length of the path that it is diffusing on [54], in the strong interaction regime the particle would be expected to return to the original site 2.8 times more often for particles attempting to descend steps. This would cause the mean residence time τ for a site with only off-edge moves to be 2.8 times larger than that for an interior site. For more complicated sites where some pathways are on-island while others are off-island, it is not trivial to predict how the residence times should scale.

To determine whether either limit is appropriate for describing our experiment, we model the process of moving from one interstitial site to another as a 1-D random walk on three line segments that share a common origin and are terminated by absorbing boundaries. We numerically implement this model as described in the following section and are able to compute the mean residence times for $p = \{0, 1, 2, 3\}$ in both limits.

8.4 Simulating particle diffusion on an island

The experiments show that to move from one interstitial site to another a particle must break a bond at the initial site and diffuse along the valley between

two of the three underlying particles as depicted by the energy landscape in Fig. 8.2b. This process can be modeled as a 1-D random walk on a segment of length L (Fig. 8.4a). The distribution of residence times in such a model can be determined by considering an ensemble of independent random walkers that enter from the left edge of the segment at the bond breaking rate. The motion of the walkers on the segment is governed by the diffusion rate. The right edge is absorbing, and the rate of absorption of walkers as a function of time yields the distribution of residence times.

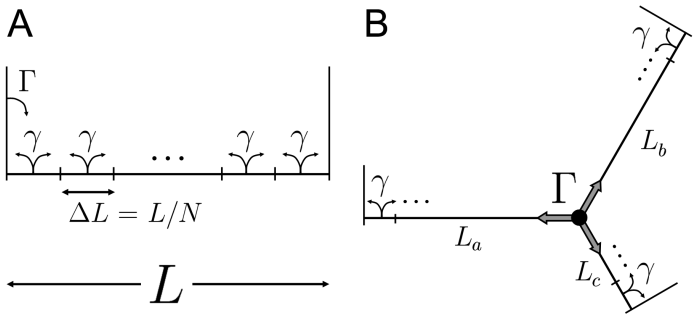

Figure 8.4: (a) Schematic of the 1-D random walk model for a single pathway. (b) Schematic of the model for 3 pathways.

To allow for numerical simulations, we discretize the path into N sites separated by a distance $\Delta L = L/N$. The walkers move between adjacent sites according to the scaled diffusion rate $\gamma = D/\Delta L^2$ and the bond breaking rate Γ. Initially, all walkers are located in the first site at the left edge, and the current $J = \partial n/\partial t$ of walkers into the first two sites is given by

$$\begin{aligned} \frac{\partial n_1}{\partial t} &= -\Gamma n_1 + \gamma n_2 \\ \frac{\partial n_2}{\partial t} &= -2\gamma n_2 + \Gamma n_1 + \gamma n_3, \end{aligned}$$

where we note that the first site loses walkers at the bond breaking rate Γ but

gains walkers that randomly walk back to it at the diffusion rate γ. Since the right boundary is absorbing, the current of walkers into the last two sites is given by

$$\begin{aligned} \frac{\partial n_{N-1}}{\partial t} &= -2\gamma n_{N-1} + \gamma n_{N-2} \\ \frac{\partial n_N}{\partial t} &= \gamma n_{N-1}. \end{aligned}$$

Here the Nth site only gains walkers and does not give any to its neighbor. The current J_i into any the other site is simply

$$\frac{\partial n_i}{\partial t} = -2\gamma n_i + \gamma(n_{i-1} + n_{i+1}).$$

While this description is accurate for a walker on a single pathway, in our experiments a particle departing from one interstitial site has three possible exit pathways $\{a, b, c\}$ that share the same origin (Fig. 8.4B). To model this scenario, the current of random walkers into each site of the three pathways is given by

$$\begin{aligned} \frac{\partial n_1}{\partial t} &= -3\Gamma n_1 + \gamma({n^a}_2 + {n^b}_2 + {n^c}_2) \\ \frac{\partial {n^\alpha}_2}{\partial t} &= -2\gamma {n^\alpha}_2 + \Gamma n_1 + \gamma {n^\alpha}_3,\ \alpha = \{a, b, c\} \\ \frac{\partial {n^\alpha}_i}{\partial t} &= -2\gamma {n^\alpha}_i + \gamma({n^\alpha}_{i-1} + {n^\alpha}_{i+1}),\ \alpha = \{a, b, c\} \\ \frac{\partial {n^\alpha}_{N^\alpha-1}}{\partial t} &= -2\gamma {n^\alpha}_{N^\alpha-1} + \gamma {n^\alpha}_{N^\alpha-2},\ \alpha = \{a, b, c\} \\ \frac{\partial {n^\alpha}_{N^\alpha}}{\partial t} &= \gamma {n^\alpha}_{N^\alpha-1},\ \alpha = \{a, b, c\}. \end{aligned}$$

Here the first site is shared by the three pathways, and the length of each pathway can be varied by tuning $N^\alpha = L^\alpha/\Delta L$. This formulation allows comparison of residence times in interstitial sites with different numbers of descent pathways p by fixing the ratio of descent path lengths to non-descent path lengths to be 2.8. To calculate the distributions of residence times τ, we numerically evaluate these walker currents at each simulation cycle and monitor the total current

$$J_N = \sum_{\alpha=a,b,c} \frac{\partial n^\alpha{}_{N^\alpha}}{\partial t},$$

which is the number of walkers that successfully complete the journey along any pathway as a function of time. By tuning the bond breaking rate Γ relative to the diffusion rate γ, the residence time distributions can be calculated for both limits: when $\Gamma \ll \gamma$, the bond breaking time dominates, and when $\Gamma = \gamma$, the residence time can be described by diffusion alone.

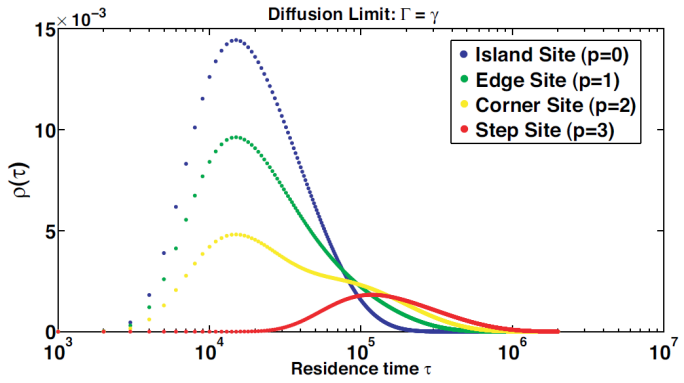

Figure 8.5: The distribution of residence times in the weak-interaction limit is shown for each of 4 kinds of lattice sites.

These distributions $\rho(\tau)$ are shown for the diffusion limit in Fig. 8.5, and for the strong bonding limit in Fig. 8.6. In the latter case, the strong bond limit is approximated by $\Gamma = \gamma/10^5$.

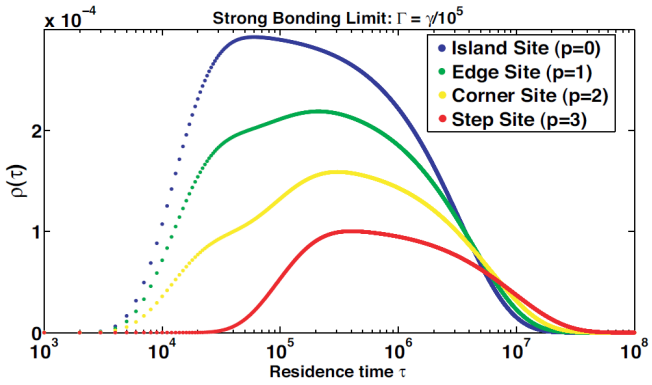

Figure 8.6: The distribution of residence times in the strong-interaction limit is shown for each of 4 kinds of lattice sites.

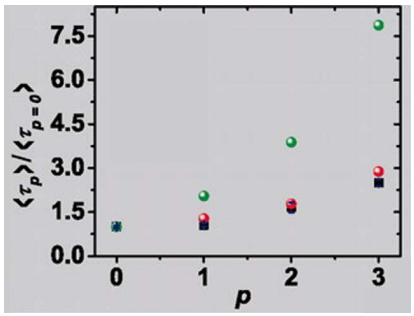

Figure 8.7: The mean residence time τ as a function of p, scaled by the mean residence time when $p = 0$. Experiments are shown as black squares. Error bars are on the order of the symbol size and show SEM. Simulations in the strong interaction limit (red circles) and weak interaction limit (green circles) are also shown.

To explore the scaling of the mean residence time $\langle\tau\rangle$ with the length of the descent pathway, we plot the mean residence time scaled by the mean residence time for an internal interstitial site where $p = 0$ (Fig. 8.7). The scaled residence times are consistent with the intuition that in the weak-interaction limit, $\langle\tau_{p=3}\rangle \,/\, \langle\tau_{p=0}\rangle \approx 2.8^2$, while in the strong-interaction limit $\langle\tau_{p=3}\rangle \,/\, \langle\tau_{p=0}\rangle \approx 2.8$.

8.5 Conclusions

These numerical simulations allow us to finally understand the ESB-like barrier observed for our colloidal systems. Clearly the experimental data in Fig. 8.7 are consistent with the numerical results in the strong-interaction limit, indicating that the observed barrier can indeed be explained by considering the differences in diffusion time caused by differing pathway lengths, even in the absence of any increased energetic barrier. This diffusion-based cause for the ESB, which in atomic systems is typically discarded as a tiny correction, must be properly appreciated in order to design crystal growth scenarios that optimize layer-by-layer, mound-free epitaxial growth.

APPENDIX A

COLLOIDAL DIMER SYNTHESIS

The colloidal dimer particles are templated from sacrificial α-Fe_2O_3 (hematite) core particles prepared via aging of a condensed $Fe(OH)_3$ gel as described in [63]. In a typical synthesis, 50 mL of $FeCl_3$ (2.0 M) is mixed with 45 mL of NaOH (6.0 M) and 5 mL of the shape-modifier, Na_2SO_4 (0.6 M), before being placed in an oven set at 100°C for 8 days. To make the nonmagnetic particles investigated in this study, a layer of rhodamine isothiocyanate-modified silica is then coated on the α-Fe_2O_3 cores using a base catalyzed sol-gel reaction under sonication at 30°C for 4 hours. A reaction mixture comprised of 0.4% hematite powder, 0.25% rhodamine dye solution, 7.1 M deionized water, 0.92 M ammonia, and 17.4 mM tetraorthoethylsilicate added batch-wise to isopropyl alcohol medium produces fluorescent silica shells approximately 65 nm thick. The shells are stabilized with a non-ionic surfactant, polyvinylpyrrolidone (30000 molecular weight), and finally the hematite cores are selectively etched by dissolution in 18% hydrochloric acid solution at room temperature. Before use, the colloidal suspension is titrated to pH 7, washed via repeated centrifugation and decanting, and redispersed in deionized water. This synthesis protocol routinely produces 95% pure dimer particles.

APPENDIX B

RAMP CELL CONSTRUCTION

The wedge-shaped confinement cells are constructed using a $2" \times 3"$ microscope slide with two #1.5 (170 μm thick) 20 mm $\times$ 55 mm coverslips. One coverslip is bonded to the microscope slide using UV glue (Norland Adhesive) to provide a structural base for the confinement cell (Fig. B.1a). Both coverslips must be thoroughly washed using a base wash solution to remove the coating that is applied during manufacturing to prevent the coverslips from sticking together. We prepare the base wash using the following recipe:

- 10 g of Sodium Hydroxide tablets
- 40 mL Deionized (DI) H_2O
- 60 mL Ethanol (optional)

The above are combined, producing a highly basic (pH $\approx$ 14) solution that will remove the anti-stick coating and any other dirt from the surfaces of the coverslips after about a 30 minute soak. The coverslips are then individually rinsed with DI H_2O and then dried using forced filtered air.

After this washing procedure, the glass coverslips are clean enough that when pressed together, two coverslips will bond together similarly to how clean fused silica wafers bond as described in [62]. In order achieve the wedge-shaped geometry, before the two coverslips are bonded together, small spacers are added to the coverslip on the slide by curing 2 rows of tiny droplets of UV glue as depicted in Fig. B.1b. After the spacers are cured, the second coverslip is place on top of the first and the two are squeezed together until a bond forms

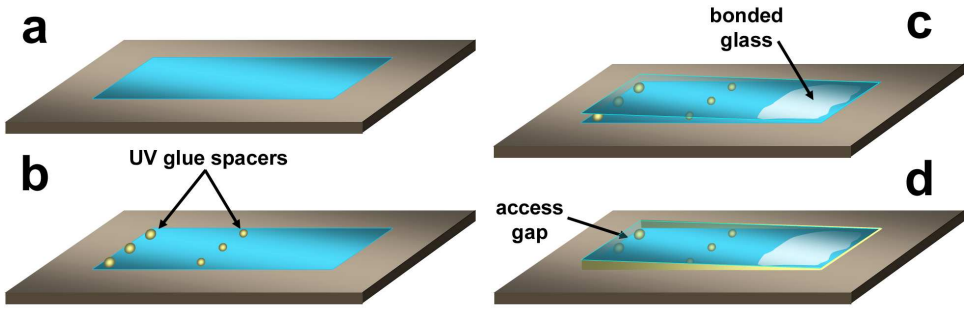

Figure B.1: Schematic of wedge-shaped confinement cell construction. The wedge angle is exaggerated for clarity. (a) One base-washed coverslip (blue) is bonded with UV glue to a larger microscope slide (beige) to provide structural support for the cell. (b) Small UV glue droplets (yellow) are placed in two rows on the coverslip and are cured to become spacers for the cell. (c) A second base-washed coverslip is placed on top of the first, and the two are squeezed together until the two coverslips bond together (bonded region shown in white). (d) UV glue (shown in yellow) is then used to seal three sides of the cell, leaving an access gap for inserting colloidal samples. Once the cell is filled with sample, this gap is also sealed using UV glue.

at the end without spacers (Fig. B.1c). UV glue is then used to seal three sides of the cell, leaving an access gap in the spacer end (Fig. B.1c).

At this point, the cell is clean, sealed, and ready to be filled with a colloidal sample, which may be pipetted in through the access gap. Finally UV glue is used to seal the access gap. The region of the cell that only accommodates one layer of ~ 1 μm-sized particles is typically found several mm above the edge of the bonded region. The slope of the wedge in the monolayer region is about 1 μm over 1 mm. Samples prepared in such wedge-shaped confinement cells can be stored for very long time periods – we have used such samples 2 years after the preparation date without noticing any evaporation or sample degradation.

APPENDIX C

THE DEPLETION EFFECT

In a suspension containing particles of two different radii, the attractive depletion interaction arises as a result of the configurational entropy of the smaller spheres [3]. Due to their hard cores, the smaller spheres cannot access the volume immediately surrounding the larger particles. This excluded volume is schematically shown by the green region in Fig. C.1.

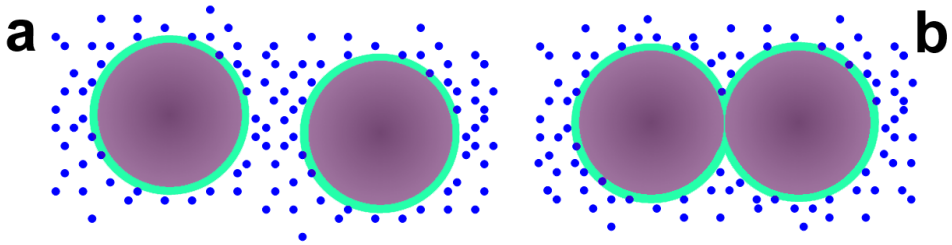

Figure C.1: Illustration of the depletion effect. The purple and blue spheres represent large and small colloidal particles, respectively. The shaded green regions surrounding the purple particles represents the excluded volume that the small spheres cannot access. (a) When two large particles are sufficiently separated, these excluded regions do not overlap. (b) If the purple particles move close enough that the blue particles cannot fit in the region between then, the total excluded volume for the spheres is decreased and an effect attractive interaction is produced.

If the Brownian motion of two larger spheres happens to bring them close enough together that the excluded volumes around each sphere overlap, then the total excluded volume for the small spheres is reduced. This means that the total configurational phase space that is accessible to the small spheres is increased when the larger spheres move closer together, so that this is the entropically favored state.

Equivalently, the depletion effect can also be intuitively understood by thinking about the unbalanced osmotic pressure exerted on the larger spheres by the smaller spheres when the larger spheres are close together. Since the smaller spheres are excluded from the volume between the larger spheres, there is a concentration gradient between this overlap region and the bulk, leading to the unbalanced osmotic pressure that 'pushes' the larger spheres together.

The range of the depletion interaction is set by the diameter of the small spheres and the strength of the depletion attraction depends on their concentration. In practice, often the small spheres are actually so-called 'depletant' polymers suspended in a bad solvent so that they prefer to form a tightly balled shape with a small radius of gyration.

APPENDIX D

SUBSTRATE FABRICATION

The procedures for patterning arrays of particle-sized holes into transparent substrates for epitaxial crystal growth studies and other projects (including crystallization on curved surfaces and in the presence of screw dislocations) were developed by me over the course of several years. The development of the processes was greatly aided by the staff at the Cornell Nanoscale Science and Technology Facility (CNF), especially Rob Ilic, John Treichler, Meredith Metzler, Alan Bleier, Garry Bordonaro and Daron Westly.

D.1 Patterning holes into a PMMA layer

This procedure utilizes electron beam (e-beam) lithography to write a pattern into a thin layer of polymethylmethacrylate (PMMA) that is spin-coated onto a #1.5 (170 μm thick) $1''$ round standard borosilicate coverslip.

1. Clean a #1.5 (170 μm thick) $1''$ round coverslip. (This step is schematically depicted in Fig. D.1a.)
   (a) Base-wash the coverslip using the base wash recipe described in Appendix B.
   (b) Plasma-clean the coverslip using O_2 for ≥ 5 min using the Glen 1000 Resist Strip tool at CNF.
2. Spin-coat and bake a 500 nm layer of PMMA (495 K 8% in Anisole) on top of the coverslip. (Fig. D.1b)

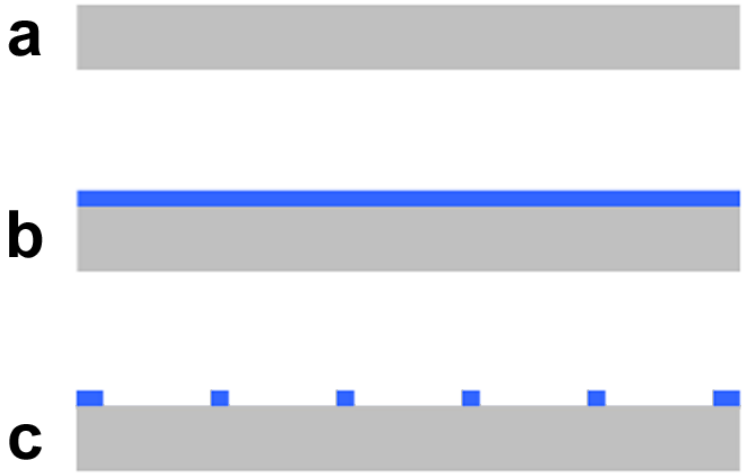

Figure D.1: Illustration of the process for patterning holes into a PMMA layer on top of a borosilicate coverslip. Process details corresponding to each lettered frame are provided in the text. Color code is as follows: gray-coverslip; blue-PMMA.

3. Write the desired pattern into the PMMA using e-beam lithography (typically the VB6 Electron-Beam Lithography tool at CNF, which has now been replaced by a new JEOL e-beam tool). (Fig. D.1c)

4. Develop the exposed PMMA pattern, producing a PMMA layer with holes in it. (Fig. D.1d)

This process yields high-quality PMMA substrates that can be used with both aqueous and oil-based suspensions of colloidal particles. Unfortunately, these substrates cannot withstand surfactants or any form of abrasion. As a result, these substrates are typically only used once and then discarded.

D.2 Patterning holes directly into glass

While the patterned PMMA substrates are useful for a variety of applications, a different substrate material is necessary in cases where charging is important or where it is desirable to vigorously clean and reuse the substrate. Ideally one would like to directly pattern holes into the #1.5 coverslips that are used on the confocal microscope. However, these coverslips are made of borosilicate glass that is index-tuned for confocal microscopy and unfortunately cannot easily be etched using standard reactive ion etching techniques. Thus it is necessary to develop an alternative process. In this section I provide a brief overview of the procedure I developed to pattern a pure silica layer of glass fused on top of a borosilicate coverslip. The process is schematically depicted in Fig. D.2.

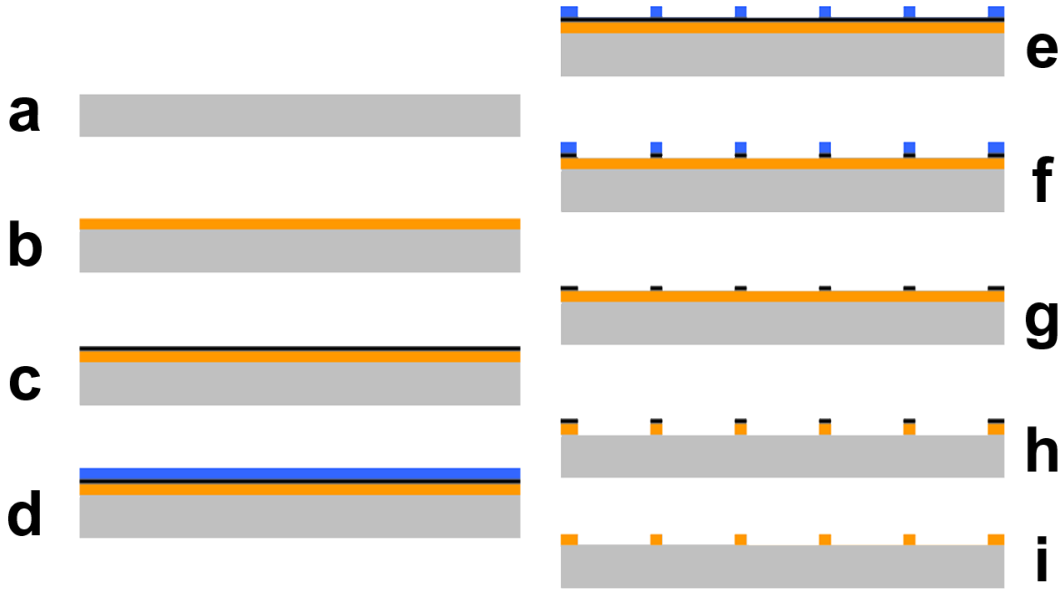

Figure D.2: Illustration of the process for patterning holes into a glass layer on top of a borosilicate coverslip. Process details corresponding to each lettered frame are provided in the text. Color code is as follows: gray-coverslip; orange-silica; black-Chromium; blue-PMMA.

1. Clean a #1.5 (170 μm thick) $1^{"}$ round coverslip. (This step is schematically depicted in Fig. D.2a.)

   (a) Base-wash the coverslip using the base wash recipe described in Appendix B.

   (b) Plasma-clean the coverslip using O_2 for ≥ 5 min using the Glen 1000 Resist Strip tool at CNF.

2. Grow a $\sim$500 nm thick silica (SiO_2) layer using the IPE 1000 Plasma-Enhanced Chemical Vapor Deposition System tool at CNF. (Fig. D.2b)

3. Sputter a 60 nm thick layer of Chromium (Cr) on top of the SiO_2 layer using the CVC Sputter Deposition tool at CNF. (Fig. D.2c)

4. Spin-coat and bake a layer of PMMA (495 K 8% in Anisole) on top of the Cr layer. (Fig. D.2d)

5. Write the desired pattern into the PMMA using e-beam lithography (typically the VB6 Electron-Beam Lithography tool at CNF, which has now been replaced by a new JEOL e-beam tool). (Fig. D.2e)

6. Develop the exposed PMMA pattern, producing a PMMA layer with holes in it. (Fig. D.2f)

7. Etch the exposed Cr layer with Fluorine chemistry using the Trion Minilock III Reactive Ion Etcher tool at CNF. This step exposes the silica layer at the bottom of the holes. (Fig. D.2f)

8. Remove PMMA by soaking in methylene chloride for $\geq$5 min. (Fig. D.2g)

9. Etch the silica layer at the bottom of the holes using CHF_3 plus Ar chemistry in the Oxford PlasmaLab 80+ Reactive Ion Etcher tool at CNF. (Fig. D.2h)

10. Remove any remaining Cr and any dirt using O_2 plasma in the Oxford PlasmaLab 80+ Reactive Ion Etcher tool at CNF. (Fig. D.2i)

The above procedure yields high-quality, reproducible substrates that are quite robust to abrasion and surfactants. These substrates can also be thoroughly washed using the base wash recipe described in Appendix B, allowing them to be used repeatedly for multiple experiments.

BIBLIOGRAPHY

[1] G. Adam and J.H. Gibbs. On the temperature dependence of cooperative relaxation properties in glass-forming liquids. *J. Chem. Phys.*, 43(1):139–146, 1965.

[2] A.M. Alsayed, M.F. Islam, J. Zhang, P.J. Collings, and A.G. Yodh. Premelting at defects within bulk colloidal crystals. *Science*, 309(5738):1207–1210, 2005.

[3] S. Asakura and F. Oosawa. On interaction between two bodies immersed in a solution of macromolecules. *J. Chem. Phys.*, 22(7):1255–1256, 1954.

[4] S. Badaire, C. Cottin-Bizonne, J.W. Woody, A. Yang, and A.D. Stroock. Shape selectivity in the assembly of lithographically designed colloidal particles. *J. Am. Chem. Soc.*, 129(1):40 – 41, 2007.

[5] C. Braga and K.P. Travis. A configurational temperature Nosé-Hoover thermostat. *J. Chem. Phys.*, 123:134101, 2005.

[6] J. Brujić, P. Wang, C. Song, D.L. Johnson, O. Sindt, and H.A. Makse. Granular dynamics in compaction and stress relaxation. *Phys. Rev. Lett.*, 95(12):128001, 2005.

[7] Z.D. Cheng, W.B. Russell, and P.M. Chaikin. Controlled growth of hard-sphere colloidal crystals. *Nature*, 401(6756):893–895, 1999.

[8] Y.-S. Cho, G.-R. Yi, S.-H. Kim, S.-J. Jeon, M.T. Elsesser, H.K. Yu, S.-M. Yang, and D.J. Pine. Particles with coordinated patches or windows from oil-in-water emulsions. *Chem. Mat.*, 19(13):3183–3193, 2007.

[9] A. Coniglio, A. Fierro, H.J. Herrmann, and M. Nicodemi, editors. *Unifying Concepts in Granular Media and Glasses*. Elsevier, 2004.

[10] A.H. Cottrell and B.A. Bilby. Dislocation theory of yielding and strain ageing of Iron. *Proc. Phys. Soc. London A*, 62(349):49 – 62, 1949.

[11] JC Crocker and DG Grier. Methods of digital video microscopy for colloidal studies. *J. Colloid and Interface Sci.*, 179(1):298–310, 1996.

[12] FF Csikor, C Motz, D Weygand, M Zaiser, and S Zapperi. Dislocation avalanches, strain bursts, and the problem of plastic forming at the micrometer scale. *Science*, 318(5848):251–254, 2007.

[13] V.W.A. de Villeneuve, R.P.A. Dullens, D.G.A.L. Aarts, E. Groeneveld, J.H. Scherff, W.K. Kegel, and H.N.W. Lekkerkerker. Colloidal hard-sphere crystal growth frustrated by large spherical impurities. *Science*, 309(5738):1231–1233, 2005.

[14] E.R. Dufresne and D.G. Grier. Optical tweezer arrays and optical substrates created with diffractive optical elements. *Rev. Sci. Instr.*, 69:1974 – 1977, 1998.

[15] M.D. Ediger, C.A. Angell, and S.R. Nagel. Supercooled liquids and glasses. *J. Phys. Chem.*, 100(31):13200 – 12, 1996.

[16] G. Ehrlich and F.G. Hudda. Atomic view of surface self-diffusion: Tungsten on Tungsten. *J. Chem. Phys.*, 44:1039, 1966.

[17] C. Eisenmann, U. Gasser, P. Keim, and G. Maret. Anisotropic defect-mediated melting of two-dimensional colloidal crystals. *Phys. Rev. Lett.*, 93(10):105702, 2004.

[18] C. Eisenmann, U. Gasser, P. Keim, G. Maret, and H.H. von Grunberg. Pair interaction of dislocations in two-dimensional crystals. *Phys. Rev. Lett.*, 95(18):185502, 2005.

[19] D.J. Evans and G.P. Morriss. *Statistical Mechanics of Nonequilibrium Liquids*. Academic Press, 1990.

[20] R. Ganapathy, M.R. Buckley, S.J. Gerbode, and I. Cohen. Direct measurements of island growth and step-edge barriers in colloidal epitaxy. *Science*, 327(5964):445–448, Jan 22 2010.

[21] S.J. Gerbode, U. Agarwal, D.C. Ong, C.M. Liddell, F.A. Escobedo, and I. Cohen. Glassy Dislocation Dynamics in 2-D Colloidal Dimer Crystals. *Phys. Rev. Lett.*, in review, 2010.

[22] S.J. Gerbode, S.H. Lee, C.M. Liddell, and I. Cohen. Restricted dislocation motion in crystals of colloidal dimer particles. *Phys. Rev. Lett.*, 101(5):058302, Aug 1 2008.

[23] S.C. Glotzer and M.J. Solomon. Anisotropy of building blocks and their assembly into complex structures. *Nat. Mater.*, 6(8):557–562, 2007.

[24] W. Gotze and L. Sjogren. Logarithmic decay laws in glassy systems. *J. Phys.: Condens. Matter*, 1(26):4203 – 4222, 1989.

[25] C.J. Hernandez and T.G. Mason. Colloidal alphabet soup: monodisperse dispersions of shape-designed lithoparticles. *J. Phys. Chem. C*, 111(12):4477–4480, 2007.

[26] A. Holz, D.T. Vigren, and M. Zuckermann. Dislocation theory of dimer melting in two dimensions: lipid membranes. *Phys. Rev. B*, 31(1):420 – 429, 1985.

[27] P.M. Johnson, C.M. van Kats, and A. van Blaaderen. Synthesis of colloidal silica dumbbells. *Langmuir*, 21(24):11510 – 11517, 2005.

[28] J. Kakalios, R.A. Street, and W.B. Jackson. Stretched-exponential relaxation arising from dispersive diffusion of hydrogen in amorphous-silicon. *Phys. Rev. Lett.*, 59(9):1037–1040, 1987.

[29] W.K. Kegel and A. van Blaaderen. Direct observation of dynamical heterogeneities in colloidal hard-sphere suspensions. *Science*, 287(5451):290–293, 2000.

[30] J. Kim, R.J. Larsen, and D.A. Weitz. Uniform nonspherical colloidal particles with tunable shapes. *Adv. Mater.*, 19(15):2005 – 2009, 2007.

[31] J.B. Knight, C.G. Fandrich, C.N. Lau, H.M. Jaeger, and S.R. Nagel. Density relaxation in a vibrated granular material. *Phys. Rev. E*, 51(5):3957–3963, 1995.

[32] J.M. Kosterlitz and D.J. Thouless. Ordering, metastability and phase transitions in two-dimensional systems. *J. Phys. C*, 6:1181 – 1203, 1973.

[33] W. Krauth and R. Moessner. Pocket Monte Carlo algorithm for classical doped dimer models. *Phys. Rev. B*, 67:064503, 2003.

[34] S.H. Lee, S.J. Gerbode, B.S. John, A.K. Wolfgang, F.A. Escobedo, I. Cohen, and C.M. Liddell. Synthesis and assembly of nonspherical hollow silica colloids under confinement. *J. Mater. Chem.*, 18(41):4912–4916, 2008.

[35] A.W. Lees and S.F. Edwards. The computer study of transport processes under extreme conditions. *J. Phys. C*, 5:1921, 1972.

[36] A. Libál, C. Reichhardt, and C.J. Olson Reichhardt. Point-defect dynamics in two-dimensional colloidal crystals. *Phys. Rev. E*, 75(1):011403, Jan 2007.

[37] C.M. Liddell and C.J. Summers. Monodispersed ZnS dimers, trimers, and tetramers for lower symmetry photonic crystal lattices. *Adv. Mater.*, 15(20):1715 – 1719, 2003.

[38] A.J. Liu and S.R. Nagel. Nonlinear dynamics: Jamming is not just cool any more. *Nature*, 396(6706):21 – 22, 1998.

[39] V.N. Manoharan, M.T. Elsesser, and D.J. Pine. Dense packing and symmetry in small clusters of microspheres. *Science*, 301(5632):483 – 487, 2003.

[40] Y.-W. Mo, B.S. Swartzentruber, R. Kariotis, M.B. Webb, and M.G. Lagally. Growth and equilibrium structures in the epitaxy of Si on Si(001). *Phys. Rev. Lett.*, 63(21):2393–2396, Nov 1989.

[41] R. Moessner and S.L. Sondhi. Resonating valence bond phase in the triangular lattice quantum dimer model. *Phys. Rev. Lett.*, 86(9):1881 – 1884, 2001.

[42] CB Murray, CR Kagan, and MG Bawendi. Synthesis and characterization of monodisperse nanocrystals and close-packed nanocrystal assemblies. *Ann. Rev. of Mat. Sci.*, 30:545–610, 2000.

[43] D.R. Nelson and B.I. Halperin. Dislocation-mediated melting in 2 dimensions. *Phys. Rev. B*, 19(5):2457 – 2484, 1979.

[44] C.R. Nugent, K.V. Edmond, H.N. Patel, and E.R. Weeks. Colloidal glass transition observed in confinement. *Phys. Rev. Lett.*, 99(2), 2007.

[45] C.J. Olson, C. Reichhardt, M. McCloskey, and R.J. Zieve. Effect of grain anisotropy on ordering, stability and dynamics in granular systems. *Europhys. Lett.*, 57(6):904 – 910, 2002.

[46] E. Orowan. Plasticity of crystals. *Z. Phys.*, 89(9-10):605 – 659, 1934.

[47] M. Oxborrow and C.L. Henley. Random square-triangle tilings - a model

for twelvefold-symmetrical quasi-crystals. *Phys. Rev. B*, 48(10):6966–6998, 1993.

[48] A. Pertsinidis and X. S. Ling. Equilibrium configurations and energetics of point defects in two-dimensional colloidal crystals. *Phys. Rev. Lett.*, 87(9):098303, 2001.

[49] K.N. Pham, A.M. Puertas, J. Bergenholtz, S.U. Egelhaaf, A. Moussaid, P.N. Pusey, A.B. Schofield, M.E. Cates, M. Fuchs, and W.C.K. Poon. Multiple glassy states in a simple model system. *Science*, 296(5565):104–106, 2002.

[50] M. Polanyi. Lattice distortion which originates plastic flow. *Z. Phys.*, 89(9-10):660 – 662, 1934.

[51] P.N. Pusey and W. van Megen. Phase-behavior of concentrated suspensions of nearly hard colloidal spheres. *Nature*, 320(6060):340–342, 1986.

[52] X.R. Qin and M.G. Lagally. Adatom pairing structures for Ge on Si(100): The initial stage of island formation. *Science*, 278(5342):1444 – 1447, 1997.

[53] I.C. Rankenburg and R.J. Zieve. Influence of shape on ordering of granular systems in two dimensions. *Phys. Rev. E*, 63(6):061303, 2001.

[54] S. Redner. *A Guide to First Passage Processes*. Cambridge Univ. Press, 2001.

[55] J.R. Savage, D.W. Blair, A.J. Levine, R.A. Guyer, and A.D. Dinsmore. Imaging the sublimation dynamics of colloidal crystallites. *Science*, 314(5800):795–798, 2006.

[56] P. Schall, I. Cohen, D.A. Weitz, and F. Spaepen. Visualization of dislocation dynamics in colloidal crystals. *Science*, 305(5692):1944 – 1948, 2004.

[57] P. Schall, I. Cohen, D.A. Weitz, and F. Spaepen. Visualizing dislocation nucleation by indenting colloidal crystals. *Nature*, 440:319 – 323, 2006.

[58] M Schmidt and H Lowen. Phase diagram of hard spheres confined between two parallel plates. *Phys. Rev. E*, 55(6, Part B):7228–7241, 1997.

[59] R.L. Schwoebel and Shipsey E.J. Step motion on crystal surfaces. *J. Appl. Phys.*, 37:3682, 1966.

[60] S.I. Simdyankin and N. Mousseau. Relationship between dynamical heterogeneities and stretched exponential relaxation. *Phys. Rev. E*, 68(4):41110 – 17, 2003.

[61] G. Springholz, V. Holy, M. Pinczolits, and Bauer G. Self-organized growth of three-dimensional quantum-dot crystals with fcc-like stacking and a tunable lattice constant. *Science*, 282(5389):734 – 737, 1998.

[62] E.A. Strychalski, S.M. Stavis, and H.G. Craighead. Non-planar nanofluidic devices for single molecule analysis fabricated using nanoglassblowing. *Nanotech.*, 19(31), 2008.

[63] T. Sugimoto, M.H. Khan, and A. Muramatsu. Preparation of monodisperse peanut-type alpha-Fe2O3 particles from condensed ferric hydroxide gel. *Colloids and Surf. A*, 70:167–169, 1993.

[64] G.I. Taylor. Plastic deformation of crystals. *Proc. R. Soc. A*, 145:362 – 404, 1934.

[65] A. van Blaaderen and A. Vrij. Synthesis and characterization of colloidal dispersions of fluorescent, monodisperse silica spheres. *Langmuir*, 8:2921–2931, 1992.

[66] Y.A. Vlasov, X.Z. Bo, J.C. Sturm, and D.J. Norris. On-chip natural assembly of silicon photonic bandgap crystals. *Nature*, 414(6861):289–293, 2001.

[67] E.R. Weeks, J.C. Crocker, A.C. Levitt, A. Schofield, and D.A. Weitz. Three-dimensional direct imaging of structural relaxation near the colloidal glass transition. *Science*, 287(5453):627–631, 2000.

[68] Eric R. Weeks and D.A. Weitz. Properties of cage rearrangements observed near the colloidal glass transition. *Phys. Rev. Lett.*, 89(9):095704, Aug 2002.

[69] J.D. Weeks, D. Chandler, and H.C. Andersen. Role of repulsive forces in determining the equilibrium structure of simple liquids. *J. Chem. Phys.*, 54:5237, 1971.

[70] J. Weertman and J.R. Weertman. *Elementary Dislocation Theory*. Oxford University Press, 1992.

[71] K.W. Wojciechowski. Monte carlo simulations of highly anisotropic two-

dimensional hard dumbbell-shaped molecules: nonperiodic phase between fluid and dense solid. *Phys. Rev. Lett.*, 46(1):26–39, 1992.

[72] K.W. Wojciechowski. Monte carlo simulations of highly anisotropic two-dimensional hard dumbbell-shaped molecules: nonperiodic phase between fluid and dense solid. *Phys. Rev. B*, 46(1):26 – 39, 1992.

[73] K.W. Wojciechowski, D. Frenkel, and A.C. Branka. Nonperiodic solid phase in a two-dimensional hard-dimer system. *Phys. Rev. Lett.*, 66(24):3168 – 71, 1991.

[74] A Yethiraj and A van Blaaderen. A colloidal model system with an interaction tunable from hard sphere to soft and dipolar. *Nature*, 421(6922):513–517, 2003.

[75] A.P. Young. Melting and the vector coulomb gas in 2 dimensions. *Phys. Rev. B*, 19(4):1855–1866, 1979.

[76] K. Zahn, R. Lenke, and G. Maret. Two-stage melting of paramagnetic colloidal crystals in two dimensions. *Phys. Rev. Lett.*, 82(13):2721 – 2724, 1999.

[77] Z. Zhang and M.G. Lagally. Atomistic processes in the early stages of thin-film growth. *Science*, 276(5311):377–383, 1997.